

Optical and Structural Properties of Europium Doped Silicon Oxide Thin Films

by

Rashin Basiri Namin

Bachelor of Engineering, Chemical Engineering Department, 2013

A Thesis, Submitted in Partial Fulfillment
of the Requirements for the Degree of

Master of Science

In the Graduate Academic Unit of Chemical Engineering

Supervisors: Zahra Khatami, Ph.D., Electrical & Computer Engineering
Felipe Chibante, Ph.D., Chemical Engineering

Examining Board: Guida Bendrich, Ph.D., Chemical Engineering
Brian Lowry, Ph.D., Chemical Engineering
Brent Peterson, Ph.D., Electrical & Computer Engineering

This thesis is accepted by the
Dean of Graduate Studies

THE UNIVERSITY OF NEW BRUNSWICK

August 2021

©Rashin Basiri Namin, 2021

Abstract

Rare earth doping is one of the main approaches to enhance the optical properties of silicon-based materials. In this work, a set of europium doped silicon oxide ($\text{Eu}_x\text{Si}_y\text{O}_z$) thin films are fabricated using an integrated magnetron sputtering electron cyclotron resonance plasma enhanced chemical vapor deposition (IMS-ECR-PECVD) system. The thin film composition was studied by Rutherford backscattering spectrometry (RBS) and elastic recoil detection (ERD) measurements verifying high control over the Eu content by changing the sputtering power. Variable Angle spectroscopic ellipsometry (VASE) was conducted, delivering the refractive index and thickness. Using a UV laser (325 nm) excitation source, Photoluminescence (PL) measurements were performed, and it was confirmed that Eu^{3+} transition which is associated with the red light emission is successfully achieved even at annealing temperatures as low as 300°C. Performing X-ray diffraction (XRD) analysis, the structural properties of the thin films were studied and the formation of $\text{Eu}_x\text{Si}_y\text{O}_z$ crystals was confirmed for the samples annealed at elevated temperatures.

Dedication

This thesis is dedicated to my mother, Nahid Eghbali, and the memory of my beloved father, Davoud Basiri Namin, who had always supported my enthusiasm for science. I promised myself to make them proud, and I hope I am on the way to reach there with this achievement as well as the ones to be achieved in the future.

Acknowledgements

I have started my MScE research at UNB in the pandemic and this work would not have been possible without the help and support of many individuals. Their assistance and guide made me enjoy the time spent working on this study and learn a great deal.

First, I would like to thank my dear supervisors Dr. Zahra Khatami and Dr. Felipe Chibante whose regardless help allowed me to build up my carrier as a researcher. They provided me with advice in all the steps from the early stages of this work. Despite being great supervisors, they have been wonderful friends during the last year. Dr. Zahra has patiently assigned me to the tasks that thought me I should be tolerant as a researcher and take one step at a time. In addition to being a charismatic supervisor, she has been a wonderful friend to me. I could not be happier working as a member of her team. Dr. Chibante also dedicated time and energy to listen to the challenges that I faced during my research and provided me with insightful guidance which made me think from different points of view and improve my skills. Although COVID made life difficult for everyone, these people became the reason I could have an amazing time working and learning.

I would also like to thank my committee members, Dr. Guida Bendrich, Dr. Brian Lowry and Dr. Brent Peterson, for putting the time and afford to give me feedback.

My special thank is to Dr. Peter Mascher for welcoming me to their virtual group meetings at the Department of Engineering Physics at McMaster University. The virtual group meetings kept me motivated to work harder and make progress during this isolation period. Dr. Mascher has always informed us about the online training going on in the community. He, along with my supervisors encouraged me to attend as many conferences and webinars

as possible, either as an audience or a presenter. Also, his collaboration on the projects was extremely helpful and informative to get to know the research going on in our field. Also, I got the chance to get to know the wonderful people who are Dr. Mascher's students and collaborate with Dr. Zahra's team. They all were open for discussion and helping each other including me.

Among the McMaster students, I am especially thankful to Yuxuan Gao (Michael) for training me on SIMNRA software; Aysegul Abdelal for further training on SIMNRA software, and Paramita Bhattacharyya and Aysegul for giving us a virtual tour of Dr. Mascher's PECVD facility at Tandem accelerator building in McMaster University, where the samples studied in this research were fabricated. I also thank Dr. Jacek Wojcik, the general manager at Intlvac Inc, for holding individual virtual training on the PECVD system.

I appreciate the time and energy Dr. Lyudmila Goncharova, in Western University, spent helping me to sort out the difficulties I had with RBS and ERD measurements. I also acknowledge Maureen Fitzpatrick for the several virtual training sessions scheduled to assist me with XRD and pole figure analysis. And thanks to, Carmen Andrei in Canadian Centre for Electron Microscopy (CCEM) at McMaster University for her assistance and running the TEM measurements.

Besides all the mentioned people who work in this field of research, I would like to thank the support of my friends and family who always gave me hope to find the strength and keep going. I want to thank my brother, Reza Basiri Namin, who always believed in me and cheered me every single day.

And last but not least, thanks to my dear friend, Reza Alaghmandfard, for generously sharing his knowledge and putting time to help me reach my goals during the very early stages of my career.

Table of Contents

Abstract	ii
Dedication	iii
Acknowledgements	iv
Table of Contents	vii
List of Tables	ix
List of Figures	xi
List of Symbols, Nomenclature or Abbreviations	xvii
Chapter 1: Introduction	1
1.1. Photosynthesis Mechanism	1
1.2. Solar Spectrum	2
1.3. Greenhouse Cover Materials	4
1.4. Conventional and Novel Deposition Systems	6
1.5. Silicon as a Light Emitter	7
1.6. Rare Earth Doped Silicon Nanostructures	10
1.7. Thesis Outline and Contributions	18
Chapter 2: Methodology	20
2.1. Deposition System	20
2.2. Fabricated Thin Films	24
2.3. Post Deposition Annealing	26
Chapter 3: Characterization Techniques	29
3.1. Rutherford Backscattering Spectrometry	29
3.2. Elastic Recoil Detection	33
3.3. Variable Angle Spectroscopic Ellipsometry	33
3.4. Photoluminescence	35
3.5. X-Ray Diffraction	36
3.6. Transmission Electron Microscopy	39

Chapter 4: Optical and Compositional Analyses	40
4.1. Elemental Composition.....	40
4.2. Variable Angle Spectroscopic Ellipsometry	51
4.3. Photoluminescence	54
4.3.1. Influence of Deposition Parameters on Photoluminescence.....	61
 Chapter 5: Structural Analysis	65
5.1. X-ray Diffraction	65
5.2. Transmission Electron Microscopy	79
 Chapter 6: Conclusion and Future Work	85
Future Works	86
 Bibliography	88
Curriculum Vitae	

List of Tables

Table 1. Deposition parameters of a set of nine thin films fabricated using IMS-ECR-PECVD system. The plasma power is 500 W, the O ₂ gas flow rate is 25 sccm, and the deposition time is 60 minutes for all the samples.	25
Table 2. Deposition parameters for a set of six samples fabricated using ECR-PECVD system and in-situ doping using MOP procedure.	25
Table 3. Deposition parameters and elemental composition of the as-deposited thin films. For all samples the deposition time was 60 minutes, microwave plasma power was set to 500 W and O flow rate was 25 sccm while the sputtering power, Ar flow rate and SiH ₄ flow rate varied in the range of 10 to 40 W, 10 to 40 sccm and 1.5 to 2.5 sccm, respectively.	41
Table 4. Deposition parameters and elemental composition of the as-deposited MOP thin films. For all the thin films the microwave plasma power was set to 500 W while the deposition time, SiH ₄ flow rate, and O ₂ flow rate varied in the range of 40 to 60 minutes, 1 to 2.5 sccm, and 25 to 30 sccm, respectively.	47
Table 5. Refractive indices, and thickness of the as-deposited IMS thin films.	52
Table 6. CIE coordination of all the IMS samples annealed at 1350°C and N ₂ +H ₂ atmosphere.	60
Table 7. Elemental composition of 54-Eu _{0.2} Si _{31.9} O _{67.9} , 57-Eu _{1.5} Si _{32.8} O _{65.6} , and 60-Eu _{6.4} Si _{25.7} O _{67.9} which were fabricated using the Ar sputtering gas flow rate of 40 sccm and SiH ₄ gas flow rate of 2 sccm with a variation of sputtering power ranging from 10 to 40 W;	

and the ratio of intensity at 2θ degrees corresponding to $\text{Eu}_x\text{SiO}_2/\text{SiO}_2$ and Eu_2O_3 phases.

.....77

List of Figures

Figure 1. Solar spectrum in space, caused by the sun's blackbody radiation at 5250°C, as well as the terrestrial spectrum and sun radiation at sea level. https://upload.wikimedia.org/wikipedia/commons/4/4c/Solar_Spectrum.png Copyright (2020).....	3
Figure 2. Recombination pathway in direct bandgap materials. The energy of the photon (E_p) is equal to the bandgap energy (E_g) [32].	8
Figure 3. Recombination pathway in indirect bandgap materials with photon interaction [32].	10
Figure 4. Energy levels of trivalent Tb and Ce oxidation states correspond to green and blue light, respectively [34].	12
Figure 5. PL measurements of the as-deposited and annealed CeSiN-pure using N_2+H_2 atmosphere at temperatures ranging from 800 to 1200°C [37].....	13
Figure 6. Energy levels of a) Eu^{2+} [39] and; b) Eu^{3+} ion with the associated wavelength and the energy levels [40]. An excitation source with 394 nm promotes the excitation of electrons in the f level and the potential photon emissions, when the electron drops back to the valence band again.	15
Figure 7. PL measurements of Eu doped Si-rich SiO_x thin film for the as-deposited and annealed samples using N_2 ambient at temperatures ranging from 800 to 1200°C in 100°C increments for 1 hour [41].	16
Figure 8. Gaussian deconvolution of PL spectrum of the Eu doped Si-rich SiO_x film annealed at 1000°C (for 1 hour) using N_2 atmosphere [41].	17

Figure 9. PL measurements of the as-deposited EuO, EuO _{1.2} , and EuO _{1.4} thin films fabricated using pulsed laser deposition [42].	18
Figure 10. Integrated magnetron sputtering and electron cyclotron resonance plasma enhanced chemical vapor deposition (IMS-ECR-PECVD) system. a) The interior area of the deposition chamber; b) a schematic of the exterior area of the ECR-PECVD system including metal organic powder and sputtering gun installed; c) and d) image and schematic of the interior area showing the orientation of the sputtering gun, dispersion ring, sample stage, and the rare earth nozzles [44].	21
Figure 11. A simplified schematic of the PECVD system [28].	22
Figure 12. A 3 inch <100> oriented Si substrate used for the deposition.	23
Figure 13. MOP canisters and the heating jackets inside which the canisters containing MOPs are heated, and the evaporated RE gases are fed into the ECR-PECVD chamber. The temperature is controlled using a K-type thermocouple [28].	23
Figure 14. Quartz tube furnace used for post deposition annealing.	26
Figure 15. A schematic of quartz tube furnace with the annealing gases of Ar, N ₂ , and H ₂ .	26
Figure 16. The formation of Si-ncs in the as-deposited amorphous SiO _x thin film when subjected to post deposition annealing. High annealing temperature results in phase separation within the film and promotes the formation of Si-ncs. Adapted from [32].	28
Figure 17. The schematic of the Rutherford backscattering spectrometry (RBS). Adapted from [46].	30
Figure 18. Representative RBS spectra of an identical sample (57-Eu _{1.5} Si _{32.8} O _{65.6}) deposited on a) C substrate; b) Si substrate.	32

Figure 19. A schematic of VASE setup indicating the linear and elliptically polarized light, plane of the incident, and the sample position. Adapted from [52].	34
Figure 20. A schematic of PL setup. Adapted from [54].	36
Figure 21. A schematic of; a) Angular rotations of sample orientation where X_L , Y_L , and Z_L are the system coordination and ω , ψ and ϕ are the rotational angles; b) Angles and coordination of XRD setup. (s_0) and (s) represent incident and diffracted beam, respectively, where the blue circle in the center is the sample.	38
Figure 22. RBS spectrum of $60\text{-Eu}_{6.4}\text{Si}_{25.7}\text{O}_{67.9}$ where the blue line is the simulated data, and the red dots are the experimental data.	42
Figure 23. Eu at. % of the Eu-ORSO samples as a function of the sputtering power deposited using a constant Ar flow of 40 sccm. Higher sputtering power results in higher concentration of Eu at. %.	43
Figure 24. Effect of SiH_4 flow on Eu at. % with a) sputtering power of 20 W and Ar flow rate of 40 sccm; b) sputtering power of 40 W and Ar flow rate of 40 sccm.	44
Figure 25. The changes of the Eu at. % with regards to sputtering power for different SiH_4 flow rates.	45
Figure 26. ERD spectra of Kapton and samples $53\text{-Eu}_{4.4}\text{Si}_{26.2}\text{O}_{69.4}$, $54\text{-Eu}_{0.2}\text{Si}_{31.9}\text{O}_{67.9}$, $55\text{-Eu}_{0.8}\text{Si}_{31.4}\text{O}_{67.8}$, $59\text{-Eu}_{0.3}\text{Si}_{34.3}\text{O}_{65.4}$, and $60\text{-Eu}_{6.4}\text{Si}_{25.7}\text{O}_{67.9}$. The qualitative change of H is observed for different samples.	49
Figure 27. a) Intensity of ERD spectra; and b) Integrated area of ERD spectra of each sample.	50
Figure 28. The influence of SiH_4 flow rate on the refractive index at different sputtering powers (P) of 10 to 40 W.	53

Figure 29. SiH ₄ influence on the thickness at different sputtering powers (P) of 10, 20 and 40 W. An equal growth rate of thickness as a result of SiH ₄ increase for all sputtering powers is observed.....	54
Figure 30. PL measurements of 57-Eu _{1.5} Si _{32.8} O _{65.6} annealed at temperatures of 300 to 1200°C using N ₂ atmosphere for 60 minutes as the representative of low temperature PL measurements.....	55
Figure 31. PL measurements of 37-Eu _{0.0} Si _{31.53} O _{68.27} and 38-Eu _{0.1} Si _{35.95} O _{58.61} annealed at 1200°C and N ₂ atmosphere for 60 minutes.	57
Figure 32. PL spectra of 52-Eu _{1.0} Si _{35.0} O _{64.0} at 1200°C and 1350°C in N ₂ and N ₂ +H ₂ atmospheres.....	58
Figure 33. PL spectra of all IMS thin films annealed at 1350°C and N ₂ +H ₂ atmosphere. Two main peaks are observed at 430 nm and 460 nm where the highest peak achieved is related to 60-Eu _{6.4} Si _{25.7} O _{67.9}	59
Figure 34. CIE chromaticity diagram of all the IMS samples at annealing condition of 1350°C and N ₂ +H ₂ atmosphere.....	60
Figure 35. PL spectra of 52-Eu _{1.0} Si _{35.0} O _{64.0} , 57-Eu _{1.5} Si _{32.8} O _{65.6} and 58-Eu _{2.1} Si _{34.4} O _{63.5} annealed at 1350°C and N ₂ +H ₂ atmosphere. The sputtering Ar flow rate and sputtering power were set constant at 40 sccm and 20 W for all samples while the SiH ₄ flow rate was 2.5, 2 and 1.5 sccm for 52-Eu _{1.0} Si _{35.0} O _{64.0} , 57-Eu _{1.5} Si _{32.8} O _{65.6} and 58-Eu _{2.1} Si _{34.4} O _{63.5} , respectively.	62
Figure 36. PL spectra of 54-Eu _{0.2} Si _{31.9} O _{67.9} , 57-Eu _{1.5} Si _{32.8} O _{65.6} and 60-Eu _{6.4} Si _{25.7} O _{67.9} at annealing condition of 1350°C and N ₂ +H ₂ atmosphere. The sputtering Ar flow rate and SiH ₄ flow rate were kept constant at 40 sccm and 2 sccm, respectively, for all samples	

while the sputtering power was 10 W for 54-Eu _{0.2} Si _{31.9} O _{67.9} , 20 W for 57-Eu _{1.5} Si _{32.8} O _{65.6} , and 40 W for 60-Eu _{6.4} Si _{25.7} O _{67.9}	63
Figure 37. PL spectra of 56-Eu _{0.2} Si _{34.2} O _{65.6} and 59-Eu _{0.3} Si _{34.3} O _{65.4} at annealing conditions of 1350°C and N ₂ +H ₂ atmosphere. The sputtering power and SiH ₄ flow rate were set at 10 W and 1.5 sccm for both samples while the Ar flow rate was 10 sccm for 56-Eu _{0.2} Si _{34.2} O _{65.6} and 40 sccm for 59-Eu _{0.3} Si _{34.3} O _{65.4}	64
Figure 38. Formation of Si-ncs within the thin films when subjected to post-deposition annealing. The phase separation in the ORSO matrix occurs when the amorphous structure of the thin film changes as the result of thermal annealing.	65
Figure 39. XRD pattern of 60-Eu _{6.4} Si _{25.7} O _{67.9} annealed using N ₂ +H ₂ atmosphere and at a) 800°C temperature exhibits amorphous structure; b) 1000°C shows some crystalline structure; c) Annealed at 1200°C, and d) 1350°C temperature show distinctive Eu _x Si _y O _z crystalline formed.	66
Figure 40. XRD pattern and the phase ID of a) 60-Eu _{6.4} Si _{25.7} O _{67.9} -N ₂ +H ₂ 1000°C; and b) 60-Eu _{6.4} Si _{25.7} O _{67.9} -N ₂ +H ₂ 1200°C.....	67
Figure 41. XRD pattern with phase IDs included for the sample 60-Eu _{6.4} Si _{25.7} O _{67.9} -N ₂ +H ₂ -1350°C.	69
Figure 42. Each image shows a merge of four diffracted frames, at 2θ degrees of 15, 35, 55 and 75, of 60-Eu _{6.4} Si _{25.7} O _{67.9} using an annealing atmosphere of N ₂ +H ₂ . Different annealing temperatures are presented in a) 800°C; b) 1000°C; c) 1200°C; and d) 1350°C.	70
Figure 43. XRD pattern of 60-Eu _{6.4} Si _{25.7} O _{67.9} -N ₂ +H ₂ -1200°C detected at psi (chi) degree of 90 shown in red and 54 shown in black.....	72

Figure 44. XRD frame of 60-Eu _{6.4} Si _{25.7} O _{67.9} -N ₂ +H ₂ -1200°C at psi degree of 54, a full rotation of 360° phi. The blue arrow demonstrates normal to the surface.....	73
Figure 45. Pole figures of 60-Eu _{6.4} Si _{25.7} O _{67.9} annealed at 1200°C with N ₂ +H ₂ atmosphere at 2θ of a) 30°; b) 31.7°; and c) 43.6°	74
Figure 46. XRD pattern of all the IMS samples annealed at 1350°C and N ₂ +H ₂ atmosphere.	76
Figure 47. XRD pattern of 54-Eu _{0.2} Si _{31.9} O _{67.9} , 57-Eu _{1.5} Si _{32.8} O _{65.6} and 60-Eu _{6.4} Si _{25.7} O _{67.9} annealed using N ₂ +H ₂ atmosphere at 1350°C.	78
Figure 48. Bright field HR-TEM image of 60-Eu _{6.4} Si _{25.7} O _{67.9} damaged in FIB preparation.	79
Figure 49. SEM images of the sample indicating the area where FIB preparation was performed.....	81
Figure 50. Cross-sectional dark-field TEM image of the two lamellas prepared using FIB technique on 60-Eu _{6.4} Si _{25.7} O _{67.9} annealed at 1350°C using N ₂ +H ₂ atmosphere.	82
Figure 51. a) TEM imaging of the yellow marked area in Figure 50; b) Magnified view of the area marked in orange in Figure 51 (a).	83
Figure 52. EDX of Figure 51 (b) shows the elemental mapping of the sample where the distribution of Si (blue), O (red), Eu (green), and W (yellow) are presented.....	83
Figure 53. The bright field HR-TEM imaging of a) Zoom up of the marked green zone in Figure 50; b) Magnified view of the blue selected area in Figure 53 (a), where the formation of the Eu _x Si _y O _z nanoclusters (darker spots) in the SiO _x matrix (the brighter spots) is observed.	84

List of Symbols, Nomenclature or Abbreviations

ECR	Electron cyclotron resonance
EDX	Energy dispersive X-ray spectroscopy
ERD	Elastic recoil detection
FIB	Focused ion beam
IMS	Integrated magnetron sputtering
LED	Light emitting diode
MOP	Metal organic powder
MSE	Mean squared error
ORSO	Oxygen rich silicon oxide
PECVD	Plasma enhanced chemical vapor deposition
PL	Photoluminescence
PLE	Photoluminescence excitation
QTF	Quartz tube furnace
RBS	Rutherford backscattering spectroscopy
RE	Rare earth

Si-ncs	Silicon nanoclusters
TEM	Transmission electron microscopy
VASE	Variable angle spectroscopic ellipsometry
XRD	X-ray diffraction

Chapter 1: Introduction

As the second most abundant element on earth, silicon (Si) is a prominent material in numerous commercial microelectronics applications owing to its outstanding features such as high stability, purity, ease of engineering, high carrier mobility, and prevalent fabrication methods [1]. Despite its prevalent use in electronics, Si is not a promising material for the photonics industry or light applications due to its indirect bandgap. However, through structural modifications of Si-based materials, it can gain luminescence properties and consequently benefit many industries as well as light-emitting diodes (LEDs), displays, etc. [2]. One of the most recent applications of Si as a light emitter is in greenhouse applications where the solar spectrum is absorbed, and light is selectively emitted in the wavelength ranges that are beneficial for plant photosynthesis [3].

This chapter begins by discussing the mechanism of plant photosynthesis and the global range of the solar spectrum, then the conventional materials used as greenhouse covers are introduced as well as the challenges associated with them, followed by the advantages of thin films, and their well-established fabrication techniques. The process of light emission and the problem with bulk Si as a light emitter are explained. Finally, the role of rare earth (RE) elements in enhancing the optical properties of materials is discussed via comprehensive state-of-the-art developments.

1.1. Photosynthesis Mechanism

Photosynthesis is a process that takes place in plants to convert light energy to chemical energy which can be utilized by the plants to grow [4]. The process of photosynthesis occurs in the presence of water (H_2O) which is transported from soil to the leaves, carbon

dioxide (CO_2) absorbed from the air by some cells in the leaves called stomata, and the photon (light particle) energy which is normally provided by the sunlight. Stomata are responsible for receiving CO_2 from the air and releasing O_2 [5]. Leaf cells contain components called chloroplast which are responsible for converting CO_2 and H_2O to glucose and O_2 in the presence of sunlight energy [5]. Water molecules act as an electron donor where the photon provides energy to excite an electron with the by-products being O_2 and H^+ [6]. The O_2 is released into the air through stomata and H^+ goes through the second set of photosynthesis reactions to react with CO_2 and produces glucose and other forms of energy that are consumable by the plants [6].

Photosynthesis is generally divided into two main categories of light reaction (light dependent) and dark reaction (light-independent). The dark reaction is also known as Calvin Cycle [5]. In the light reaction, the photon from sunlight hits the chloroplast which is made of pigments called chlorophyll. The chlorophyll is the light-absorbing pigment. The structures inside the chloroplast, called grana, are responsible for water splitting reactions. When the photon from sunlight encounters the chlorophyll, it provides the energy required for water molecules to split into O_2 which is released into the air by stroma, H^+ , some electron carrier molecules called NADPH, and some energy in the form of ATP [7].

The second reaction (dark reaction) is where the glucose is formed by using the energy provided by ATP and NADPH. The biochemistry of the second part of the photosynthesis reaction is not relevant to this thesis.

1.2. Solar Spectrum

Solar radiation is required for the photosynthesis process to proceed [8]. The sun spectrum with the contribution of each light range is shown in Figure 1. The solar radiation is originated from the blackbody radiation at a temperature of 5250°C. The solar spectrum in space differs from the radiation that reaches the earth due to the absorption by the earth's outer atmosphere. The terrestrial solar spectrum radiates in a broad wavelength range of 300 to 2500 nm, in three general ranges of ultraviolet (UV) (200-400 nm), visible (400-700 nm), and infrared (IR) (700 to 2000 nm) [9]. Terrestrial solar radiation includes 7% of UV light, 50% visible and 43% IR light [10]. Photosynthetically active radiation (PAR) which ranges from 400 to 700 nm is the light array benefiting photosynthesis process. The light ranges which are best absorbed by chlorophylls to start the photosynthesis reaction are blue and red light in the visible with wavelengths of 380 to 480 nm and 600 to 700 nm, respectively [3].

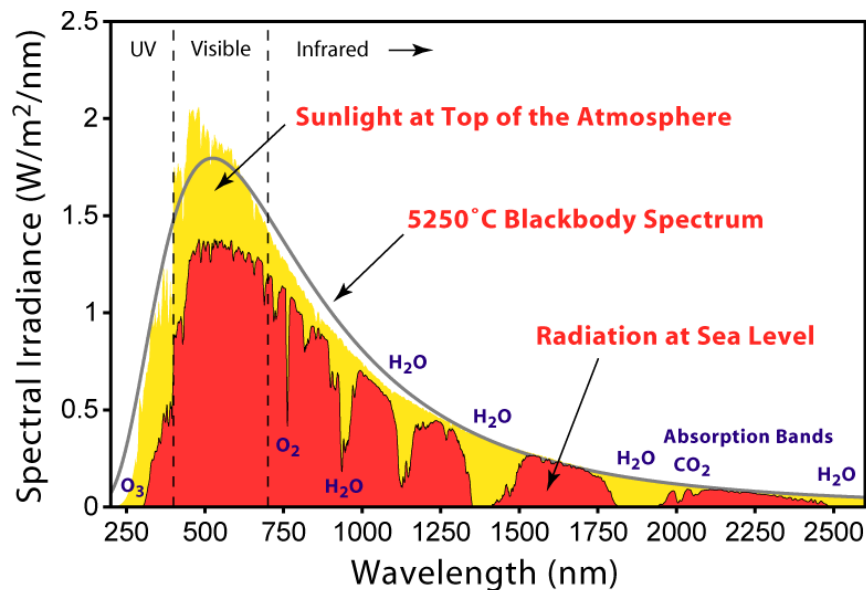


Figure 1. Solar spectrum in space, caused by the sun's blackbody radiation at 5250°C, as well as the terrestrial spectrum and sun radiation at sea level.

https://upload.wikimedia.org/wikipedia/commons/4/4c/Solar_Spectrum.png Copyright (2020).

1.3. Greenhouse Cover Materials

There have been challenges for growers and the cultivation industry to optimize the plant growth rate and protect the plant from environmental conditions. One of the concerns is regarding the enhancement of the light range promoting the photosynthesis process or PAR [11]. Glass (SiO_2) used to be the most common material employed as greenhouse covers in the 20th century. However, the high fuel cost associated with its production led to polymers emerging as more efficient greenhouse cover materials [12]. The most well-known polymer for greenhouse application is polyethylene (PE) [11][13][14][15] while other polymers such as polyester [16][17], polyvinyl chloride (PVC) [18], etc. have been extensively studied.

To enhance the properties of greenhouse sheets, adding various types of additives for different purposes have been suggested such as adding UV stabilizers to increase the durability of polymers [19][20]. The manipulation of optical properties of the material to achieve photoselectivity by blocking the UV and IR light and optimizing PAR light has been practiced by using additives that act as UV and IR absorbers [19]. In this contribution, since luminescence europium (Eu) complex absorbs UV light and emits in the red spectral region, Nordin et al. presented a study on a polymer so called Eu (TTA)₃phen doped PE films with different ratios of Eu (TTA)₃phen complex to PE ranging from 0 to 0.2 %. The optical properties were investigated by studying fluorescence spectra using an excitation source with a wavelength of 394 nm. The spectral measurements showed that with

increasing the Eu (TTA)₃phen to PE ratio, the PL emission corresponding to $^5D_0 \rightarrow ^7F_2$ transition of Eu^{3+} was more intense which is responsible for the red light emission [12].

One of the factors that increases the temperature inside the greenhouses leading to the burn or even death of the plants is trapping IR light which has a longer wavelength compared to visible light and if transmitted through the greenhouse covers it causes extensive temperature rise inside the greenhouses in normal or hot climate regions [21]. As a solution, Aldaftari et al. modeled different coatings with a variety of performance rates where the IR light is reflected and visible light passes through the material [21].

Although the polymer materials have been studied extensively and their properties have been enhanced, there are still challenges that in some aspect make glass more interesting for greenhouse application. In plastic materials multi-layering is one of the strategies for heat retention which is one of the important parameters for plant growth, however, it leads to less transparency of the material which consequently brings about compromising light transmission required for photosynthesis [22]. Another disadvantage of plastic materials is the fact that IR transmission is higher compared to glass. In addition, glass shows the highest heat protection with transmitting PAR light and reflecting IR light [23]. Besides, Polymers need to be UV stabilized and the additives used as UV stabilizers are made of heavy metals namely lead and cadmium which are hazardous to human health. One of the main disadvantages of the polymer based greenhouse covers is that without UV stabilizers they last only a few months [21], [24], [25].

Thin film technology has brought many advantages into light in numerous fields such as microelectronics, solar cells, photonics, and optics [26]. Transparent thin films with thickness below 200 nm are another solution for manipulating and optimizing the

properties of greenhouse sheets. Thin films are promising in absorbing UV radiation and consequently sustaining resistance against degradation while allowing PAR transmission [27].

Thin film fabrication can be performed by several different deposition methods which are categorized as physical vapor deposition (PVD) such as sputtering and evaporation, chemical vapor deposition (CVD), and completely chemical techniques like sol-gel [26], [28]. The challenges associated with purely chemical techniques are the lack of uniformity and poor control over the quality of the thin films which makes this technique unappealing for optical thin films [28].

1.4. Conventional and Novel Deposition Systems

Sputtering as one of the deposition techniques has been used for enhancing the desired properties of materials for the semiconductor industry for many years now. The downsides of the conventional sputtering, which are extreme temperature rise on the substrate, low rate of deposition, and low efficiency of ionization in the presence of plasma, restricts the use of this technique. To address these challenges, magnetron sputtering is introduced where the substrate and target are placed parallel and using a sputtering gun, through which energetic ion particles bombard the target's solid surface to knock off the surface atoms, and the films are fabricated. This technique relies more on physical reaction rather than chemical. Although magnetron sputtering enables high control over producing films with a wide range of thickness it can also lead to major broken bonds and a low rate of deposition compared to CVD which limits fabrication of complex, high quality, and high-density films [28], [29].

In the CVD system, the driving force of the process is the high temperature of the substrate where the film is grown while the precursor gases chemically react. The high temperature required in this deposition method restricts its application for low melting point materials and polymers. Therefore, the alternative technique of plasma enhanced chemical vapor deposition (PECVD) is proposed where instead of high temperature, plasma supplies the energy needed to dissociate the bonds of the precursor gases, and the free radicals are adsorbed on the substrate surface and the thin film are grown [28]. Z. Khatami et al. introduced the novel and customized system of integrated magnetron sputtering and electron cyclotron resonance plasma enhanced chemical vapor deposition (IMS-ECR-PECVD) to minimize the deficiencies related to each equipment (magnetron sputtering technique and ECR-PECVD system) [30]. Conventionally, in-situ doping in PECVD system is performed by metal organic powder (MOP) sources which are heated in heating jackets and the ions evaporate and enter the deposition chamber. The main drawback of this method is that the amount of doped elements cannot be accurately controlled since it is extremely susceptible to the temperature of the heating jackets which makes the duplication of the samples challenging [28], [30], [31]. By fabricating terbium (Tb) doped SiO_x thin films, it was shown that IMS-ECR-PECVD is highly adjustable and the concentration of RE dopant is directly dependent on the deposition parameters especially sputtering power therefore, the RE concentration can be easily controlled via the deposition parameters. Besides, another drawback of the common in-situ doping, the MOP method, is the H contamination [30].

1.5. Silicon as a Light Emitter

Light emission involves generating electron-hole pairs, which takes place when light is absorbed by a medium (absorption) and excites the electrons from the ground states to higher electronic energy levels; the return of the electron to its original (ground) state (recombination) is accompanied by releasing the energy as a photon. Recombination is the reverse process of absorption. The light emission occurs when the electron in the conduction band recombines with the hole in the valence band. The conservation of energy and momentum has to be considered in the recombination process. Materials with direct bandgaps have their minimum of the conduction band and the maximum of their valence band in the same momentum space. Therefore, when the excited electron in the conduction band reoccupies the hole in the valence band, photon can directly be emitted with no need of momentum for electron to fall from conduction band to valence band (shown in Figure 2).

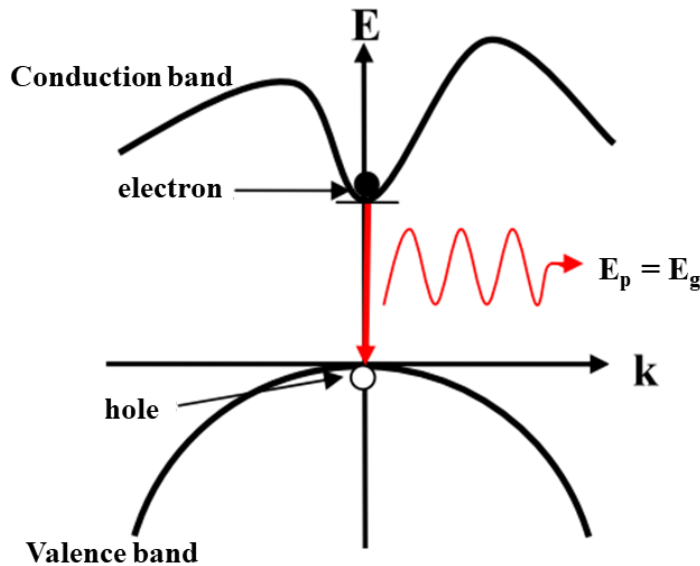


Figure 2. Recombination pathway in direct bandgap materials. The energy of the photon (E_p) is equal to the bandgap energy (E_g) [32].

The general problem with bulk Si as a light emitter is its electronic configuration making it an indirect bandgap material and consequently a poor light emitter. In indirect bandgap materials, the minimum of the conduction band and the maximum of valence band are offset and to have electron-hole recombination, there is a phonon interaction with energy of E_q required to conserve the momentum; and light particle (photon) emission is needed for the conservation of the energy [33] (shown in Figure 3). The required phonon interaction along with a longer recombination lifetime of indirect bandgap materials compared to direct bandgap materials lead to a lower probability of radiative recombination in indirect bandgap materials. The radiative lifetime of Si is in the order of milliseconds which is longer than direct bandgap semiconductors such as GaAs which have a radiative lifetime of 40 ns. When the electrons recombine with the holes in addition to the radiative pathway, they can go through non-radiative recombination pathways. Based on the radiative (τ_r) and non-radiative lifetime (τ_{nr}), the efficiency of the photoluminescence (η) (light emission) is given by the following equation 1:

$$\eta = \frac{\tau_{nr}}{\tau_{nr} + \tau_r}$$

eq.1

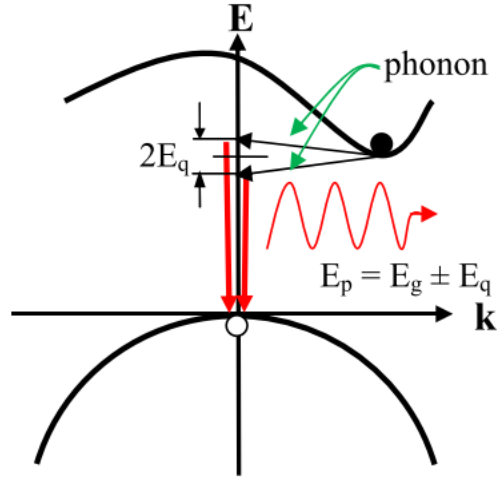


Figure 3. Recombination pathway in indirect bandgap materials with photon interaction [32].

1.6. Rare Earth Doped Silicon Nanostructures

Ease of engineering of Si, enables the opportunity to modify the Si nanostructure and its bandgap to obtain a potential light emitter and consequently, its poor light emission properties can be sorted out. One approach to address this challenge is through RE doping. Trivalent RE ions have allowed 4f transitions, which offers a high probability of occurrence, and their luminescence appears as bright and sharp emission lines. The 4f shielding of the RE elements makes the energy levels independent from the host material [34], [35].

Among RE elements, cerium (Ce), terbium (Tb) and europium (Eu) serve as blue, green, and red light emission, respectively, and together they can deliver the RGB (white) spectrum for display and LED applications. Using these RE elements as dopants in Si matrices makes it viable to have transition in the RE ions' electron levels therefore,

obtaining the desired emission because of the wavelength associated with their electron structure [32].

Even though the optical properties of Ce and Tb doped Si-based thin film are not studied in this study, a brief review of the luminescence Ce and Tb doped Si films is conducted. The combination of Ce and Tb color emission with Eu emissions provides a white spectrum for lighting applications. In the presence of RE elements in the Si nanoclusters (Si-ncs) host, when the nanoclusters are excited, the energy can transfer to the RE ions and de-excitation occurs radiatively in the wavelength corresponding to the RE ion emission [35]. Besides the radiative recombination in rare earth emission wavelengths as a result of transferred energy from Si-ncs, defect related energy can also be transferred and lead to radiative recombination [36]. The most outer electrons in $5s^2$ and $5p^6$ of the RE elements are shielded by the 4f shielding, which makes the energy levels of REs insensitive to the host materials. In the RE doped materials, the RE element occupies the sites having identical electronic configurations and absorbs the free carriers by the electrons in the 4f shell where the electrons are excited to higher energy levels. During the relaxation i.e. the excited electron returns to its valence band, the excess energy is emitted in the form of photons with the specific wavelength corresponding to the bandgap of the RE energy level [32].

Figure 4 shows the energy levels of trivalent Tb and Ce. In a study by Y. Gao et al. the luminescence properties of Ce doped SiO_xN_y , Ce doped SiO_x and Ce doped SiN_x films with a variety of elemental compositions were investigated. The samples were produced by identical ECR-PECVD and MOP setup used for this project. Using RBS measurements, it was indicated that the concentration of Ce was ranging from 0.5 to 0.9 at.%. The highest

PL intensity was observed for the samples annealed at 1200°C due to the formation of nanoclusters containing Ce. The brightest sample was fabricated using pure N₂ as the precursor gas when subjected to post deposition annealing at 1200°C and N₂+H₂ ambient (shown in Figure 5). The composition of CeSiN-pure which represents the highest PL intensity was reported to be 22.3, 48.6, 5.2, and 0.5 at. % for Si, O, N and Ce, respectively [37].

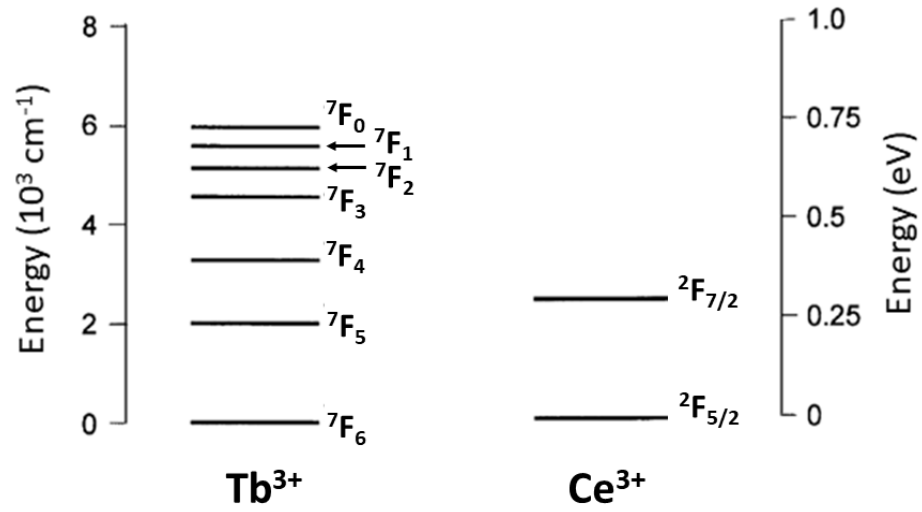


Figure 4. Energy levels of trivalent Tb and Ce oxidation states correspond to green and blue light, respectively [34].

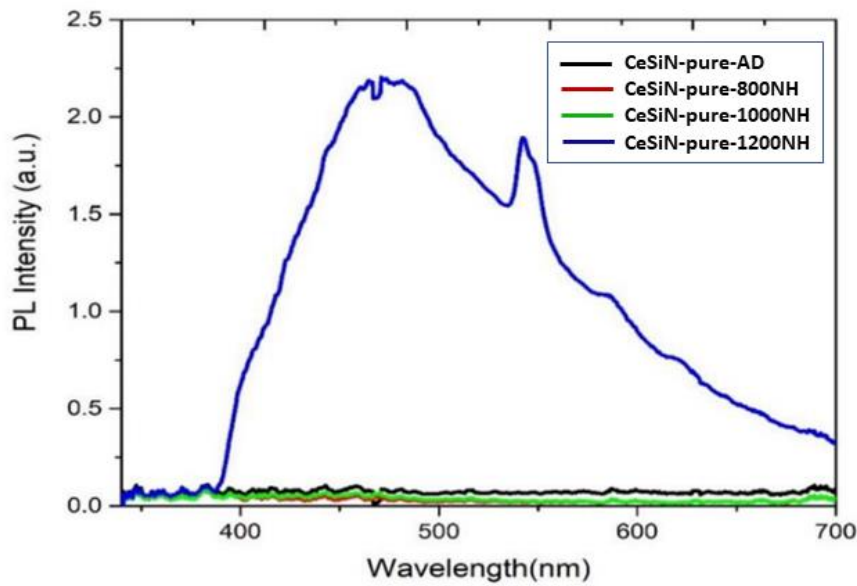


Figure 5. PL measurements of the as-deposited and annealed CeSiN-pure using N_2+H_2 atmosphere at temperatures ranging from 800 to 1200°C [37]

One of the former students in Dr. Mascher's group, P. R. J. Wilson, studied the optical and structural properties of Ce and Tb co-doped SiO_x thin films. The association of highest PL intensity at elevated annealing temperature was observed because of nanocrystals formation which was confirmed by transmission electron microscopy (TEM). Additionally, P. R. J. Wilson et al. noticed that in the presence $Ce_2Si_2O_7$ crystals, the Tb related PL emission was enhanced and this was ascribed to the transformation of energy among Ce nanoclusters and Tb energy levels by performing X-ray absorption near edge structure (XANES) performed in the Canadian Light Source (CLS) located in the University of Saskatchewan [38].

The energy level of atoms is defined by their electron configuration and is labeled by an integer as the shell number (1, 2, 3, ...), a lower-case letter as the sub shell (s, p, d, f, ...) and followed by another integer as the number of electrons in the subshell. In addition to the electron configuration of the RE ions, their energy level is also defined by the term symbols ($^{2S+1}L_J$) where S is the ion spin and 2S+1 is the possible orientation of the total ion spin, L is the orbital angular momentum, and J is the total angular momentum [34].

The energy levels of divalent and trivalent oxidation states of Eu are shown in Figure 6. Emissions related to Eu^{2+} are generally broad peaks sitting between 400 to 550 nm ascribed to $4f^6 5d^1$ to $4f^7$ [39]. Eu^{3+} emission, on the other hand, arises from f-f transitions. The emission from the Eu^{3+} ion derives from the excitation of 5D_0 to 7F_J level. The Eu^{3+} emission is in the red region with the wavelengths of 585 and 615 nm from the transition of 5D_0 to 7F_1 and 5D_0 to 7F_2 , respectively [39], [40].

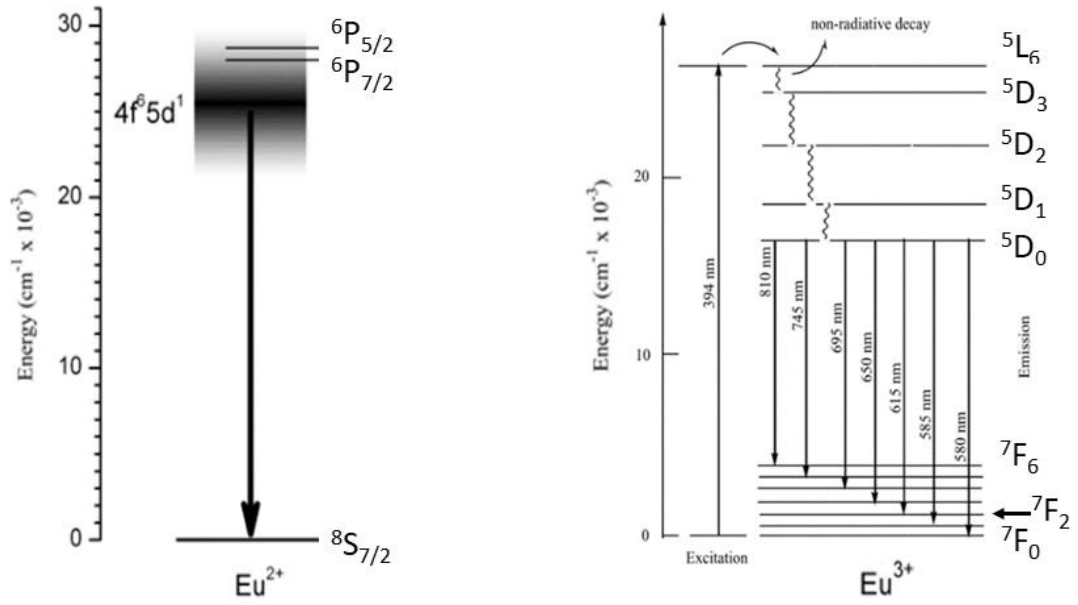


Figure 6. Energy levels of a) Eu^{2+} [39] and; b) Eu^{3+} ion with the associated wavelength and the energy levels [40]. An excitation source with 394 nm promotes the excitation of electrons in the f level and the potential photon emissions, when the electron drops back to the valence band again.

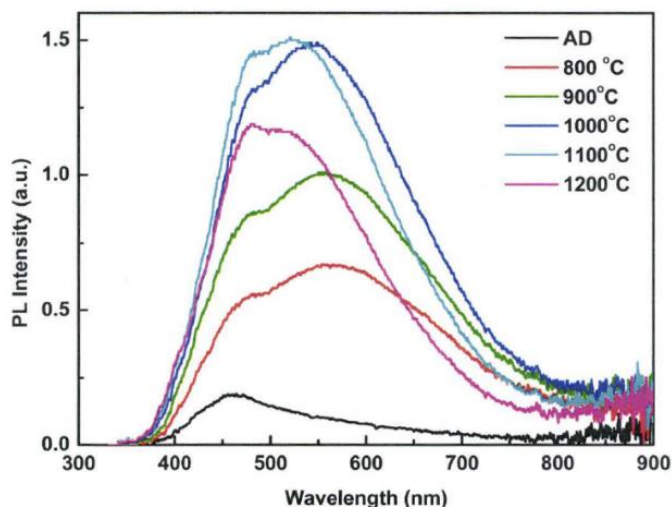


Figure 7. PL measurements of Eu doped Si-rich SiO_x thin film for the as-deposited and annealed samples using N₂ ambient at temperatures ranging from 800 to 1200°C in 100°C increments for 1 hour [41].

J. Li studied the PL of a variety of RE elements (Er, Eu, Tb and Ce) doped in SiO_x matrix with and/or without excess Si, fabricated using ECR-PECVD. PL measurements of an Eu doped Si rich SiO_x film with a composition of 34.48 at. % of Si and 0.12 at. % Eu for the deposited and annealed samples at different temperatures ranging from 800 to 1200°C and N₂ atmosphere, is shown in Figure 7. A broad peak is observed in the range of 400 to 800 nm. Since the peak is not symmetric, suggesting the possibility of different luminescence centers that might be related to the defects, Eu²⁺, Eu³⁺, or Si-ncs [41]. Gaussian deconvolution divides the peak in red (shown in Figure 8) into three peaks to investigate the sub-peaks constituting the red peak. Peak 1 and 2 can either be related to Eu²⁺ luminescence centers or the oxide defects. However, after annealing less defect related luminescence centers are expected to be observed. The luminescence centers at peaks 1 and 2 can be attributed to Eu²⁺ emission which occurs as a broad band at 400 to 600 nm

corresponding to $4f^6-5d^1$ transition. Regarding peak 3, considering its wavelength, it is associated with the Eu^{3+} or Si-ncs luminescence centers. However, the Eu^{3+} emission appears as sharp emission lines; thus, it should be ascribed to the Si-ncs defects which are comparable with the same wavelength [41].

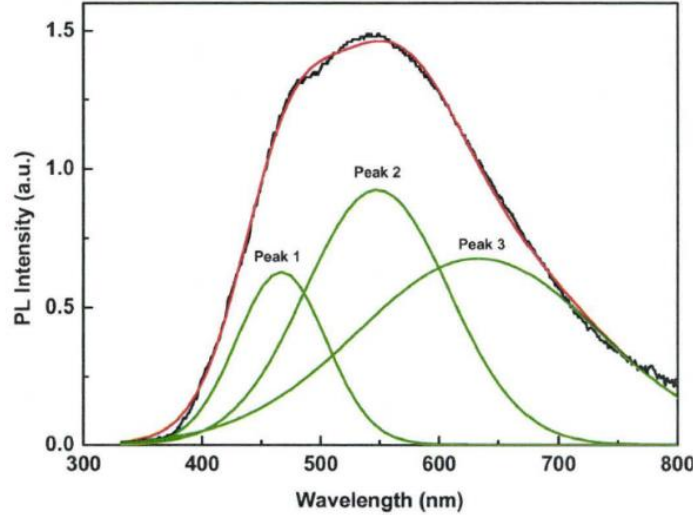


Figure 8. Gaussian deconvolution of PL spectrum of the Eu doped Si-rich SiO_x film annealed at 1000°C (for 1 hour) using N_2 atmosphere [41].

Mariscal-Jimenez et al. studied the influence of the O content in the EuO_x matrices. They investigated the light emission of EuO_x and O rich EuO_x nanocrystals fabricated on Si substrate using pulsed laser deposition with a layer of Al_2O_3 on the films to protect it from changing structure due to the atmospheric reaction. It was observed that the PL emission changed based on the O content and the surrounding of the nanocrystals. For EuO , mainly Eu^{2+} transition is observed as broad peak emission. Sample $\text{EuO}_{1.2}$ showed a mixture of both Eu^{2+} and Eu^{3+} emissions and $\text{EuO}_{1.4}$ showed only narrow band emission corresponding to Eu^{3+} transition (shown in Figure 9) [42].

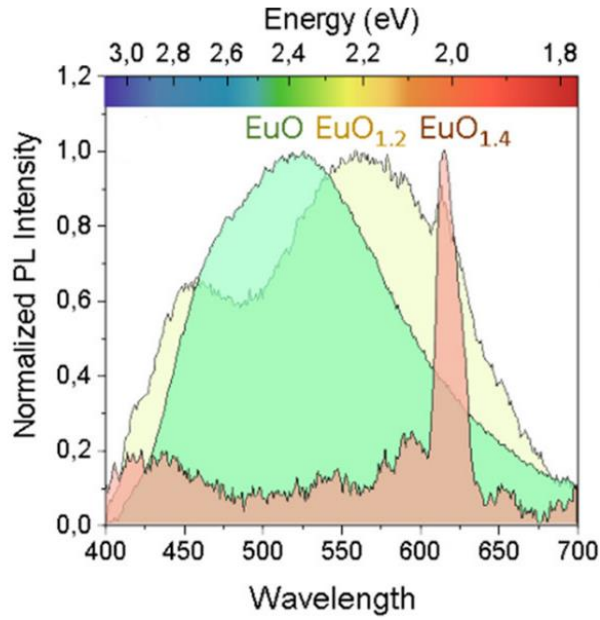


Figure 9. PL measurements of the as-deposited EuO, EuO_{1.2}, and EuO_{1.4} thin films fabricated using pulsed laser deposition [42].

1.7. Thesis Outline and Contributions

In this thesis, a number of Eu doped O rich SiO_x (ORSO), compared to the stoichiometric SiO₂, thin films were fabricated using IMS-ECR-PECVD system for the first time and the optical and structural properties of the samples were investigated thoroughly. The observation of Eu³⁺ transition emission in these thin films can lead to potential candidates serving as the cover materials for greenhouse applications in the future.

The elemental composition of the samples was detected using Rutherford backscattering spectroscopy (RBS) measurements and it is verified that at higher sputtering power, higher Eu concentration is achieved. Variable angle spectroscopy ellipsometry (VASE) was performed to investigate the refractive index and thickness of the thin films. PL measurements were conducted for the annealed and the as-deposited thin films and the

differences in their PL properties as the result of different elemental composition and annealing condition are studied. The structure of the samples was studied by X-ray diffraction (XRD) analysis and TEM where the correlation of the thin film structure with their PL properties is discussed.

The deposition system, as well as the doping techniques used for fabricating the samples studied in this thesis, the condition of post-deposition annealing, and the deposition parameters of the samples fabricated, are discussed in Chapter 2. Chapter 3 gives the fundamental description of RBS and elastic recoil detection (ERD), VASE, PL, XRD, and TEM. Chapter 4 presents a comprehensive study of the characterization and optical properties of the samples where the correlation of the deposition parameters with the thickness, refractive index and composition of the thin films is discussed. Additionally, the changes in the PL intensity of the different samples as a result of annealing conditions and their elemental composition is studied. The structural properties and the crystalline phases formed in the annealed samples are discussed in Chapter 5. The last chapter, Chapter 6, provides the conclusion and suggests further potential studies.

Chapter 2: Methodology

The purpose of this chapter is to provide the detail of the thin film preparation and introducing the samples fabricated with different deposition parameters. This chapter starts with describing the novel deposition system of IMS-ECR-PECVD and gives a brief description of the conventional in-situ doping in the ECR-PECVD system. Then explains the post-deposition annealing procedure and the condition in which the samples were annealed. The following introduces two sets of samples, one fabricated using IMS-ECR-PECVD and the other one using the conventional ECR-PECVD system.

2.1. Deposition System

The fabrication system used in this work was the IMS-ECR-PECVD system (shown in Figure 10). In this regard, ECR-PECVD system is used for the deposition of the SiO_x thin films, while the in-situ doping of Eu is performed using a sputtering gun that was embedded in the ECR-PECVD chamber [30]. A 3-inch $\langle 100 \rangle$ oriented, n-type Si substrate (shown in Figure 12) is placed in the load lock chamber. Using a turbo pump the load lock chamber is highly vacuumed, dropping the pressure to 10^{-6} Torr to evacuate the atmospheric gases and providing a pressure low enough that allows us to expose the main chamber to the load lock region. The substrate is then transferred to the sample stage inside the ECR-PECVD chamber. Prior to the thin film deposition, using diffusion or turbo pumps, the chamber is evacuated to an ultra-high vacuum pressure of 10^{-9} Torr. Next, the precursor gases, which in this case are 30% of SiH_4 and 10% of O_2 both diluted in Ar, are fed into the chamber and are directed to the substrate by the dispersion ring. To obtain uniformity in the

deposited thin films, during the deposition process the sample stage rotates with the rate of 20 revolutions per minute (rpm). The temperature of the sample stage was set at 350°C which results in the substrate temperature of 120°C [43]. The plasma is empowered with a microwave power source to impart the precursor gases turning them into free radicals which are consequently absorbed on the substrate and chemically react.

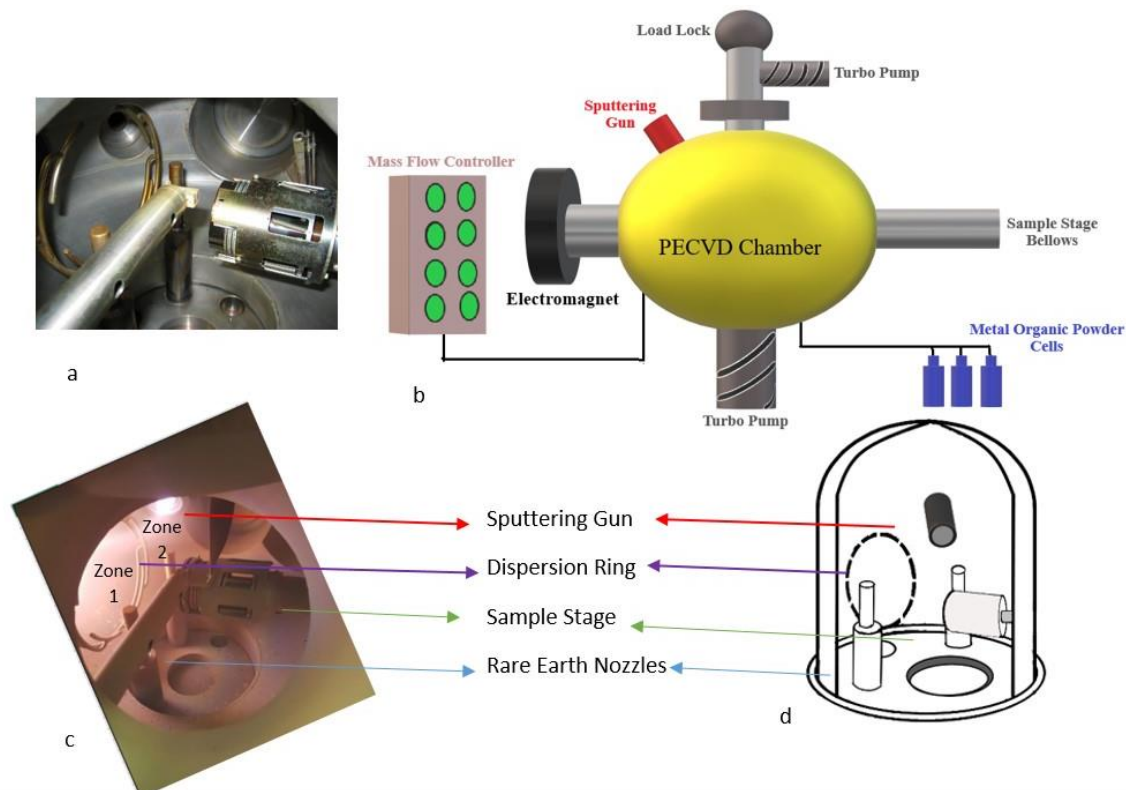


Figure 10. Integrated magnetron sputtering and electron cyclotron resonance plasma enhanced chemical vapor deposition (IMS-ECR-PECVD) system. a) The interior area of the deposition chamber; b) a schematic of the exterior area of the ECR-PECVD system including metal organic powder and sputtering gun installed; c) and d) image and schematic of the interior area showing the orientation of the sputtering gun, dispersion ring, sample stage, and the rare earth nozzles [44].

Figure 11 shown the detailed schematic of the PECVD system which was studied by one of the PhD students in Dr. Mascher team and calibration of the system is provided comprehensively. At atmospheric pressure (760 Torr) the Si wafer is placed in the load

lock chamber and using a turbo pump (Figure 11), the load lock area reaches high vacuum pressure (10^{-6} Torr) which is in the range of desired pressure in the main chamber. Then the load lock gate is opened, and the wafer is inserted to the PECVD chamber and placed on the sample stage. The pressure in main chamber dropped to ultra high vacuum level (10^{-9} Torr) using another turbo pump (shown in the Figure 11). The diffusion pump is only a backup system. More information about the system can be find in [28].

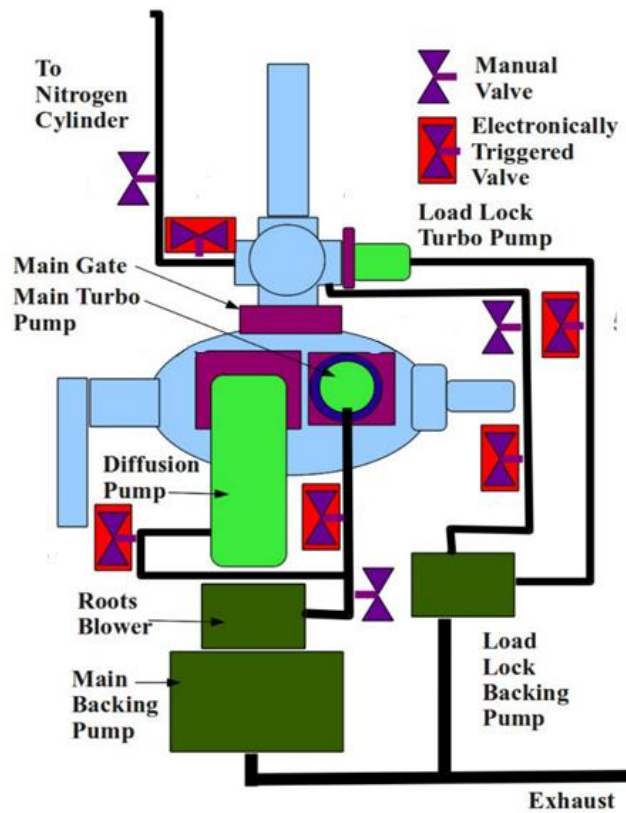


Figure 11. A simplified schematic of the PECVD system [28].

For in-situ RE doping, the conventional method involves using metal organic powder (MOP) where the canisters, containing volatile RE metal organic powder, are heated in heating jackets. The amount of RE elements entering the deposition chamber is controlled

by the temperature of the heating jackets (shown in Figure 13). In the customized IMS-ECR-PECVD system, the sputtering gun is used to perform the in-situ doping. The sputtering gun bombards the RE target, knocking out the atoms by accelerated ions which consequently are incorporated into the growing layer.

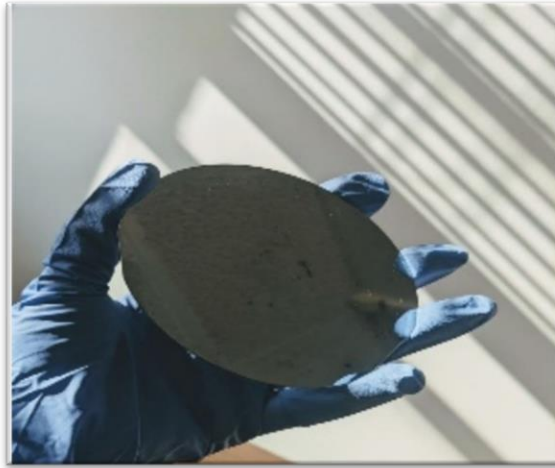


Figure 12. A 3 inch $\langle 100 \rangle$ oriented Si substrate used for the deposition.



Figure 13. MOP canisters and the heating jackets inside which the canisters containing MOPs are heated, and the evaporated RE gases are fed into the ECR-PECVD chamber. The temperature is controlled using a K-type thermocouple [28].

2.2. Fabricated Thin Films

In this work, a set of nine Eu-doped SiO_x thin films was fabricated on $\langle 100 \rangle$ oriented, n-type Si wafer as well as glassy C substrate using the IMS-ECR-PECVD system with different deposition parameters (shown in Table 1). The Eu target used was 99.9% purity. The IMS-ECR-PECVD system is located at Tandem Accelerator Building in McMaster University, Centre for Emerging Device Technologies (CEDT). Deposition time, O_2 gas flow rate, and microwave power of plasma were 60 minutes, 25 standard cubic centimeters per minutes (sccm) (where the standard temperature and pressure are 20°C and 1 atmosphere), and 500 W, respectively, and were set constant for all the samples. The variable deposition parameters, for fabricating different thin films, were SiH_4 flow rate varying from 1.5 to 2.5 sccm, the sputtering Ar flow rate of 10 to 40 sccm, and sputtering power ranging from 10 to 40 W (shown in Table 1). Using the variable deposition parameters while keeping the remaining deposition parameters constant, enables us to investigate the role of each variable parameter on the properties of the thin films.

Table 1. Deposition parameters of a set of nine thin films fabricated using IMS-ECR-PECVD system. The plasma power is 500 W, the O₂ gas flow rate is 25 sccm, and the deposition time is 60 minutes for all the samples.

IMS Samples	30%SiH ₄ /Ar [sccm]	Sputtering Ar [sccm]	Sputtering Power [W]
52-Eu _{1.0} Si _{35.0} O _{64.0}	2.5	40	20
53-Eu _{4.4} Si _{26.2} O _{69.4}	2.5	40	40
54-Eu _{0.2} Si _{31.9} O _{67.9}	2.0	40	10
55-Eu _{0.8} Si _{31.4} O _{67.8}	2.0	10	10
56-Eu _{0.2} Si _{34.2} O _{65.6}	1.5	10	10
57-Eu _{1.5} Si _{32.8} O _{65.6}	2.0	40	20
58-Eu _{1.5} Si _{34.4} O _{63.5}	1.5	40	20
59-Eu _{0.3} Si _{34.3} O _{65.4}	1.5	40	10
60-Eu _{6.4} Si _{25.7} O _{67.9}	2.0	40	40

A set of MOP samples were also fabricated previously and are presented in Table 2 along with their deposition parameters.

Table 2. Deposition parameters for a set of six samples fabricated using ECR-PECVD system and in-situ doping using MOP procedure.

MOP Samples	SiH ₄ /Ar [sccm]	O ₂ /Ar [sccm]/[mTorr]	Eu Cell Temp [°C]	Deposition time [min]
37-Eu ₀ Si _{31.53} O _{68.27}	2.5	25/2.90	142	60
38-Eu _{0.01} Si _{35.95} O _{58.61}	2.5	25/2.85	170	40
39-Eu _{0.46} Si _{35.77} O _{63.61}	2.5	30/3.35	196	60
41-Eu _{0.04} Si _{28.86} O _{69.69}	1	30/3.10	170	60
43-Eu _{0.31} Si _{31.25} O _{67.94}	1	30/3.3	198	60
44-E _{0.46} Si _{21.64} O _{76.96}	1	20/2.35	198	60

2.3. Post Deposition Annealing

Followed by the fabrication, the samples were cleaved and subjected to post deposition annealing in a quartz tube furnace (QTF) (shown in Figure 14). The furnace was heated gradually by ramping up the temperature to reach the desired annealing temperature. In the meantime, Ar gas flow was used to vent the tube from atmospheric gases and obtain an inert gas ambient which protects the samples from oxygen contamination. The samples were annealed by placing samples inside a 1-inch quartz tube using a quartz rod and a quartz boat. A schematic of the quartz tube furnace is shown in Figure 15.

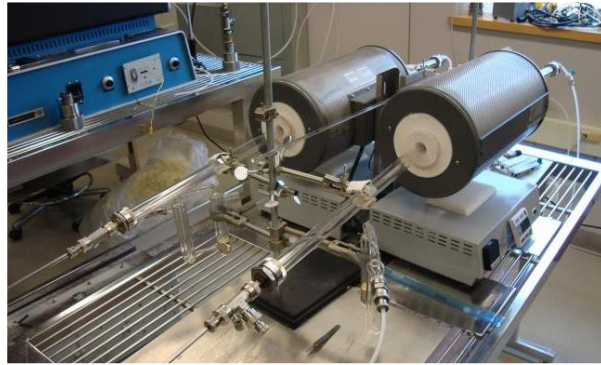


Figure 14. Quartz tube furnace used for post deposition annealing.

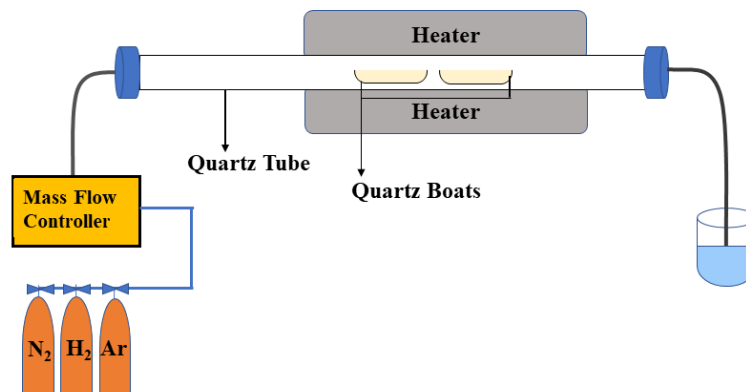


Figure 15. A schematic of quartz tube furnace with the annealing gases of Ar, N₂, and H₂.

To study the effect of H passivation and the influence of annealing temperature on the PL properties, the post deposition annealing was performed at two different annealing ambients of pure N₂, and forming gas with 95% of N₂ and 5% of H₂ (N₂+H₂), at different temperatures ranging from 300 to 1350°C. To avoid the atmospheric gas reaction with the annealed thin films, following the annealing, the samples are cooled off to room temperature outside the heating area of the furnace under the N₂ gas flow.

The as-deposited Eu doped ORSO thin films are originally amorphous. Annealing the samples at elevated temperatures results in the phase separation of metastable amorphous SiO_x. This can emanate through nucleation and/or spinodal decomposition where the SiO_x phase, separates into two phases [45] and induces the formation of Eu_xSi_yO_z crystalline structure embedded in the SiO_x matrix (shown in Figure 16). The formation of these Eu_xSi_yO_z crystals promotes the Eu ions to become optically active by the opportunity provided with the Si-based nanocrystals to transfer the energy (Forster-Dexter energy transfer). This energy transfer is required for the excitation of electrons in the 4f shell energy levels of Eu and generating PL emissions corresponding to Eu ion transitions.

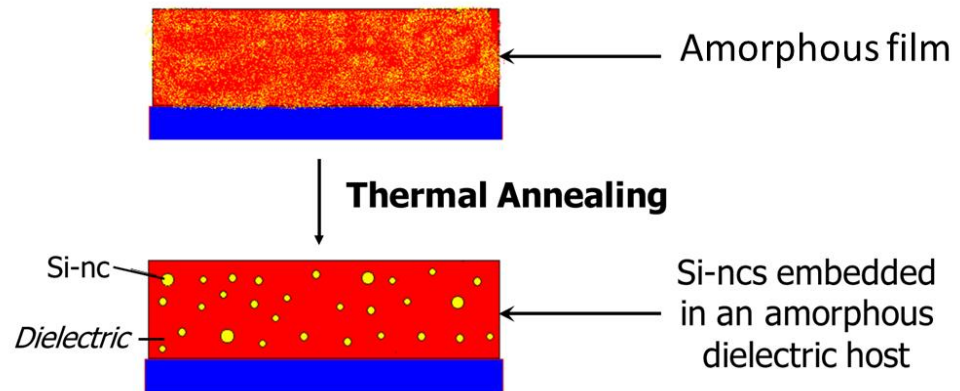


Figure 16. The formation of Si-ncs in the as-deposited amorphous SiO_x thin film when subjected to post deposition annealing. High annealing temperature results in phase separation within the film and promotes the formation of Si-ncs. Adapted from [32].

Chapter 3: Characterization Techniques

This chapter presents a description of each measurement performed on the samples studied in this thesis. The measurements carried out to investigate various properties of the thin films are Rutherford backscattering spectrometry (RBS) and elastic recoil detection (ERD) to obtain the elemental composition, variable angle spectroscopic ellipsometry (VASE) to achieve refractive index and the thickness, and PL measurements where the light emission at different wavelengths are studied. In addition, the structural characterizations of the thin films are examined by X-ray diffraction (XRD) and transmission electron microscopy (TEM) measurements to detect the crystalline structures and the crystalline phases formed in the thin films.

3.1. Rutherford Backscattering Spectrometry

RBS is a non-destructive technique to determine the in-depth elemental composition of solid materials using MeV charged particles which are usually $^4\text{He}^{2+}$ ions. The $^4\text{He}^{2+}$ ion beam collides the sample and while some of the particles penetrate through the sample, some particles elastically backscatter with loss of energy. The energy of the backscattered particles is detected and indicates the number of particles as a function of energy (shown in Figure 17) [46]. In this essence, the energy of the backscattered ions varies based on the different atomic masses of the elements presented in the samples.

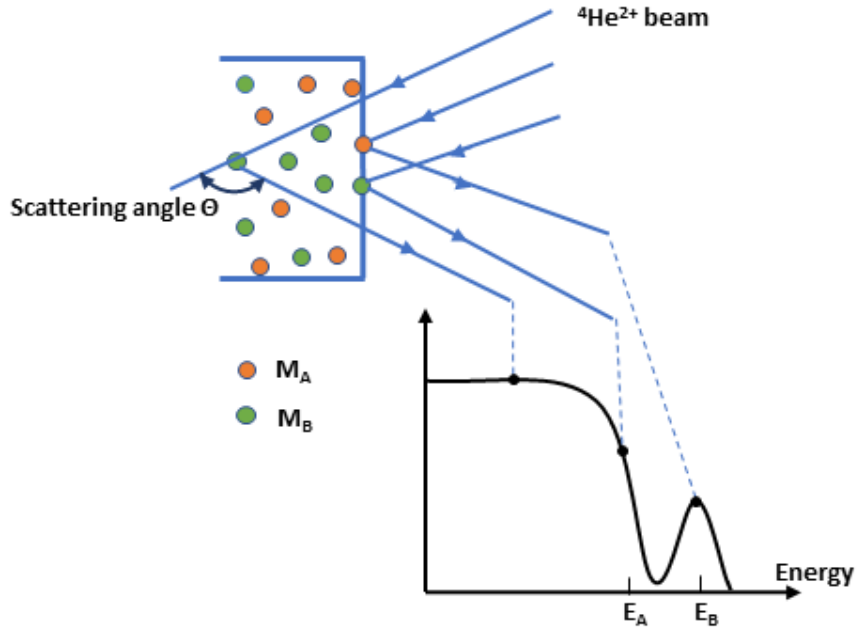


Figure 17. The schematic of the Rutherford backscattering spectrometry (RBS). Adapted from [46].

The projectile with the mass of M_1 and initial kinetic energy of E_0 interacts with the sample's stationary atom with a mass of M_2 . The kinetic energies for projectile and stationary atoms are E_1 and E_2 , respectively, and θ is the scattering angle. Kinematic factor K is the ratio of latter energy of the ion particle to its initial energy (E_1/E_0) and using the law of energy conservation is given as [47]:

$$K = \frac{E_1}{E_0} = \left[\frac{M_1 \cos(\theta) + \sqrt{M_2^2 - M_1^2 \sin^2(\theta)}}{M_1 + M_2} \right]^2 \quad \text{eq.2}$$

The preferred position for the detector is at $\theta \sim 180^\circ$ due to the fact that K sensitivity becomes maximum with small mass differences of target elements [48]. The energy loss

as a result of projectile interaction with the electron clouds of the target elements is below 100 keV and considering the high energy of incident particles (in the range of 1 to 3 MeV), it can be neglected [43], [48].

The detector was positioned at 170° (scattering angle) with the incident and exit angles of 0° and 5° , respectively, using 4 μC doses of 1.8 MeV $^4\text{He}^{2+}$ ions. To achieve a more accurate simulation, the samples used for these measurements were deposited on a glassy (vitreous) C substrate. Using C substrate improves the signal to background level which is beneficial for distinguishing the lighter elements without overlapping with the signal coming from the substrate, in this case, Si [49]. Figure 18 shows representative RBS spectrums of the same sample deposited on C (Figure 18 (a)) and Si substrate (Figure 18 (b)).

The SIMNRA package software was used for the quantitative analysis of all the RBS spectra for the thin films presented in this thesis. Details on the SIMNRA data simulation are given in [50].

One of the limitations of RBS measurement is that due to low sensitivity it cannot detect elements lighter than the beam (He) which leads to the requirement of other complementary measurements such as elastic recoil detection (ERD) [48].

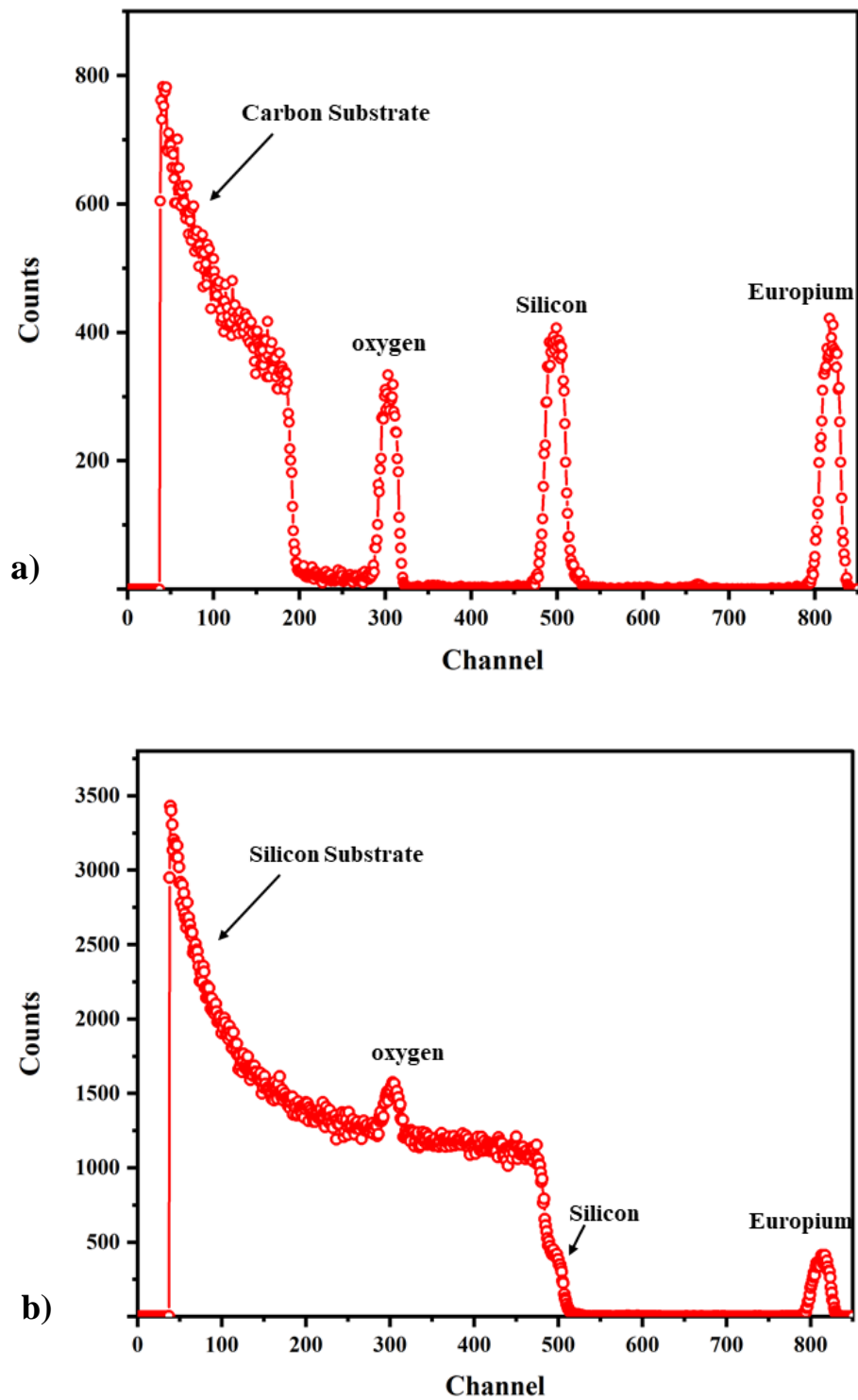


Figure 18. Representative RBS spectra of an identical sample ($57\text{-Eu}_{1.5}\text{Si}_{32.8}\text{O}_{65.6}$) deposited on a) C substrate; b) Si substrate.

3.2. Elastic Recoil Detection

ERD analysis is a complementary measurement to RBS to detect the concentration of the lighter elements which in this case is H. The RBS and ERD measurements for this thesis were performed at Tandetron Accelerator Laboratory located at Western University in London Ontario, Canada, which is equipped with several beamlines. Each beamline provides different energy distribution of the ion beam. For the ERD measurements, 2 μC doses of $^4\text{He}^{2+}$ ion beam with energy of 2.9 MeV is used. The incident and exit angles are 75° with a scattering angle of 30° . In ERD measurements all the matrix elements with higher atomic masses than He are stopped by using a foil placed in front of the detector. On the other hand, the downside of using the foil is reducing the resolution which makes ERD less accurate compared to RBS measurements [51].

3.3. Variable Angle Spectroscopic Ellipsometry

VASE is an experimental method to detect the optical properties and the thickness of thin films. VASE measurements are commonly performed on the as-deposited samples since it leads to more consistency which provides a reliable comparison between different thin films. The formation of nanoclusters in the annealed samples makes it challenging to determine the optical properties of the annealed samples.

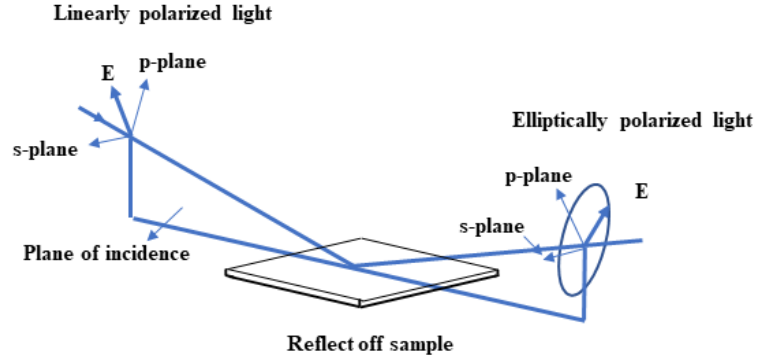


Figure 19. A schematic of VASE setup indicating the linear and elliptically polarized light, plane of the incident, and the sample position. Adapted from [52].

The principle of VASE is based on the change in the polarization of the incident light which can be either reflected or transmitted from the sample. **Error! Reference source not found.** shows a schematic of the VASE measurements. The derivatives from the polarization change of the incident light are amplitude ratio, psi (Ψ), and phase difference (Delta (Δ)), from r_p and r_s which are Fresnel's coefficients for parallel and perpendicular polarization light to the incident plane, respectively.

$$\tan(\Psi) \cdot e^{i\Delta} = \rho = \frac{r_p}{r_s} \quad \text{eq.3}$$

VASE measurement was performed at five variable angles of 55° , 60° , 65° , 70° and 75° to improve the accuracy of the measurements. Simulation of the collected data was conducted using J.A. Woollam Co., Inc. CompleteEASE package software [53]. A Cauchy model was employed for modelling the acquired data. It is suggested that the Cauchy model is suitable for obtaining the thickness and refractive index of thin films with the assumption of the films being transparent [53]. Cauchy dispersion equation is given as below:

$$n(\lambda) = A + \frac{B}{\lambda^2} + \frac{C}{\lambda^4} \quad \text{eq.4}$$

Where A, B, and C are the Cauchy coefficients, n is the refractive index and λ is the wavelength.

3.4. Photoluminescence

PL measurements indicate the PL intensity associated with different wavelengths. PL measurement is based on the excitation of electrons by an excitation source that is absorbed by the sample and can reemit by radiative recombination from the subjected material. Minimum energy of the material's bandgap is required to excite an electron from the valance band to its conduction band. As the excited electron returns to its valence band (recombination) the energy is emitted as a photon with the energy of the material's bandgap [43].

Prior to the PL measurements, a background spectrum is measured to be subtracted from the samples' measurements. In this thesis, visible PL measurements are conducted at room temperature using a He-Cd laser with a wavelength of 325 nm as an excitation source. The laser beam is pointed to a UV mirror from which the light beam is reflected and directed to the sample. The PL emission from the sample is collected by collimator lens coupling by a multimode optical fiber connected to an Ocean Optic 2000 spectrometer. Then the signal is converted and transferred to a computer by an A/D convertor. Figure 20 shows a simplified schematic of the PL setup.

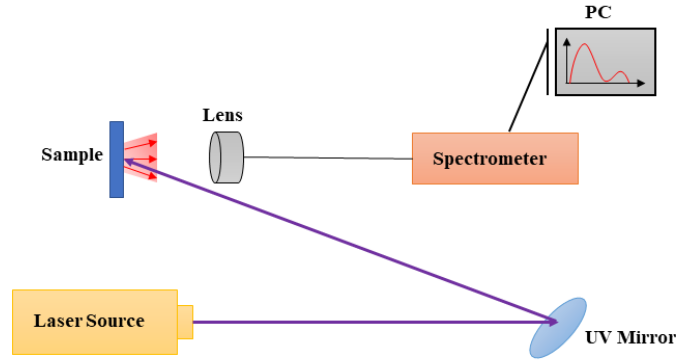


Figure 20. A schematic of PL setup. Adapted from [54].

3.5. X-Ray Diffraction

XRD measurements along with texture analysis and phase identification are performed to detect and study the crystalline structures formed in the annealed samples. The principle of XRD measurements is based on Bragg's law (diffraction condition) which says when an incident X-ray beam with a wavelength of λ and incident angle of θ interacts with the atoms of the embedded crystal structure with the distance between the layers of atoms (d spacing), the scattered beam constructively interfere, and it should follow the Bragg's equation:

$$n\lambda = 2d \sin \theta \quad \text{eq.5}$$

The XRD measurements were performed at the McMaster Analytical X-Ray Diffraction Facility (MAX) using a Bruker D8 DISCOVER diffractometer and $\text{CuK}\alpha$ sealed tube source ($\lambda_{\text{avg}} = 1.54184 \text{ \AA}$) with a graphite monochromator. The XRD patterns were collected in four frames at 15, 35, 55 and 75°, in 2θ range of 8 to 90° with 360° full rotation in ϕ (ϕ) for each frame where the detector distance was set at 20.02 cm.

The angles used during the measurements are shown in Figure 21. There are three angular rotations that are essential to recognize the orientation of the sample in the diffractometer (Figure 21 (b)): omega (ω), psi/Chi (ψ), and phi (ϕ) [55]. The sample is placed in the diffractometer center (the blue circle in Figure 21 (b)). X_L , Y_L , and Z_L are the coordination of the system, and the X-ray beam radiates on the X_L axis which is also the rotation axis of the diffraction cone since the X-ray beam and X_L axis are two coincident lines. Azimuthal angle (γ) emanates from the opposite side of the Z_L direction and is right-hand rotation with respect to the opposite direction of the X-ray beam. The half apex of the forwarded diffraction cone has the value of 2θ . The incident beam is (s_0), and (s) is the diffracted beam. Based on Bragg's law the incident vector (s/λ) makes θ angle with the diffracting plane of hkl and the H_{hkl} is diffraction vector [55].

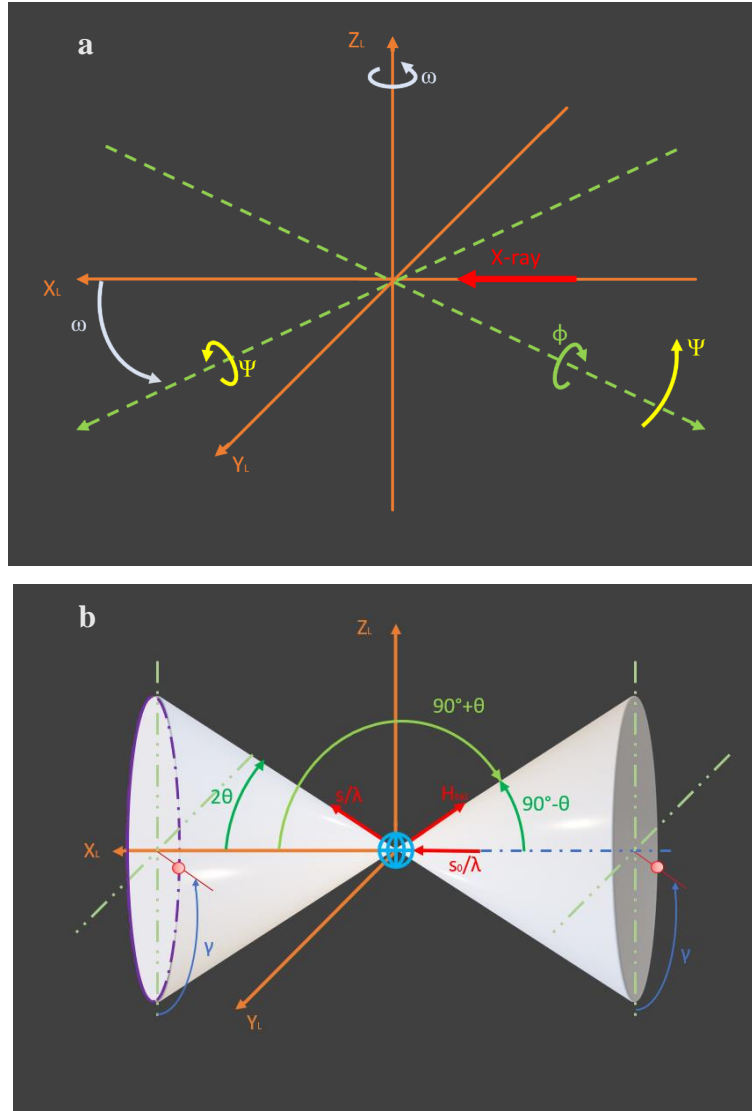


Figure 21. A schematic of; a) Angular rotations of sample orientation where X_L , Y_L , and Z_L are the system coordination and ω , ψ and ϕ are the rotational angles; b) Angles and coordination of XRD setup. (s_0) and (s) represent incident and diffracted beam, respectively, where the blue circle in the center is the sample.

3.6. Transmission Electron Microscopy

TEM captures the image of ultra-thin samples (thickness less than 100 nm) by transmitting a primary electron beam with high voltage (higher than 100 kV) through the sample. The contrast between the transmitted and scattered electrons is detected by and the image is formed. Prior to the TEM measurements, a layer of Au with a thickness of 10-20 nm is deposited on the sample in the Microscopy and Microanalysis Facility at the University of New Brunswick. Then the sample is prepared by milling a thin layer using the focused ion beam (FIB) technique to reach electron transparency thickness. In this study, TEM measurements are performed using FEI Titan 80-300 Cryo-in-situ microscopes at the Canadian Centre for Electron Microscopy (CCEM) located at McMaster University.

Chapter 4: Optical and Compositional Analyses

This chapter starts with discussing the elemental composition of the samples. Using RBS measurements, the concentration of Eu, O and Si is obtained while ERD analysis detects the concentration of lighter elements which in this case is H. Meanwhile the composition of MOP samples is compared with the IMS samples to observe the influence of the doping technique on the concentration of Eu. The thickness and refractive index of the samples are calculated by VASE measurements and the effect of deposition parameters on the thickness and refractive index is discussed. The last section of this chapter studies the PL measurement results to investigate the effect of H passivation and annealing temperature on the luminescence properties.

4.1. Elemental Composition

Carrying out RBS measurements, Eu, O and Si atomic percentage (at. %) of all the as-deposited thin films grown on C substrate with different deposition parameters were calculated. H concentration cannot be detected by RBS and therefore ERD measurements were used. For the samples in this thesis, the ERD measurements could only be analyzed qualitatively due to a technical problem in the ERD facility center. Table 3 shows the values for Eu, Si and O concentration with subtracting H concentration. The qualitative ERD measurements are discussed later in this section. Eu concentration ranges from 0.2 to 6.4 at. %, O concentration ranges between 63.5 and 69.4 at. % and Si concentration is in the range of 25.6 to 35.0 at. %. The experimental data is simulated using SMNRA package

software where the experimental data points and simulated data should make a good fit to assure acceptable accuracy [50]. The small values of uncertainties listed in Table 3 confirm the reliability and considerable precision of the simulation for all the samples.

Table 3. Deposition parameters and elemental composition of the as-deposited thin films. For all samples the deposition time was 60 minutes, microwave plasma power was set to 500 W and O flow rate was 25 sccm while the sputtering power, Ar flow rate and SiH₄ flow rate varied in the range of 10 to 40 W, 10 to 40 sccm and 1.5 to 2.5 sccm, respectively.

IMS Samples	30%SiH ₄ /Ar [sccm]	Sputtering Ar [sccm]	Sputtering Power [W]	Eu at. %	Si at. %	O at. %
52-Eu _{1,0} Si _{35,0} O _{64,0}	2.5	40	20	0.9 ± 0.1	35.0 ± 1.4	64.0 ± 6.3
53-Eu _{4,4} Si _{26,2} O _{69,4}	2.5	40	40	4.4 ± 0.1	26.2 ± 1.4	69.4 ± 0.8
54-Eu _{0,2} Si _{31,9} O _{67,9}	2	40	10	0.2 ± 0.1	31.8 ± 0.7	67.9 ± 0.8
55-Eu _{0,8} Si _{31,4} O _{67,8}	2	10	10	0.8 ± 0.2	31.4 ± 0.6	67.8 ± -
56-Eu _{0,2} Si _{34,2} O _{65,6}	1.5	10	10	0.2 ± 0.0	34.2 ± 2.0	65.6 ± -
57-Eu _{1,5} Si _{32,8} O _{65,6}	2	40	20	1.5 ± 0.1	32.8 ± 0.3	65.6 ± 3.5
58-Eu _{2,1} Si _{34,4} O _{63,5}	1.5	40	20	2.1 ± 0.1	34.4 ± 0.3	63.5 ± 3.5
59-Eu _{0,3} Si _{34,3} O _{65,4}	1.5	40	10	0.3 ± 0.1	34.2 ± 3.5	65.2 ± 3.3
60-Eu _{6,4} Si _{25,7} O _{67,9}	2	40	40	6.4 ± 0.3	25.6 ± 0.7	67.8 ± 0.4

Sometimes to obtain higher accuracy of the concentration of one certain element, one should devote the exact accuracy of the other elements. Here the relatively higher uncertainty of Si and O at. % compared to Eu at. % is because the focus was on the

concentration of Eu. However, the uncertainty values of all the elements are in an acceptable range. Figure 22 shows $60\text{-Eu}_{6.4}\text{Si}_{25.7}\text{O}_{67.9}$ as a representative of the simulated data for the samples studied in this thesis. Figure 22 shows that the simulated spectra (blue line) present a good fit with the experimental data which verifies the high accuracy of the RBS simulation.

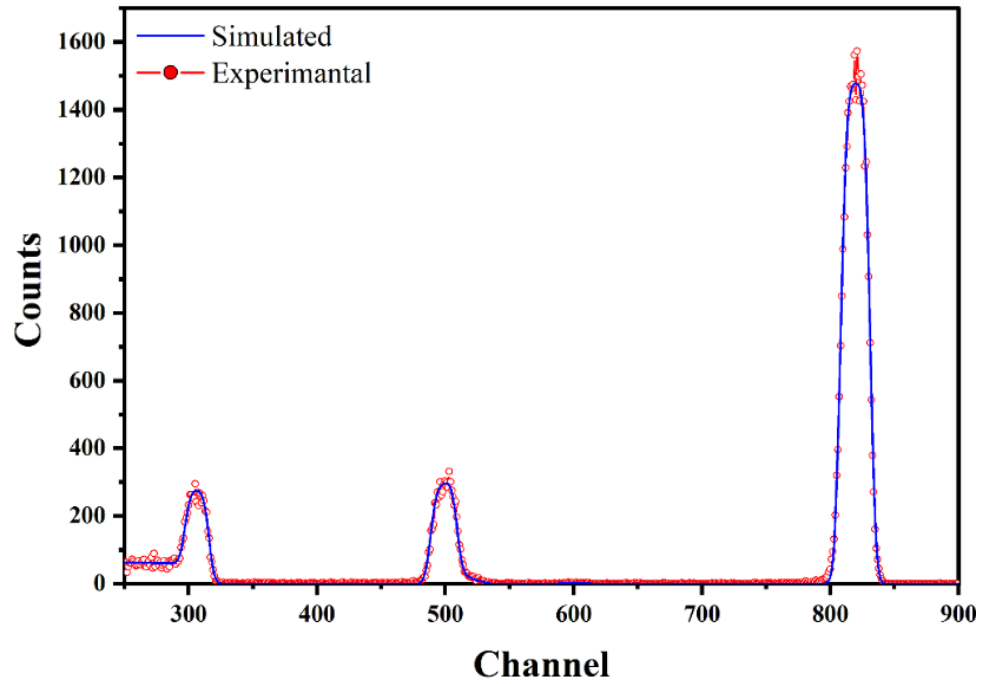


Figure 22. RBS spectrum of $60\text{-Eu}_{6.4}\text{Si}_{25.7}\text{O}_{67.9}$ where the blue line is the simulated data, and the red dots are the experimental data.

The Eu concentration of the thin films deposited using 40 sccm sputtering Ar (total number of 7 samples) and its correlation with sputtering power is investigated and is shown in Figure 23. At a constant Ar flow rate of 40 sccm, regardless of their SiH_4 flow rate, with an increase in the sputtering power the Eu doping level increases. Looking more closely, using the same sputtering power of 20 and 40 W, the Eu content varies as the SiH_4 flow

differs ranging between 1.5 and 2.5 sccm. The effect of different SiH₄ flow rates will be discussed later in this section.

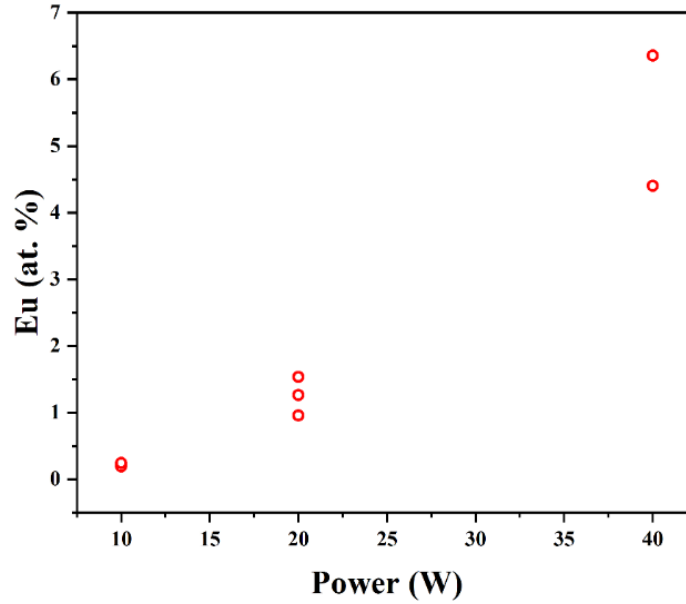


Figure 23. Eu at. % of the Eu-ORSO samples as a function of the sputtering power deposited using a constant Ar flow of 40 sccm. Higher sputtering power results in higher concentration of Eu at. %.

Since the variable deposition parameters are sputtering power, sputtering Ar flow rate and SiH₄ flow rate, the fabricated samples are generally divided into three categories including 1) Constant sputtering power and sputtering Ar flow rate to study the effect of SiH₄ flow rate; 2) Constant SiH₄ flow rate and sputtering Ar flow rate to investigate the effect of the sputtering power; 3) Constant sputtering power and SiH₄ flow rate to examine the influence of sputtering Ar flow rate.

To study the SiH₄ role on Eu doping level, 52-Eu_{1.0}Si_{35.0}O_{64.0}, 57-Eu_{1.5}Si_{32.8}O_{65.6}, and 58-Eu_{2.1}Si_{34.4}O_{63.5} are chosen which all were fabricated using 20 W sputtering power (shown in Figure 23) and 40 sccm sputtering Ar flow rate while SiH₄ flow rate was set at 2.5, 2

and 1.5 sccm, respectively. Figure 24 (a) shows a lower SiH_4 flow results in a higher Eu at. %. This is also consistent with the samples 53- $\text{Eu}_{4.4}\text{Si}_{26.2}\text{O}_{69.4}$ and 60- $\text{Eu}_{6.4}\text{Si}_{25.7}\text{O}_{67.9}$ fabricated with sputtering power of 40 W (shown in Figure 24 (b)).

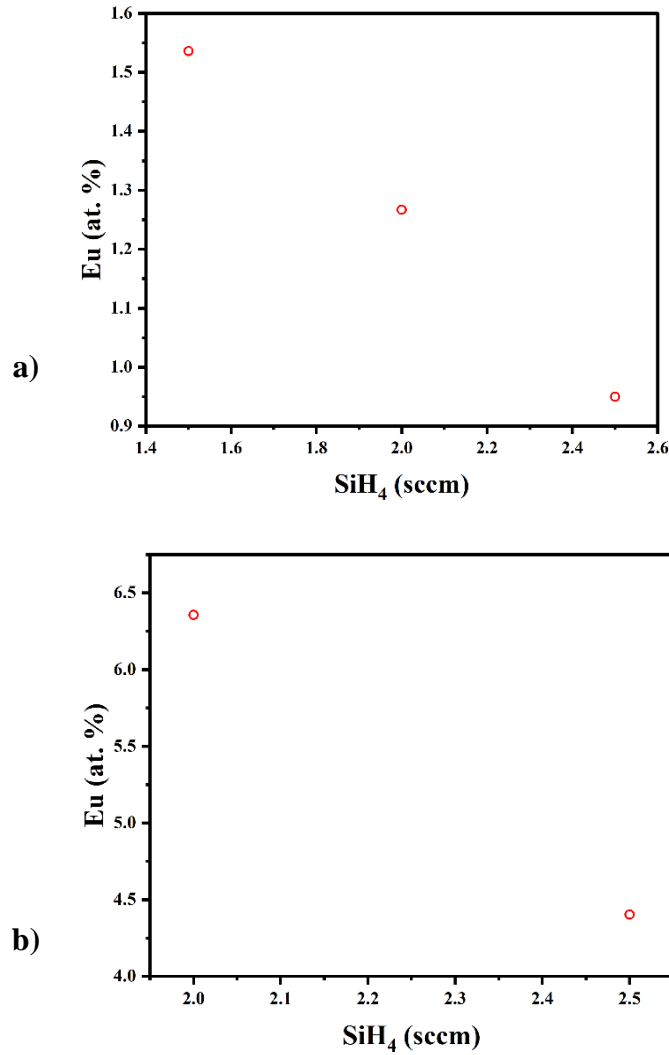


Figure 24. Effect of SiH_4 flow on Eu at. % with a) sputtering power of 20 W and Ar flow rate of 40 sccm; b) sputtering power of 40 W and Ar flow rate of 40 sccm.

Figure 25 shows that the influence of the sputtering power on the concentration of Eu is more significant when SiH_4 flow rate is lower, which can be easily observed in the data

line of SiH_4 flow rate of 1.5 sccm (shown in blue) in comparison with the higher SiH_4 flow rate of 2 sccm (shown in green) where the sputtering power increases from 10 to 20 W. As previously mentioned, this is consistent with the trend of 2 sccm and 2.5 sccm SiH_4 flow rate when the sputtering power changes from 20 to 40 W. This implies that for the thin films grown using a lower SiH_4 flow rate, with increasing sputtering power more Eu concentration can be achieved while this effect is less intense at higher SiH_4 flow rates.

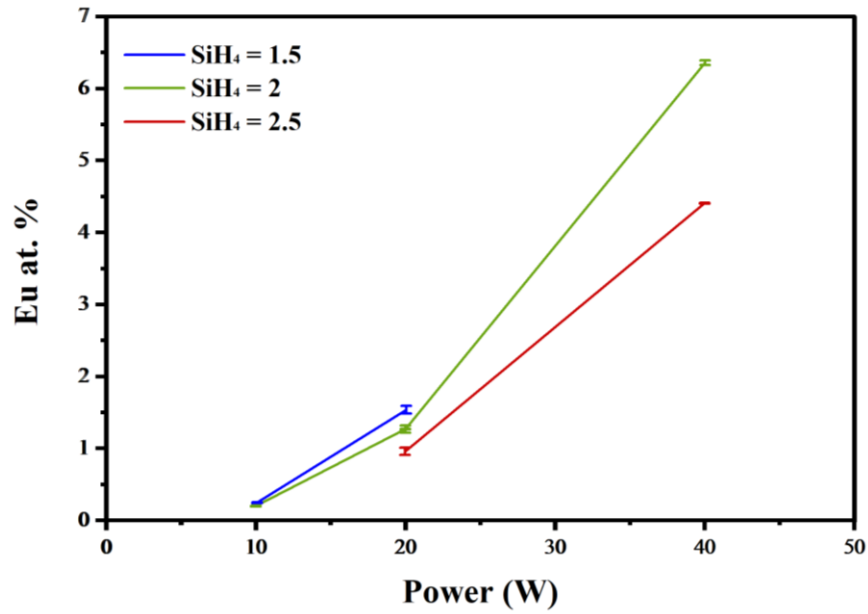


Figure 25. The changes of the Eu at. % with regards to sputtering power for different SiH_4 flow rates.

To compare the elemental composition of the MOP thin films with the IMS ones, the deposition parameters and the thin film composition of MOP samples are provided in Table 4. Among the MOP samples, 37-Eu_{0.0}Si_{31.53}O_{68.27} can be compared to IMS samples 52-Eu_{1.0}Si_{35.0}O_{64.0} and 53-Eu_{4.4}Si_{26.2}O_{69.4} since all were deposited with the same deposition parameters including 60 minutes deposition time, 25 sccm O₂ flow rate, and 2.5 sccm SiH_4 flow rate. The only difference between the MOP and the IMS samples is the approach that

Eu is introduced to the growing layer during the deposition. As previously discussed for the IMS samples, the higher sputtering power leads to a higher Eu percentage in the film. However, the comparison of 37-Eu_{0.0}Si_{31.53}O_{68.27} with 52-Eu_{1.0}Si_{35.0}O_{64.0}, which is grown using lower sputtering power (20 W) compared to 53-Eu_{4.4}Si_{26.2}O_{69.4} (with sputtering power of 40 W), a significant difference in the Eu at. % is observed where 52-Eu_{1.0}Si_{35.0}O_{64.0} contains a higher Eu concentration.

Table 4. Deposition parameters and elemental composition of the as-deposited MOP thin films. For all the thin films the microwave plasma power was set to 500 W while the deposition time, SiH₄ flow rate, and O₂ flow rate varied in the range of 40 to 60 minutes, 1 to 2.5 sccm, and 25 to 30 sccm, respectively.

MOP Samples	30%SiH ₄ /Ar [sccm]	O ₂ /Ar [sccm]/[mTorr]	Eu Cell Temp [°C]	Deposition time [min]	Eu at. %	Si at. %	O at. %
37-Eu _{0,0} Si _{31.53} O _{68.27}	2.5	25	142	60	0	31.5	68.3
38-Eu _{0,1} Si _{35.95} O _{58.61}	2.5	25	170	40	0.1	35.9	58.6
39-Eu _{0,5} Si _{35.77} O _{67.61}	2.5	30	196	60	0.5	35.8	63.6
41-Eu _{0,0} Si _{29.86} O _{69.69}	1	30	170	60	0.1	29.9	69.7
43-Eu _{0,3} Si _{31.25} O _{67.94}	1	30	198	60	0.3	31.2	68

Using the qualitative ERD measurements the approximate H concentration and the influence of each variable in the deposition parameters are studied. Figure 26 shows the ERD spectra of Kapton as a reference sample with known elemental composition, along with the samples 53-Eu_{4.4}Si_{26.2}O_{69.4}, 54-Eu_{0.2}Si_{31.9}O_{67.9}, 55-Eu_{0.8}Si_{31.4}O_{67.8}, 59-Eu_{0.3}Si_{34.3}O_{65.4}, and 60-Eu_{6.4}Si_{25.7}O_{67.9} as representatives for investigating the role of SiH₄ flow rate, sputtering power, and sputtering Ar flow rate. Looking at the ERD spectra of Kapton which contains 25.6 at. % of H, it can be estimated that the H content of all the thin films is around 5-10 at. % (shown in Figure 26).

To indicate the role of SiH₄ flow rate on H concentration two sets of samples, all fabricated using sputtering Ar flow rate of 40 sccm while one was grown with sputtering power of 40 W (53-Eu_{4.4}Si_{26.2}O_{69.4} and 60-Eu_{6.4}Si_{25.7}O_{67.9}) and the other one with sputtering power of 10 W (54-Eu_{0.2}Si_{31.9}O_{67.9} and 59-Eu_{0.3}Si_{34.3}O_{65.4}) were studied. 53-Eu_{4.4}Si_{26.2}O_{69.4} and 60-Eu_{6.4}Si_{25.7}O_{67.9} were grown using SiH₄ flow rate of 2.5 sccm and 2 sccm, respectively. The ERD spectra in Figure 26 shows that in terms of intensity, the H concentration is almost the same 53-Eu_{4.4}Si_{26.2}O_{69.4} and 60-Eu_{6.4}Si_{25.7}O_{67.9} (shown in Figure 27 (a)) while the integrated area of 53-Eu_{4.4}Si_{26.2}O_{69.4} is higher than 60-Eu_{6.4}Si_{25.7}O_{67.9} (shown in Figure 27 (b)).

The second set involves 54-Eu_{0.2}Si_{31.9}O_{67.9} and 59-Eu_{0.3}Si_{34.3}O_{65.4}, which were fabricated using SiH₄ flow rate of 2 sccm and 1.5 sccm, respectively. It is observed that both integrated area and the intensity of 54-Eu_{0.2}Si_{31.9}O_{67.9} are higher compared to 59-Eu_{0.3}Si_{34.3}O_{65.4}. Therefore, as expected, a higher SiH₄ flow rate incorporates a higher H concentration.

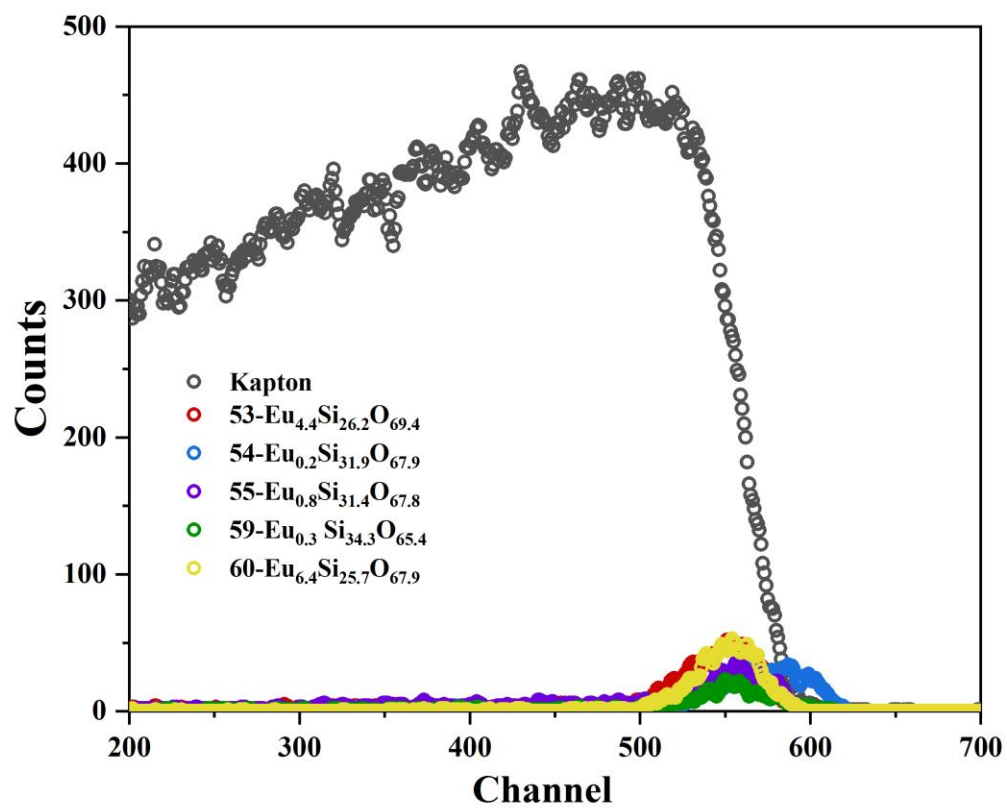


Figure 26. ERD spectra of Kapton and samples 53-Eu_{4.4}Si_{26.2}O_{69.4}, 54-Eu_{0.2}Si_{31.9}O_{67.9}, 55-Eu_{0.8}Si_{31.4}O_{67.8}, 59-Eu_{0.3}Si_{34.3}O_{65.4}, and 60-Eu_{6.4}Si_{25.7}O_{67.9}. The qualitative change of H is observed for different samples

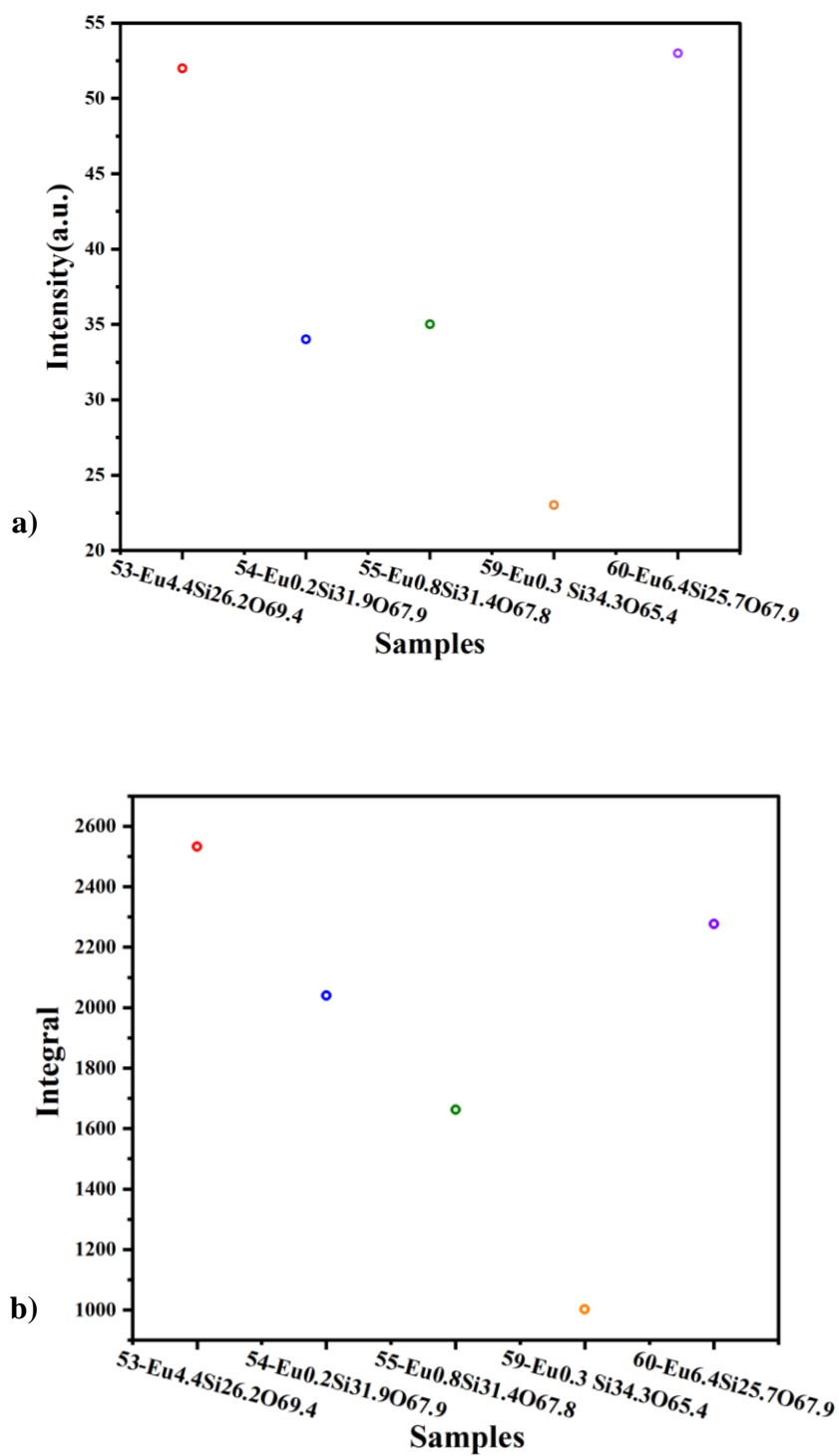


Figure 27. a) Intensity of ERD spectra; and b) Integrated area of ERD spectra of each sample.

The role of the sputtering Ar flow rate on the H content was investigated by studying 54-Eu_{0.2}Si_{31.9}O_{67.9} and 55-Eu_{0.8}Si_{31.4}O_{67.8} both fabricated using SiH₄ flow rate of 2 sccm and sputtering power of 10 W. The Ar flow rate was 40 sccm for 54-Eu_{0.2}Si_{31.9}O_{67.9}, and 10 sccm for 55-Eu_{0.8}Si_{31.4}O_{67.8}. 54-Eu_{0.2}Si_{31.9}O_{67.9} and 55-Eu_{0.8}Si_{31.4}O_{67.8} show almost the same intensity, with 55-Eu_{0.8}Si_{31.4}O_{67.8} being slightly more intense. However, the integrated area of 54-Eu_{0.2}Si_{31.9}O_{67.9} is more than 55-Eu_{0.8}Si_{31.4}O_{67.8}.

Regarding the effect of the sputtering power on the H concentration, 54-Eu_{0.2}Si_{31.9}O_{67.9} and 60-Eu_{6.4}Si_{25.7}O_{67.9} with deposition parameters of 2 sccm SiH₄ flow rate and 40 sccm sputtering Ar flow rate were compared. The sputtering power used to fabricate 54-Eu_{0.2}Si_{31.9}O_{67.9} and 60-Eu_{6.4}Si_{25.7}O_{67.9} was 10 W and 40 W, respectively. The result shows a higher sputtering power is associated with a higher H concentration.

4.2. Variable Angle Spectroscopic Ellipsometry

The refractive indices and thickness of the thin films are determined by performing VASE measurements. Table 5 shows the refractive index and thickness of each thin film. The Complete EASE package software was used for the simulation of VASE measurements where the Cauchy model was applied to perform the simulation of the experimental data. More details of the simulation and setup were explained in Chapter 2. The refractive indices range from 1.5 to 1.6 which is close to that of glass (SiO₂) being 1.4. The thickness of the samples varies between 62.2 to 110.5 nm.

Table 5. Refractive indices, and thickness of the as-deposited IMS thin films.

IMS samples	Refractive index	Thickness (nm)	Thickness Error (nm)
52-Eu_{1.0}Si_{35.0}O_{64.0}	1.48	110.5	0.06
53-Eu_{4.4}Si_{26.2}O_{69.4}	1.54	97.0	0.2
54-Eu_{0.2}Si_{31.9}O_{67.9}	1.47	84.0	0.08
55-Eu_{0.8}Si_{31.4}O_{67.8}	1.47	83.2	0.07
56-Eu_{0.2}Si_{34.2}O_{65.6}	1.47	63.3	0.07
57-Eu_{1.5}Si_{32.8}O_{65.6}	1.49	95.8	0.07
58-Eu_{2.1}Si_{34.4}O_{63.5}	1.50	62.2	0.03
59-Eu_{0.3}Si_{34.3}O_{65.4}	1.47	62.5	0.08
60-Eu_{6.4}Si_{25.7}O_{67.9}	1.58	71.1	0.02

As expected, Figure 28 shows the refractive index decreases with increasing SiH₄ flow rate. Interestingly, at higher sputtering power, for instance, 40 W, the role of SiH₄ flow is more significant compared to the lower sputtering powers of 20 and 10 W. The reason for the observed trend can be explained in terms of the fact that with more incorporation of H, as the consequence of higher SiH₄ flow rate, the density of the thin films decreases and subsequently the refractive index decreases. Whereas with increasing the sputtering power, and as a result of a higher Eu content, both the density and the refractive index of the samples increase.

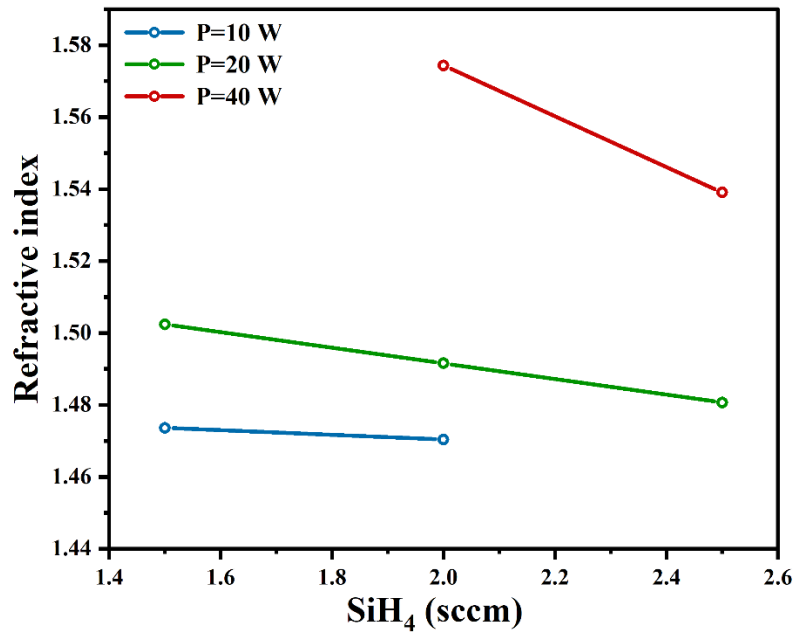


Figure 28. The influence of SiH₄ flow rate on the refractive index at different sputtering powers (P) of 10 to 40 W.

Figure 29 shows the effect of SiH₄ flow rate on the thickness of the thin films grown using 40 sccm Ar flow rate. The trend exhibits a direct relationship between thickness and SiH₄ flow rate. Additionally, regardless of the sputtering power, either it is 10, 20 or 40 W, the effect of SiH₄ on thickness seems to be of equal rate since the three lines presenting different sputtering powers have virtually identical slope. In this matter, it should be considered that the data line for the sputtering power of 20 W is fitted for the three data point (shown in Figure 29).

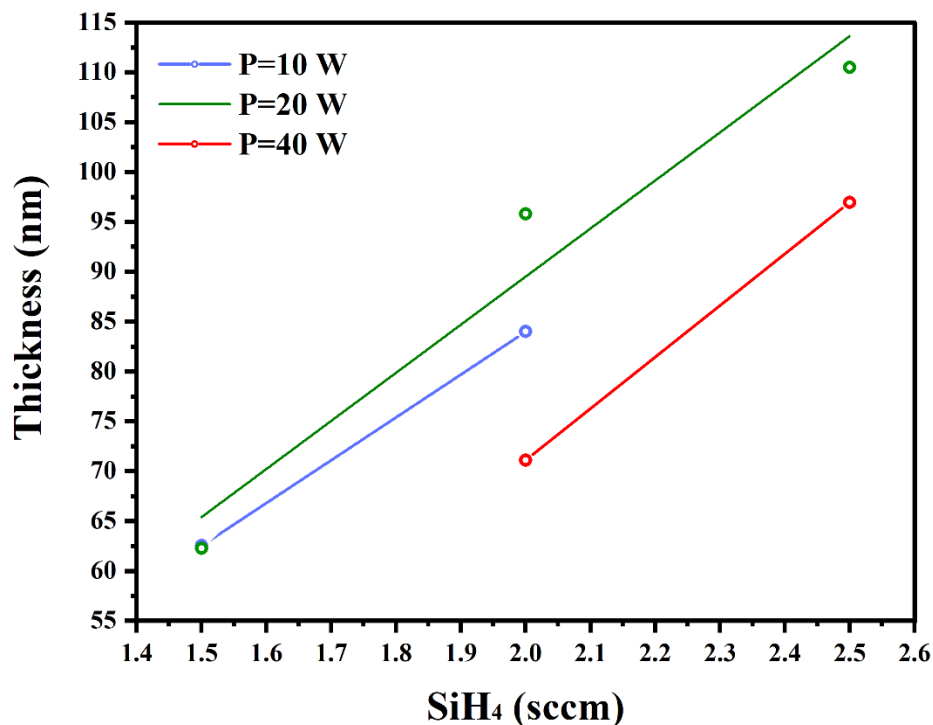


Figure 29. SiH₄ influence on the thickness at different sputtering powers (P) of 10, 20 and 40 W. An equal growth rate of thickness as a result of SiH₄ increase for all sputtering powers is observed.

4.3. Photoluminescence

The light emission of the thin films is detected by PL measurements where a monochromatic He-Cd laser with wavelength of 325 nm is used as the excitation source. The photon with an energy higher than the bandgap of the thin film is radiated towards the samples. When the photon is absorbed, the electrons in the ground state become excited and transmit to the higher energy level and can turn back to their initial state by radiative or non-radiative recombination. In this section the PL properties of the annealed and as-deposited IMS thin films is discussed in details and a brief comparison with the MOP samples is provided. It should be mentioned that as the measurements provide a PL

intensity, which is an arbitrary unit (a. u.), as a function of wavelength. Prior to the PL measurements of the samples, the dark spectrum at room temperature is collected and is subtracted from the PL spectrum of the studied samples.

All the IMS thin films were subjected to the post deposition annealing for 60 minutes in a wide range of temperatures ranging from 300°C to 1350°C and two annealing atmospheres of pure N₂ and 95% of N₂ and 5% of H₂ (N₂+ H₂). As the PL measurements of all the thin films annealed at temperatures of 300°C to 1200°C using annealing atmosphere of pure N₂ were collected a significant PL intensity increase for all thin films annealed at 1200°C compared to the ones annealed at lower temperatures (300 to 1000°C) was observed.

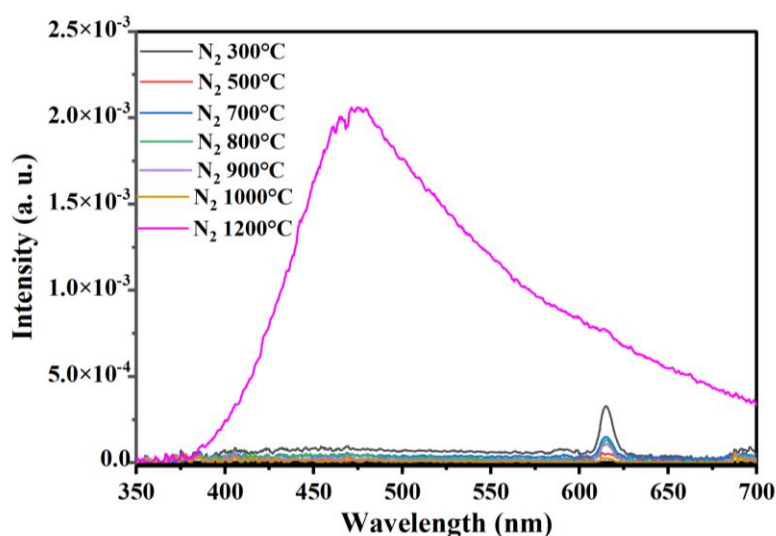


Figure 30. PL measurements of 57-Eu_{1.5}Si_{32.8}O_{65.6} annealed at temperatures of 300 to 1200°C using N₂ atmosphere for 60 minutes as the representative of low temperature PL measurements.

Figure 30 shows a representative of the PL measurements for the samples annealed at temperatures between 300 to 1200°C using N₂ atmosphere for 60 minutes. The peak at 615 nm which is more pronounced for the lower temperatures from 300 to 1000°C is

corresponding to the Eu^{3+} transition. On the other hand, for the sample annealed at 1200°C , the PL intensity significantly increases showing a combination of Eu^{2+} (blue light) and Eu^{3+} (red light) related transitions. The fluctuating trend of PL intensity for the samples annealed at different temperatures ranging between 300 to 1000°C can be ascribed to reduction of optically active site containing Eu or some defects introduced which can lead to quenching of luminescence centers and the abrupt increase at 1200°C can be associated with the formation of $\text{Eu}_x\text{Si}_y\text{O}_z$ nanocrystals. Similar fluctuating trend was previously observed for Ce doped ORSO thin films reported by J.Li et. al [56]. However, the origin of this luminescence behaviour is still unknown in the community, and it requires further studies to understand the reason why at some annealing temperatures the PL intensity decreases. It is remarkable that even at temperatures as low as 300°C the red light emission is achieved which is in one of the ranges that benefits photosynthesis process. On the other hand, the PL measurements of the MOP samples, 37- $\text{Eu}_{0.0}\text{Si}_{31.53}\text{O}_{68.27}$ and 38- $\text{Eu}_{0.1}\text{Si}_{35.95}\text{O}_{58.61}$, fabricated using analogous deposition parameters to that of IMS samples, show weak and noise like emission at 615 nm which is corresponding to the transition of $^5\text{D}_0$ to $^7\text{F}_2$ in Eu^{+3} energy level [39] (shown in Figure 31). This confirms the advantage of the use of the sputtering method integrated with the ECR-PECVD.

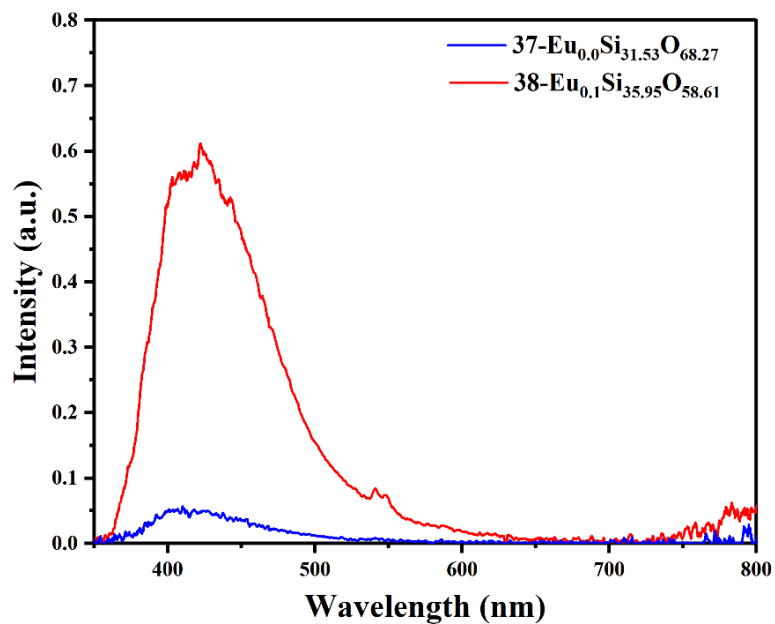


Figure 31. PL measurements of 37-Eu_{0.0}Si_{31.53}O_{68.27} and 38-Eu_{0.1}Si_{35.95}O_{58.61} annealed at 1200°C and N₂ atmosphere for 60 minutes.

To study changes introduced by H passivation, samples annealed at 1200 and 1350°C using annealing atmospheres of N₂ and N₂ +H₂ are compared. It is observed that H passivation enhances the PL emission by one order of magnitude possibly due to the passivation of the defects and dangling bonds. Figure 32 represents the PL measurements of 52-Eu_{1.0}Si_{35.0}O_{64.0} annealed at 1200 and 1350°C and two annealing atmospheres of N₂ and N₂+H₂.

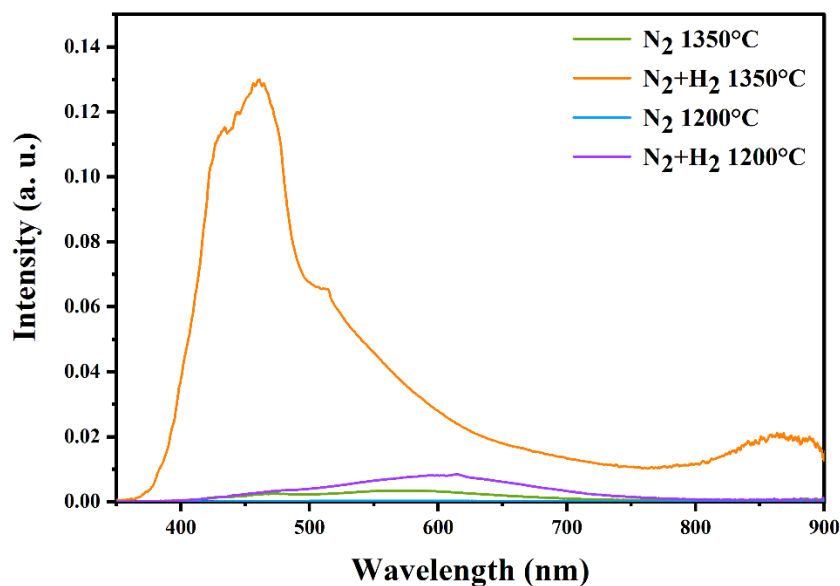


Figure 32. PL spectra of 52-Eu_{1.0}Si_{35.0}O_{64.0} at 1200°C and 1350°C in N₂ and N₂+H₂ atmospheres.

The PL measurements of all IMS thin films annealed at 1350°C and N₂+H₂ atmosphere are shown in Figure 33. In the annealing atmosphere of N₂+H₂ with the increase of the annealing temperature to 1350°C, a combination of Eu²⁺ and Eu³⁺ related emission is observed while the peak at 615 nm corresponding to Eu³⁺ is not dominate. Instead, there are mainly two PL emission peaks centering at wavelengths of 430 and 460 nm which are associated with the Eu²⁺ emission but with a variation of PL intensity where 60-Eu_{6.4}Si_{25.7}O_{67.9} with Eu at. % of 6.4 ± 0.3 is attributed to the highest PL intensity. The Commission Internationale de l'Éclairage (CIE) chromaticity diagram of all the samples annealed at 1350°C and N₂+H₂ atmosphere is shown in Figure 34. Details on the x and y positions of the CIE color coordinates are provided in Table 6 and as observed, the emissions are positioned close to the values of blue light.

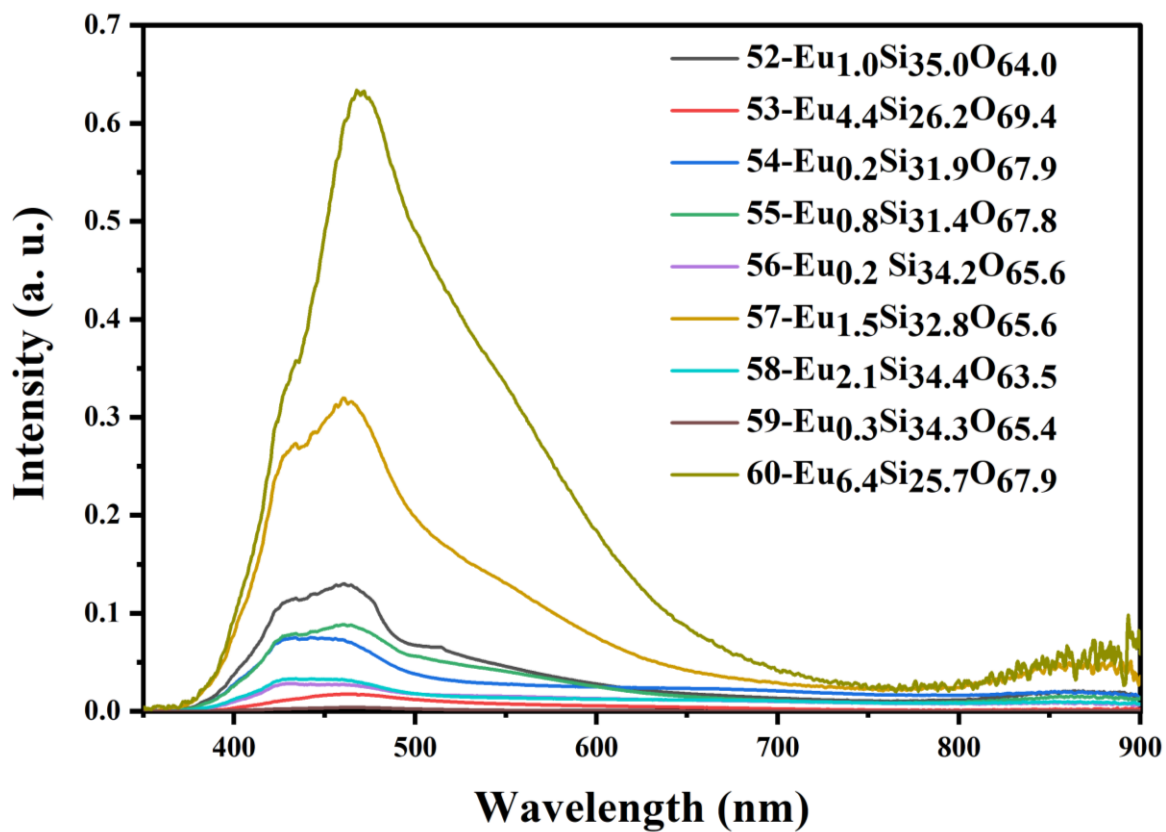


Figure 33. PL spectra of all IMS thin films annealed at 1350°C and N₂+H₂ atmosphere. Two main peaks are observed at 430 nm and 460 nm where the highest peak achieved is related to 60-Eu_{6.4}Si_{25.7}O_{67.9}.

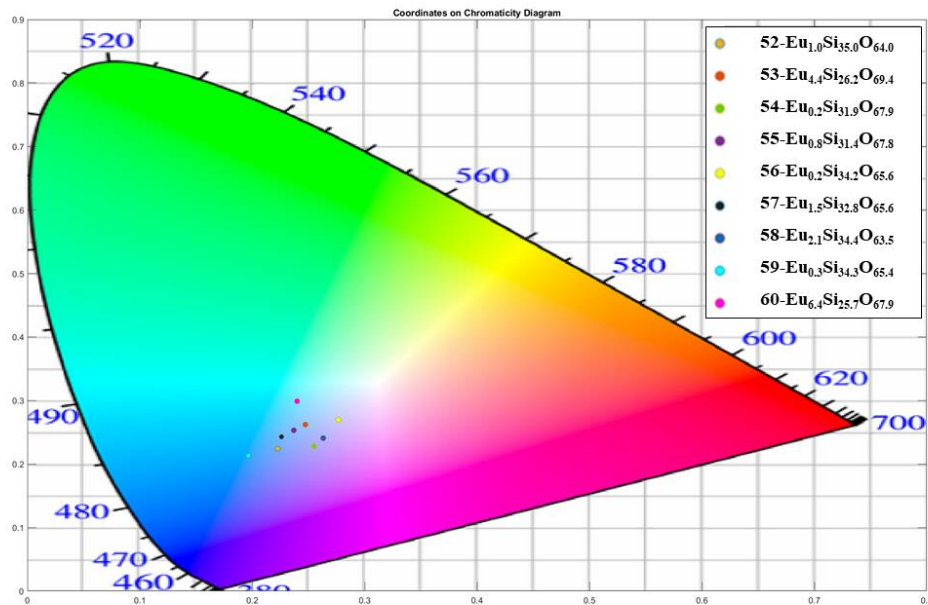


Figure 34. CIE chromaticity diagram of all the IMS samples at annealing condition of 1350°C and N₂+H₂ atmosphere.

Table 6. CIE coordination of all the IMS samples annealed at 1350°C and N₂+H₂ atmosphere.

IMS samples	CIE _x	CIE _y
52-Eu _{1.0} Si _{35.0} O _{64.0}	0.2225	0.2242
53-Eu _{4.4} Si _{26.2} O _{69.4}	0.2472	0.2621
54-Eu _{0.2} Si _{31.9} O _{67.9}	0.2549	0.2281
55-Eu _{0.8} Si _{31.4} O _{67.8}	0.2369	0.2532
56-Eu _{0.2} Si _{34.2} O _{65.6}	0.2765	0.2697
57-Eu _{1.5} Si _{32.8} O _{65.6}	0.226	0.2429
58-Eu _{2.1} Si _{34.4} O _{63.5}	0.2631	0.2408
59-Eu _{0.3} Si _{34.3} O _{65.4}	0.1966	0.2132
60-Eu _{6.4} Si _{25.7} O _{67.9}	0.2399	0.299

4.3.1. Influence of Deposition Parameters on Photoluminescence

The effect of each deposition parameter, SiH₄ flow rate, sputtering Ar flow rate and sputtering power, was investigated on the IMS samples where all the deposition parameters except one are identical in each set. A representative of each sample set annealed at 1350°C and N₂+H₂ atmosphere is discussed in this section and the main points are mentioned. The effect of SiH₄ flow rate on the PL was investigated by studying the PL measurements of 52-Eu_{1.0}Si_{35.0}O_{64.0}, 57-Eu_{1.5}Si_{32.8}O_{65.6} and 58-Eu_{2.1}Si_{34.4}O_{63.5} all deposited using 40 sccm sputtering Ar flow rate and sputtering power of 20 W while the SiH₄ flow rate is 2.5, 2 and 1.5 sccm, respectively (shown in Figure 35). The first and the second peaks positioned at 430 and 460 nm both correspond to Eu²⁺ transition which is related to the blue emission. The peak at 585 nm corresponding to Eu³⁺ emission (⁵D₀ to ⁷F₁ energy level) is slightly hidden by the intense peaks at 460 and 430 nm. The ratio of Eu³⁺ to Eu²⁺ emission increases at lower SiH₄ flow rate.

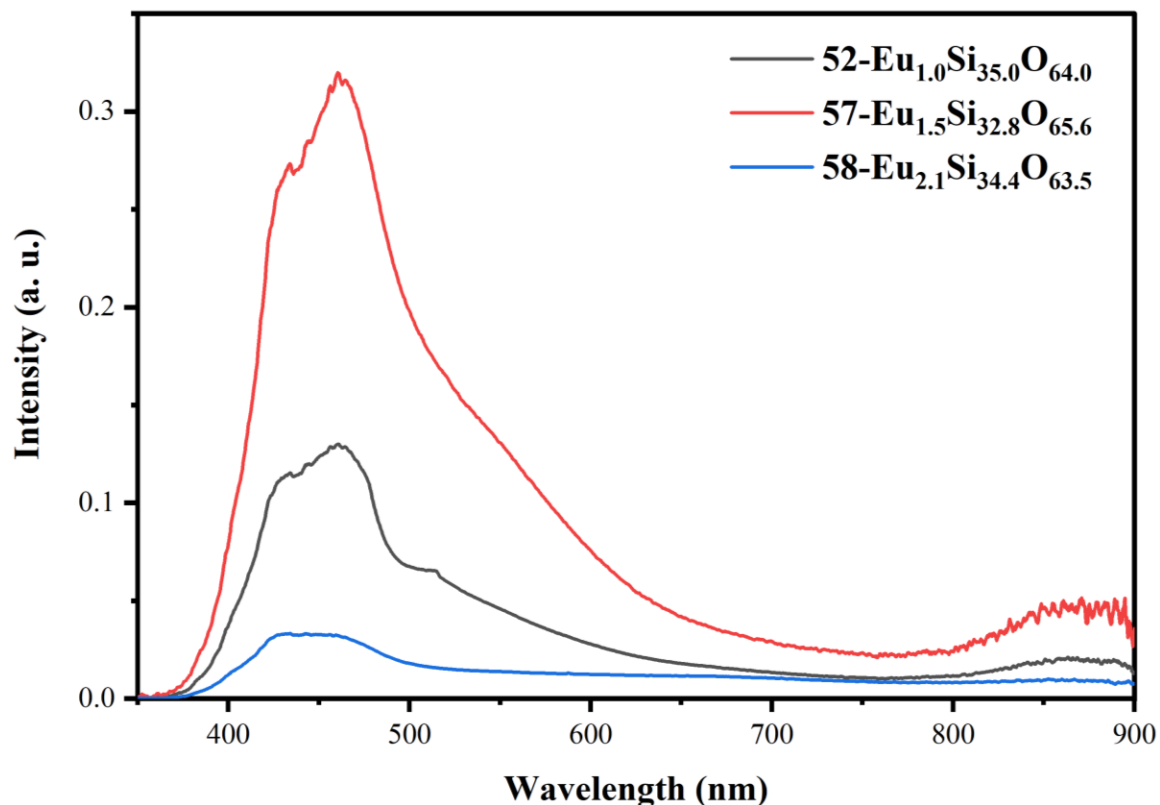


Figure 35. PL spectra of 52-Eu_{1.0}Si_{35.0}O_{64.0}, 57-Eu_{1.5}Si_{32.8}O_{65.6} and 58-Eu_{2.1}Si_{34.4}O_{63.5} annealed at 1350°C and N₂+H₂ atmosphere. The sputtering Ar flow rate and sputtering power were set constant at 40 sccm and 20 W for all samples while the SiH₄ flow rate was 2.5, 2 and 1.5 sccm for 52-Eu_{1.0}Si_{35.0}O_{64.0}, 57-Eu_{1.5}Si_{32.8}O_{65.6} and 58-Eu_{2.1}Si_{34.4}O_{63.5}, respectively.

The role of sputtering power was investigated by studying the PL measurements of 54-Eu_{0.2}Si_{31.9}O_{67.9}, 57-Eu_{1.5}Si_{32.8}O_{65.6} and 60-Eu_{6.4}Si_{25.7}O_{67.9} produced using similar deposition parameters of 2 sccm SiH₄ flow rate and 40 sccm sputtering Ar flow rate while the sputtering power was 10, 20 and 40 W, respectively (shown in Figure 36). The ratio of Eu³⁺ to Eu²⁺ emission (580 nm to 430 nm) is higher at higher sputtering power which implies 60-Eu_{6.4}Si_{25.7}O_{67.9} generates the highest Eu³⁺ to Eu²⁺ ratio.

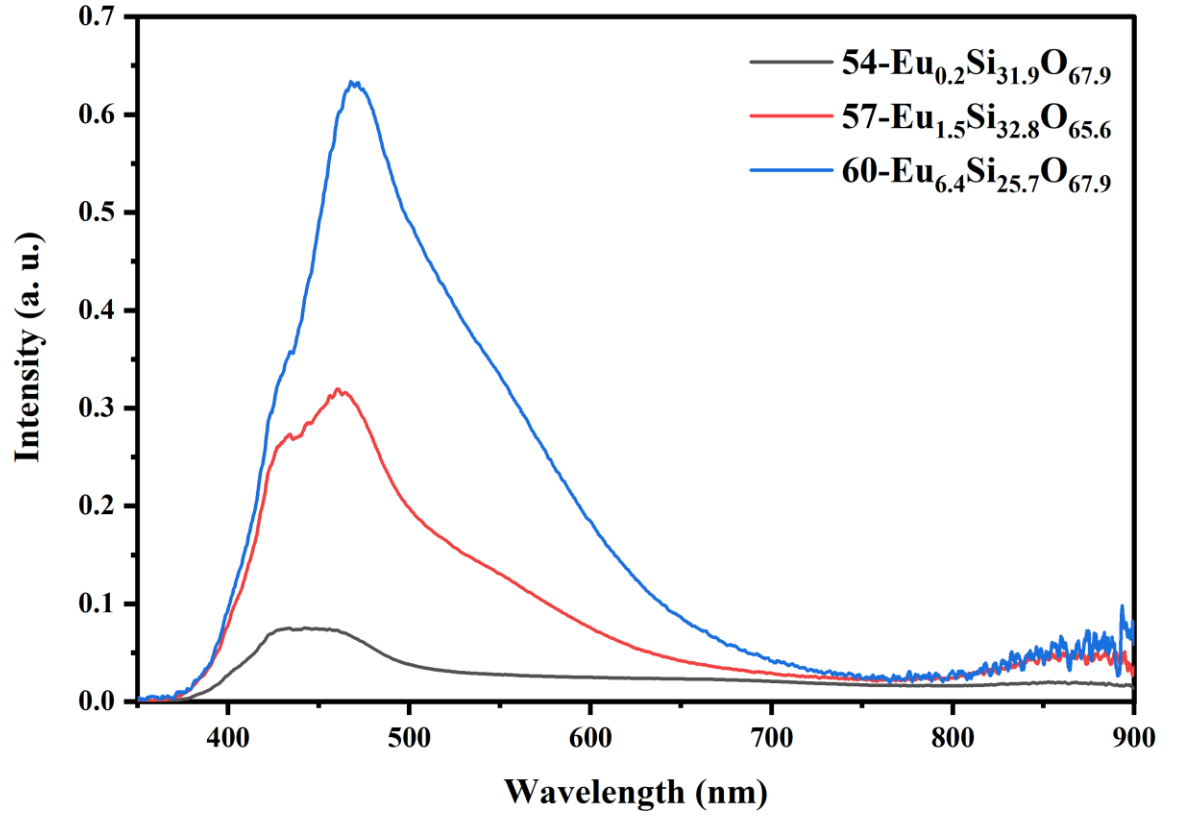


Figure 36. PL spectra of 54-Eu_{0.2}Si_{31.9}O_{67.9}, 57-Eu_{1.5}Si_{32.8}O_{65.6} and 60-Eu_{6.4}Si_{25.7}O_{67.9} at annealing condition of 1350°C and N₂+H₂ atmosphere. The sputtering Ar flow rate and SiH₄ flow rate were kept constant at 40 sccm and 2 sccm, respectively, for all samples while the sputtering power was 10 W for 54-Eu_{0.2}Si_{31.9}O_{67.9}, 20 W for 57-Eu_{1.5}Si_{32.8}O_{65.6}, and 40 W for 60-Eu_{6.4}Si_{25.7}O_{67.9}.

To investigate the role of the sputtering Ar flow rate on the PL intensity of IMS samples, PL measurements of 56-Eu_{0.2}Si_{34.2}O_{65.6} and 59-Eu_{0.3}Si_{34.3}O_{65.4} fabricated using sputtering power of 10 W and SiH₄ flow rate of 1.5 sccm is shown in Figure 37. The sputtering Ar flow rate was 10 and 40 sccm for 56-Eu_{0.2}Si_{34.2}O_{65.6} and 59-Eu_{0.3}Si_{34.3}O_{65.4}, respectively. It

is observed that a higher Eu^{3+} to Eu^{2+} ratio is attributed to a lower sputtering Ar flow rate which in this case is 56- $\text{Eu}_{0.2}\text{Si}_{34.2}\text{O}_{65.6}$.

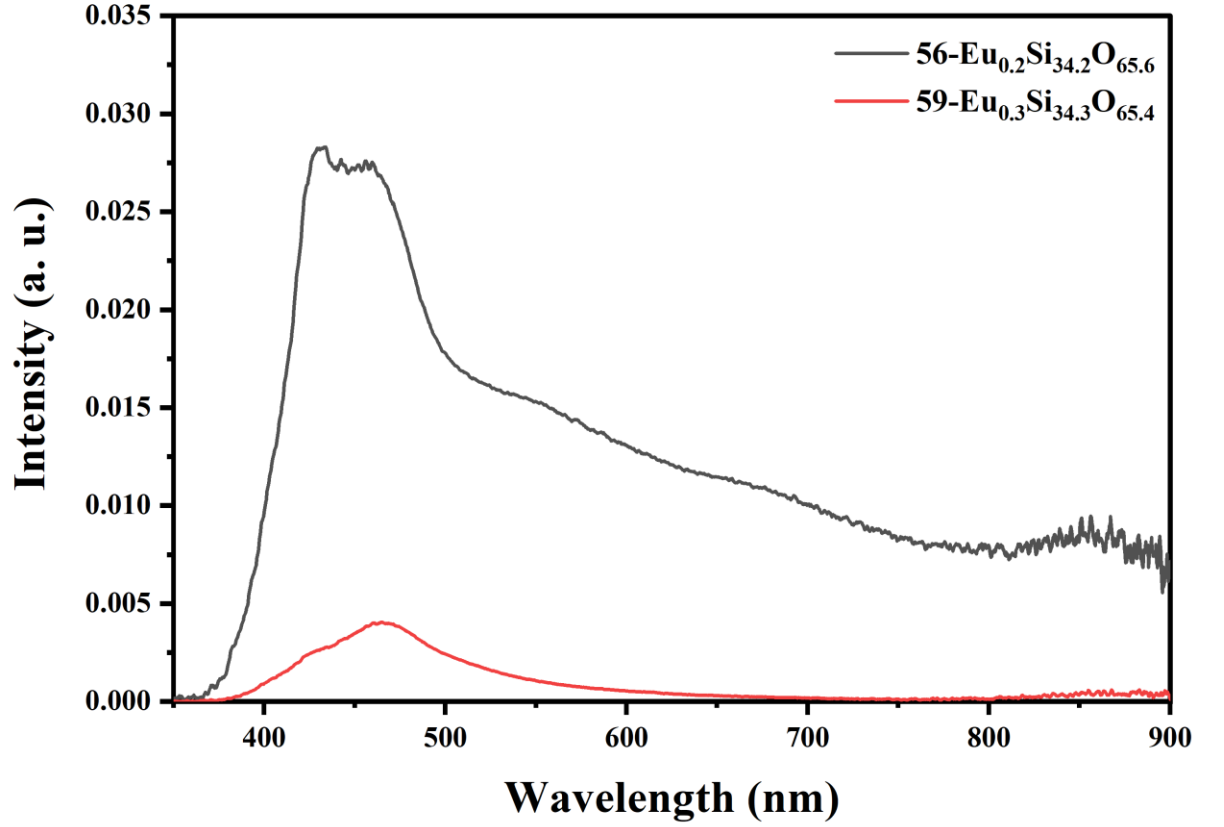


Figure 37. PL spectra of 56- $\text{Eu}_{0.2}\text{Si}_{34.2}\text{O}_{65.6}$ and 59- $\text{Eu}_{0.3}\text{Si}_{34.3}\text{O}_{65.4}$ at annealing conditions of 1350°C and N_2+H_2 atmosphere. The sputtering power and SiH_4 flow rate were set at 10 W and 1.5 sccm for both samples while the Ar flow rate was 10 sccm for 56- $\text{Eu}_{0.2}\text{Si}_{34.2}\text{O}_{65.6}$ and 40 sccm for 59- $\text{Eu}_{0.3}\text{Si}_{34.3}\text{O}_{65.4}$.

Chapter 5: Structural Analysis

In this chapter, the structural properties of the IMS samples are discussed based on the XRD measurements; and the crystalline phases in the samples are identified. In addition, TEM analysis is performed and discussed as a complementary measurement to confirm the formation of crystalline structures in the thin films annealed at high temperatures. The as-deposited Eu-doped ORSO thin films are originally an amorphous structure. Post deposition annealing process at temperatures ranging from 300 to 1350°C promotes the formation of crystalline nanostructures within the films (shown in Figure 38).

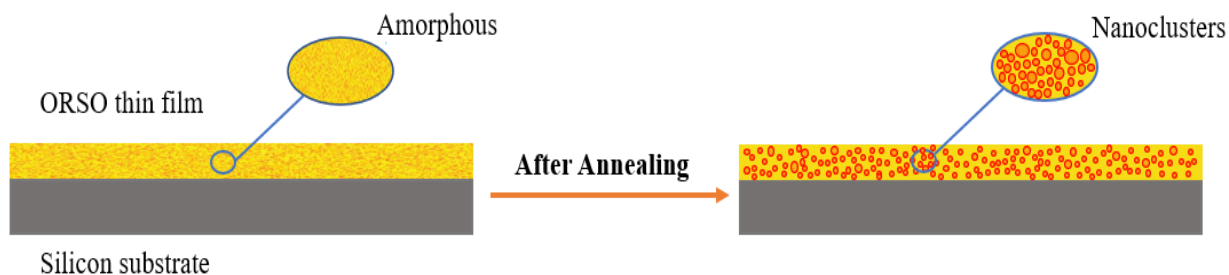


Figure 38. Formation of Si-ncs within the thin films when subjected to post-deposition annealing. The phase separation in the ORSO matrix occurs when the amorphous structure of the thin film changes as the result of thermal annealing.

5.1. X-ray Diffraction

At lower annealing temperatures (approximately below 800-900°C) it was observed that the structure remains amorphous (shown in Figure 39 (a)) since the formation of crystalline structure requires a higher annealing temperature. However, at temperatures above 900°C crystalline structures appear to form (shown in Figure 39 (b)), and with increasing the

temperature, different $\text{Eu}_x\text{Si}_y\text{O}_z$ crystalline structures are detected (shown in Figure 39 (c) and (d)).

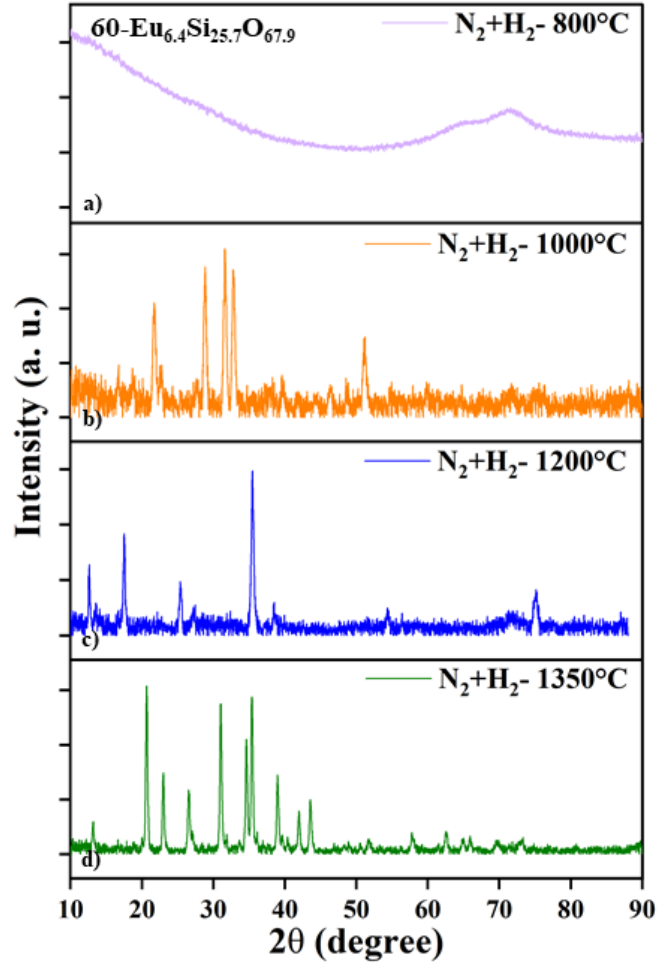


Figure 39. XRD pattern of $60\text{-Eu}_{6.4}\text{Si}_{25.7}\text{O}_{67.9}$ annealed using N_2+H_2 atmosphere and at a) 800°C temperature exhibits amorphous structure; b) 1000°C shows some crystalline structure; c) Annealed at 1200°C , and d) 1350°C temperature show distinctive $\text{Eu}_x\text{Si}_y\text{O}_z$ crystalline formed.

The phases detected by XRD measurements for $60\text{-Eu}_{6.4}\text{Si}_{25.7}\text{O}_{67.9}\text{-N}_2+\text{H}_2\text{-}1000^\circ\text{C}$ are europium oxide silicate ($\text{Eu}_5(\text{SiO}_4)_3\text{O}$), SiO_2 , and gwihabaite (NH_4NO_3) (shown in Figure

40 (a)) whereas that of $60\text{-Eu}_{6.4}\text{Si}_{25.7}\text{O}_{67.9}\text{-N}_2\text{+H}_2\text{-1200}^\circ\text{C}$ are dieuropium silicate ($\text{Eu}_2(\text{Si}_2\text{O}_7)$) and europium silicate ($\text{Eu}_2\text{Si}_2\text{O}_7/\text{Eu}_2\text{SiO}_5$) (shown in Figure 40 (b)). Figure 40 shows that $60\text{-Eu}_{6.4}\text{Si}_{25.7}\text{O}_{67.9}\text{-N}_2\text{+H}_2\text{-1000}^\circ\text{C}$ and $60\text{-Eu}_{6.4}\text{Si}_{25.7}\text{O}_{67.9}\text{-N}_2\text{+H}_2\text{-1200}^\circ\text{C}$ can be indexed to the aforementioned crystalline phases, however, they are not ideally fitted with the crystalline phases in terms of intensity or covering at all 2θ degrees.

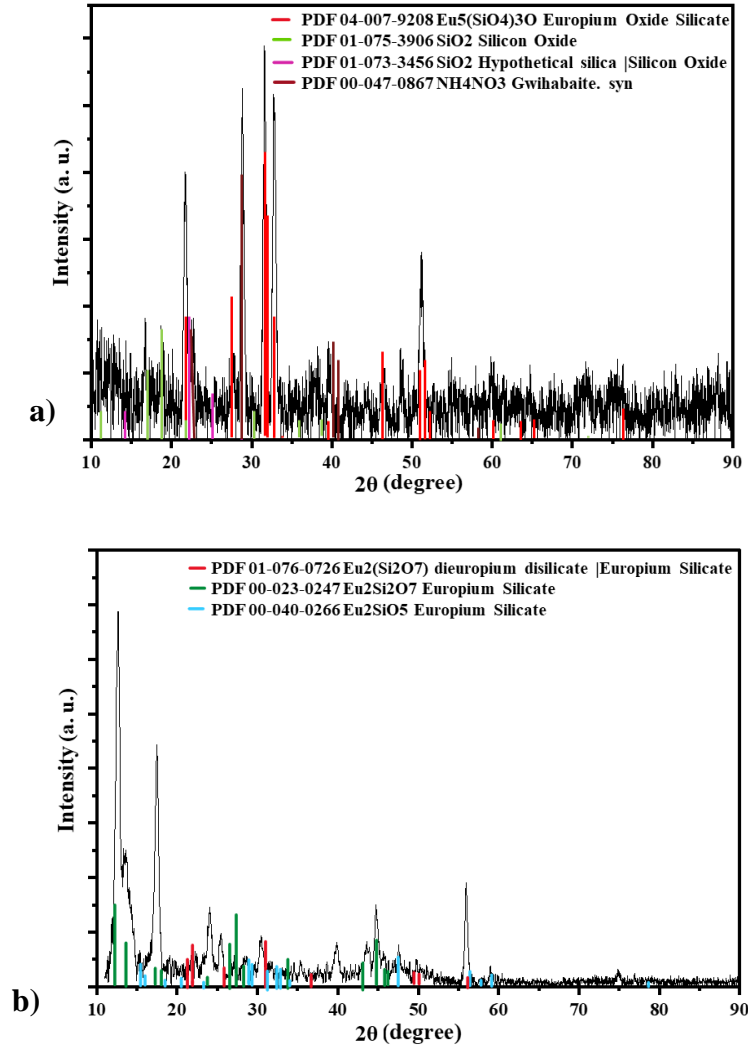


Figure 40. XRD pattern and the phase ID of a) $60\text{-Eu}_{6.4}\text{Si}_{25.7}\text{O}_{67.9}\text{-N}_2\text{+H}_2\text{-1000}^\circ\text{C}$; and b) $60\text{-Eu}_{6.4}\text{Si}_{25.7}\text{O}_{67.9}\text{-N}_2\text{+H}_2\text{-1200}^\circ\text{C}$.

In the case of $60\text{-Eu}_{6.4}\text{Si}_{25.7}\text{O}_{67.9}\text{-N}_2\text{+H}_2\text{-1350}^\circ\text{C}$ the matched phases are europium silicon (Eu_3Si_4), silicon nitride (Si_3N_4), moganite (SiO_2), europium oxide (Eu_2O_3), europium

silicon oxide (Eu_xSiO_2) with the dominant phase being Si_3N_4 (shown in Figure 41). As there has not been any N in the precursor gases during the deposition of the thin films and the absence of N was further approved by performing RBS analysis, the main peaks in 60- $\text{Eu}_{6.4}\text{Si}_{25.7}\text{O}_{67.9}\text{-N}_2\text{+H}_2\text{-1350}^\circ\text{C}$ cannot be related to Si_3N_4 phase and it should be originated from another phase with a similar structure to Si_3N_4 composed of Eu, O and/or Si. Although N_2 was used as an inert gas in the annealing process, N cannot diffuse significantly in the sample and form Si_3N_4 phase. This also applies to the NH_4NO_3 phase which was detected for 60- $\text{Eu}_{6.4}\text{Si}_{25.7}\text{O}_{67.9}\text{-N}_2\text{+H}_2\text{-1000}^\circ\text{C}$.

Figure 41 shows that the reference data of Si_3N_4 with PDF card of 00-041-0360 is well-indexed with the 60- $\text{Eu}_{6.4}\text{Si}_{25.7}\text{O}_{67.9}\text{-N}_2\text{+H}_2\text{-1350}^\circ\text{C}$, however, as explained previously there should be some structure similar to Si_3N_4 formed in the samples annealed using $\text{N}_2\text{+H}_2$ at 1350°C . The rest of the peaks in the XRD pattern of 60- $\text{Eu}_{6.4}\text{Si}_{25.7}\text{O}_{67.9}\text{-N}_2\text{+H}_2\text{-1350}^\circ\text{C}$ can be indexed to Eu_3Si_4 , Si_3N_4 , moganite SiO_2 , Eu_2O_3 , and Eu_xSiO_2 . This indicates there is lower certainty for the presence of these phases as their reference data is not as match as the Si_3N_4 phase with 00-041-0360 PDF card. The reason for the low certainty of most of the phases is that the database is for Powder X-ray Diffraction in which the orientations are fairly random, but the samples in this study are thin films, and in thin films, there is always some level of texture and random orientation [55].

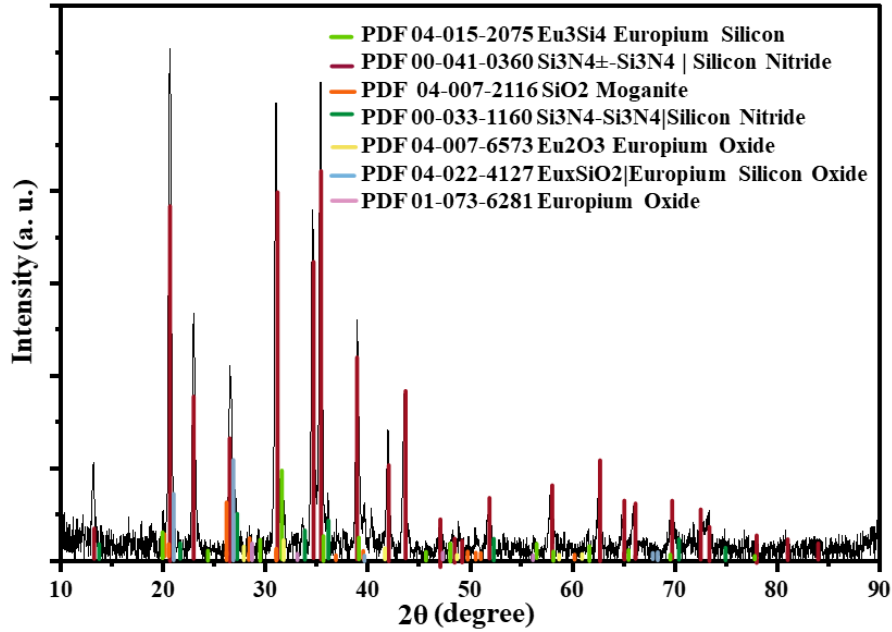


Figure 41. XRD pattern with phase IDs included for the sample 60-Eu_{6.4}Si_{25.7}O_{67.9}-N₂+H₂-1350°C.

The patterns of diffracted X-rays of 60-Eu_{6.4}Si_{25.7}O_{67.9}-N₂+H₂ at annealing temperatures of 800, 1000, 1200, and 1350°C are shown in Figure 42. The broad bright spot which appeared in all 2D patterns at 72 degrees is due to the single-crystal Si substrate (shown with the green circle in Figure 42 (a)). As it can be seen when the sample 60-Eu_{6.4}Si_{25.7}O_{67.9} is annealed using N₂+H₂ atmosphere at 800°C, its 2D pattern shows that there is no diffraction pattern corresponding to the presence of crystalline phases and the structure remains amorphous. The small bright dots (circled with blue in Figure 42 (a)) are textures but since they are negligible, the sample is considered amorphous. The peak at 28.5 degrees is related to the (100) plane of a single crystal of Si substrate and the one at 72 degrees is corresponding to the (400) plane of Si crystal [57][58].

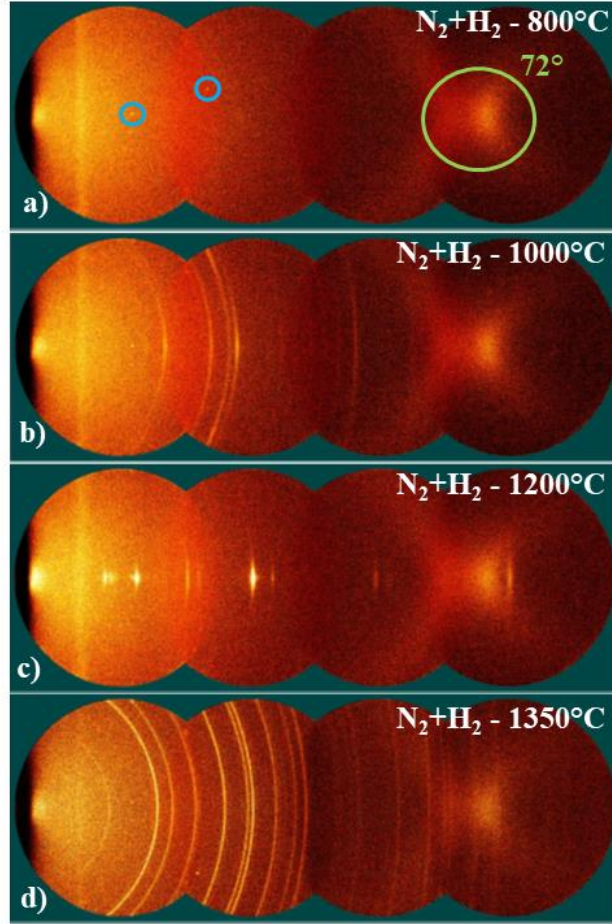


Figure 42. Each image shows a merge of four diffracted frames, at 2θ degrees of 15, 35, 55 and 75, of 60-Eu_{6.4}Si_{25.7}O_{67.9} using an annealing atmosphere of N₂+H₂. Different annealing temperatures are presented in a) 800°C; b) 1000°C; c) 1200°C; and d) 1350°C.

As shown in Figure 42 (b), for the sample 60-Eu_{6.4}Si_{25.7}O_{67.9}-N₂+H₂-1000°C the ring patterns show some of the aforementioned crystalline phases, and as the diffraction rings are not uniformly distributed, it indicates that there is some intensity response variation along with the diffraction rings [58]. This variation in the intensity response of the diffraction rings implies that the brighter spots along the rings correlate with the preferred orientations in the detected phase, and the phase orientation is not completely randomized. Further analysis of this sample is not required since the diffraction lines can be observed.

Therefore, Figure 42 (c) suggests that the diffracted frame of 60-Eu_{6.4}Si_{25.7}O_{67.9}-N₂+H₂-1200°C is highly textured with no random orientation [55]. This can be explained in terms of the transformation of some of the phases which appeared in 60-Eu_{6.4}Si_{25.7}O_{67.9}-N₂+H₂-1000°C occur at 1200°C and the diffraction rings at 1200°C appear as textures rather than uniformly distributed rings. Further analysis of this sample presents more elaborate information on its structural properties which will be discussed qualitatively later. As shown in Figure 42 (d) the diffraction rings for 60-Eu_{6.4}Si_{25.7}O_{67.9}-N₂+H₂-1350°C appeared as sharp and uniformly bright lines implying that all the crystalline phases at each ring are randomly oriented and are evenly distributed with no texture structure.

The original XRD pattern of 60-Eu_{6.4}Si_{25.7}O_{67.9}-N₂+H₂-1200°C was collected at 2θ degrees of 15, 35, 55, and 75 and incident angle of psi=90 degrees. The 2D pattern in Figure 42 (c) shows that the sample is highly textured, and the orientation distribution has deviated compared to its ideal random orientation which is obtained from powder X-ray diffraction. This implies that there is some preferred orientation to the crystalline phases. These diffraction rings with preferred orientation appear as peaks in the XRD pattern while for the highly textured samples some orientation cannot satisfy the Bragg condition, and are not detected in the XRD pattern [58]. Thus, to detect the missing peaks, the XRD pattern was additionally collected at psi=54 degrees. The separate XRD patterns at psi degree of 90 versus 54 are shown in Figure 43. The missing peaks at psi 90 degrees which appeared at psi degree of 54 are at 2θ=30.5, 43.7, and 44.8° (shown in Figure 43). For the phase ID, both scans at 90 and 54 psi degrees were added together (shown in Figure 40 (b)).

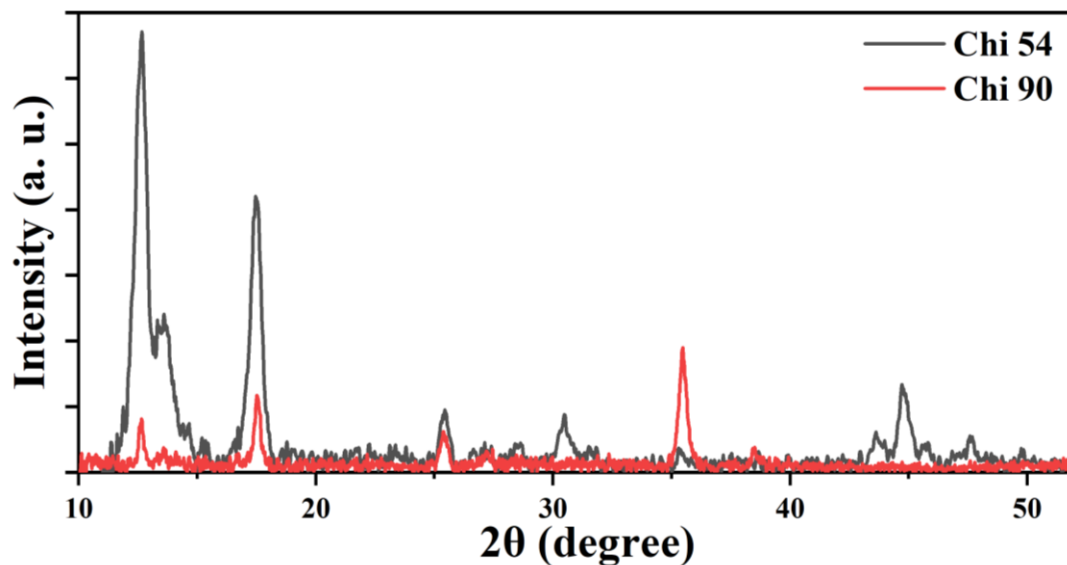


Figure 43. XRD pattern of $60\text{-Eu}_{6.4}\text{Si}_{25.7}\text{O}_{67.9}\text{-N}_2\text{+H}_2\text{-1200}^\circ\text{C}$ detected at psi (chi) degree of 90 shown in red and 54 shown in black.

The XRD frame at 2θ degree of 35° , psi of 54° , and full rotation of 360° phi is shown in Figure 44 where the blue arrow represents the normal to the surface.

Peaks at 2θ values of 12.5° , 17.4° , and 25.2° (first three peaks from the left side shown in Figure 39 (c)) are always present in the azimuthal angle (γ) hence pole figures are not collected for these values. To be more specific when the sample is rotating, these three spots do not disappear from the XRD frame with the change of phi. In Figure 42 (c) the three bright spots in the first frame (2θ degree of 15) represent the 2θ peaks at 12.5° , 17.4° , and 25.2° . On the other hand, the peak at 2θ degree of 44.8 did not appear in this frame which is likely because the scan time was not sufficient to capture that peak. For the rest of the peaks (30° and 43.6°) which could not be detected at a psi degree of 90, the pole figures are generated and shown in Figure 45.

The diffraction ring at 30° that did not diffract at a psi of 90 degrees is shown in Figure 45 (a). As it can be seen there is a fiber structure that does not have a perfect fiber texture since it is patchy, and it is not uniform around the ring meaning that there is a preferred orientation within this texture structure.

There is no fiber texture at 31.7° (Figure 45 (b)) but there are two bright spots in the vicinity of the intense bright spots at every 90° which is due to the single crystal of Si substrate. The two bright spots can be due to the planar twinning defects. In general, twinning occurs when the substance is subjected to high pressure/temperature and as the result, the plane lattice of one crystal shares lattice point with another crystal [59]. Therefore, it can imply that the high annealing temperature of 1200°C led to the formation of these planar twinning.

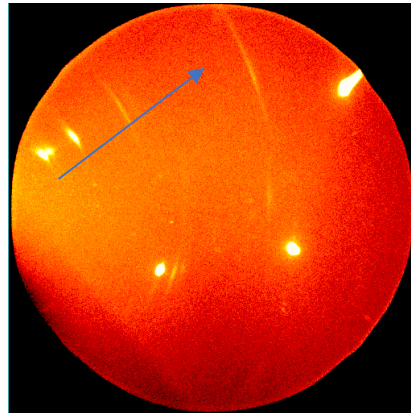


Figure 44. XRD frame of $60\text{-Eu}_{6.4}\text{Si}_{25.7}\text{O}_{67.9}\text{-N}_2\text{+H}_2\text{-}1200^\circ\text{C}$ at psi degree of 54, a full rotation of 360° phi. The blue arrow demonstrates normal to the surface.

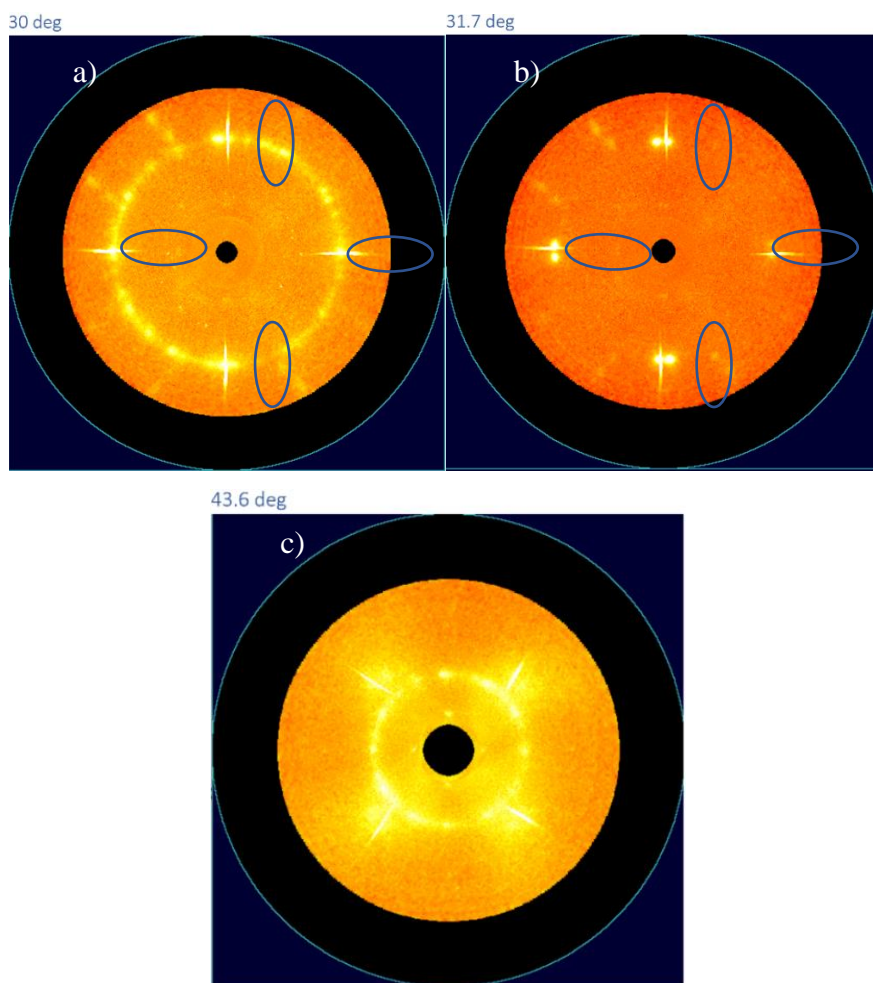


Figure 45. Pole figures of 60-Eu_{6.4}Si_{25.7}O_{67.9} annealed at 1200°C with N₂+H₂ atmosphere at 2θ of a) 30°; b) 31.7°; and c) 43.6°.

Similarly, in the pole figure generated at 30°, at 2θ degree of 43.6, there is a fiber with preferred orientation. In all the pole figures the intense bright spots at every 90° are related to the single crystal of Si substrate (shown with blue circles in Figure 45 (a) and (b)). The peak at 2θ of 44.8° which is not detected in the frame likely because of low scan time, similar to the ones at 30 and 43.6 2θ degrees, comes from the same crystalline phase ID, Eu₂(Si₂O₇) (PDF 01-076-0726). As previously discussed, the pole figures at 2θ of 30° and

43.6° both show patchy fiber structures. Since 44.8 2θ degree originates from the same crystalline phase, it may suggest that its structure is also patchy fiber.

Figure 46 shows the XRD patterns of all the IMS samples when annealed at 1350°C and N₂+H₂ atmosphere for 60 minutes. It is observed that identical polycrystalline phases are formed for all the samples annealed at 1350°C using N₂+H₂ ambient but with different intensities. This variation in the intensity is due to the different film compositions in each sample which consequently leads to different PL intensity (shown in Chapter 4. PL section). For quantifying the phases, Rietveld analysis is required, but because our samples are textured and except the Si₃N₄ phase, the rest of the phases are not a perfect match with Inorganic Crystal Structure Database (ICSD), performing the Rietveld measurements is not precise and beneficial.

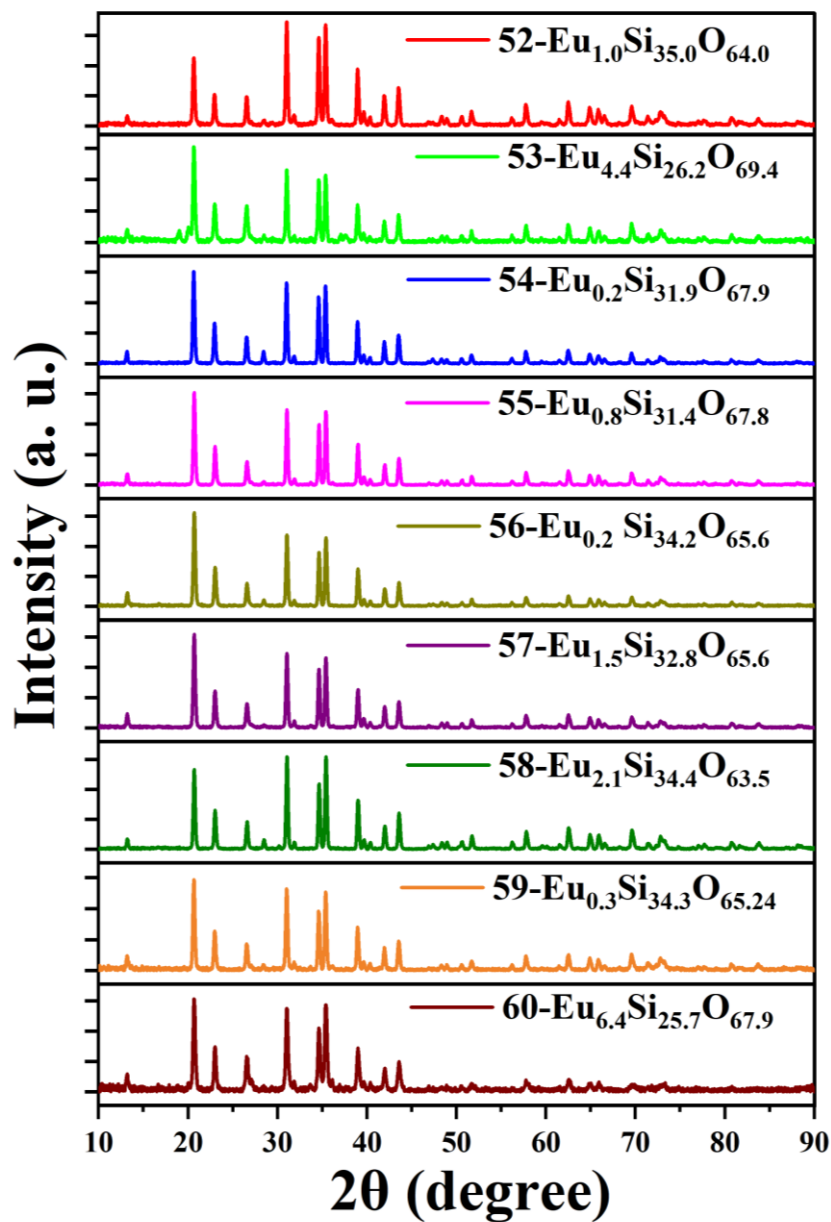


Figure 46. XRD pattern of all the IMS samples annealed at 1350°C and N_2+H_2 atmosphere.

Here the samples are discussed based on the ratio of the peak's intensity. Table 7 shows the film composition of samples 54-Eu_{0.2}Si_{31.9}O_{67.9}, 57-Eu_{1.5}Si_{32.8}O_{65.6} , and 60-

Eu_{6.4}Si_{25.7}O_{67.9} which are all fabricated using SiH₄ flow rate of 2 sccm and sputtering Ar flow rate of 40 sccm while the sputtering power is 10, 20, and 40 W, respectively. It can be observed that although when the samples are annealed at 1350°C and N₂+H₂ ambient, they form the same crystalline structure phases regardless of their composition, the intensity of the peaks varies (shown in Figure 47).

Looking at the elemental composition of the three samples, with increasing sputtering power, as expected the Eu concentration increases and the Si concentration decreases, while the O content virtually remains unchanged. The ratio of the peaks at 2θ of 26.5° to 28.4° which are corresponding to Eu_xSiO₂/ SiO₂ and Eu₂O₃, respectively, increases with increasing Eu concentration. Therefore, the increase of the Eu content likely decreases the Si content which implies that Eu³⁺ preferentially enters SiO₂ rather than forming crystalline structures containing O alone (e.g. Eu₂O₃).

Table 7. Elemental composition of 54-Eu_{0.2}Si_{31.9}O_{67.9}, 57-Eu_{1.5}Si_{32.8}O_{65.6}, and 60-Eu_{6.4}Si_{25.7}O_{67.9} which were fabricated using the Ar sputtering gas flow rate of 40 sccm and SiH₄ gas flow rate of 2 sccm with a variation of sputtering power ranging from 10 to 40 W; and the ratio of intensity at 2θ degrees corresponding to Eu_xSiO₂/ SiO₂ and Eu₂O₃ phases.

Samples	Eu at. %	Si at. %	O at. %	Intensity at 2θ=26.55°	Intensity at 2θ=28.42°	Intensity ratio of 26.55°/28.42°
54-Eu_{0.2}Si_{31.9}O_{67.9}	0.2	31.8	67.8	0.29	0.137	1.93
57-Eu_{1.5}Si_{32.8}O_{65.6}	1.3	30.5	68.1	0.20	0.022	9.26
60-Eu_{6.4}Si_{25.7}O_{67.9}	6.4	25.3	66.8	0.10	0.008	12.49

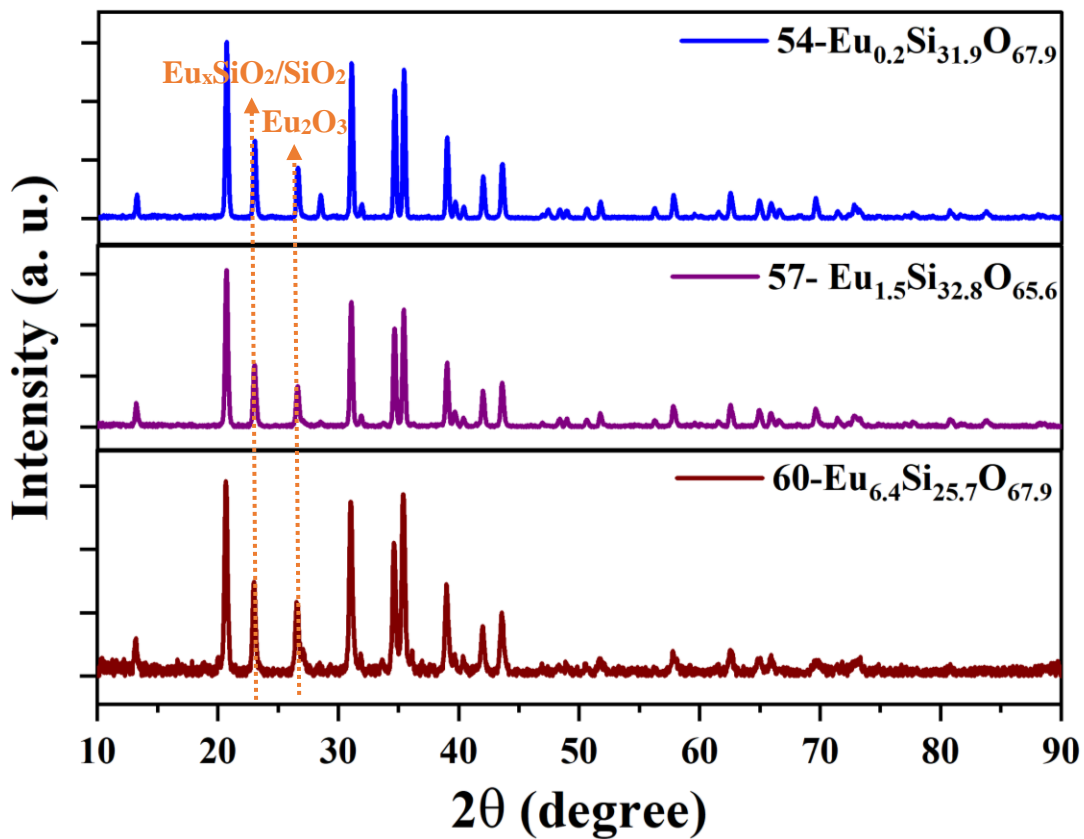


Figure 47. XRD pattern of 54- $\text{Eu}_{0.2}\text{Si}_{31.9}\text{O}_{67.9}$, 57- $\text{Eu}_{1.5}\text{Si}_{32.8}\text{O}_{65.6}$ and 60- $\text{Eu}_{6.4}\text{Si}_{25.7}\text{O}_{67.9}$ annealed using N_2+H_2 atmosphere at 1350°C .

5.2. Transmission Electron Microscopy

TEM was performed using the Talos 200X microscopes as an additional complimentary measurement to confirm the formation of crystalline structure. The samples were prepared using the FIB technique. Both FIB preparation and TEM measurements were conducted at McMaster University in Canadian Centre for Electron Microscopy (CCEM). The TEM images were taken from the cross-section view of 60-Eu_{6.4}Si_{25.7}O_{67.9} annealed at 1350°C and N₂+H₂ atmosphere. In the first attempt, the sample was damaged in the FIB preparation process and the thin film was mainly removed. This was confirmed by TEM measurements and as shown in Figure 48 only Si substrate was detected. The top layer where the thin film was removed is labelled with a red arrow.

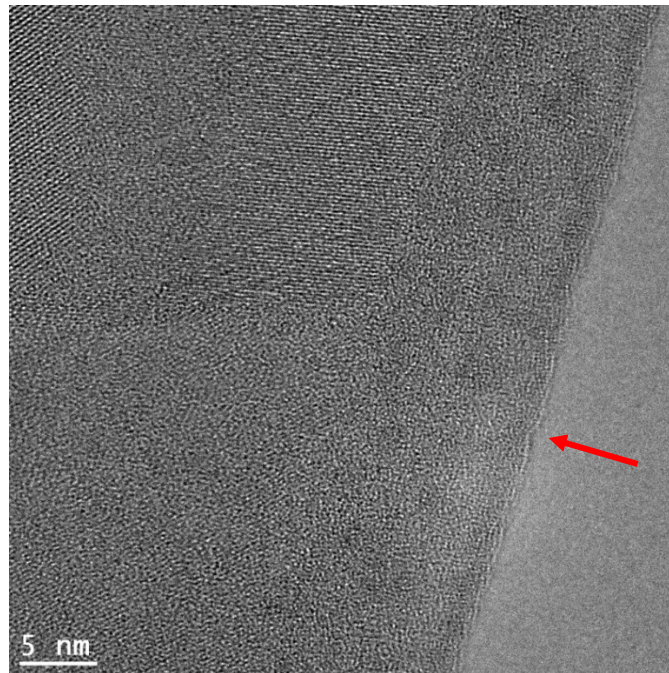


Figure 48. Bright field HR-TEM image of 60-Eu_{6.4}Si_{25.7}O_{67.9} damaged in FIB preparation.

In the second attempt, two lamellas were prepared with different thinning limits. The scanning electron microscopy (SEM) image of the area of interest is shown in Figure 49. The reason for preparing two lamellas with slightly different thicknesses is to provide the advantage of having another lamella in case the other one was damaged during the FIB preparation. Figure 50 shows the TEM image of both lamellas with a thickness of around 100 nm. The image is taken in the dark field mode where the heavier elements appear brighter since they scatter electrons more intensely. The lamella on the right-side window (Lamella 2) is thicker than the one on the left window (Lamella 1). Multilamellar preparation using the FIB technique also brings the benefit of delivering a variety of thicknesses for different applications.

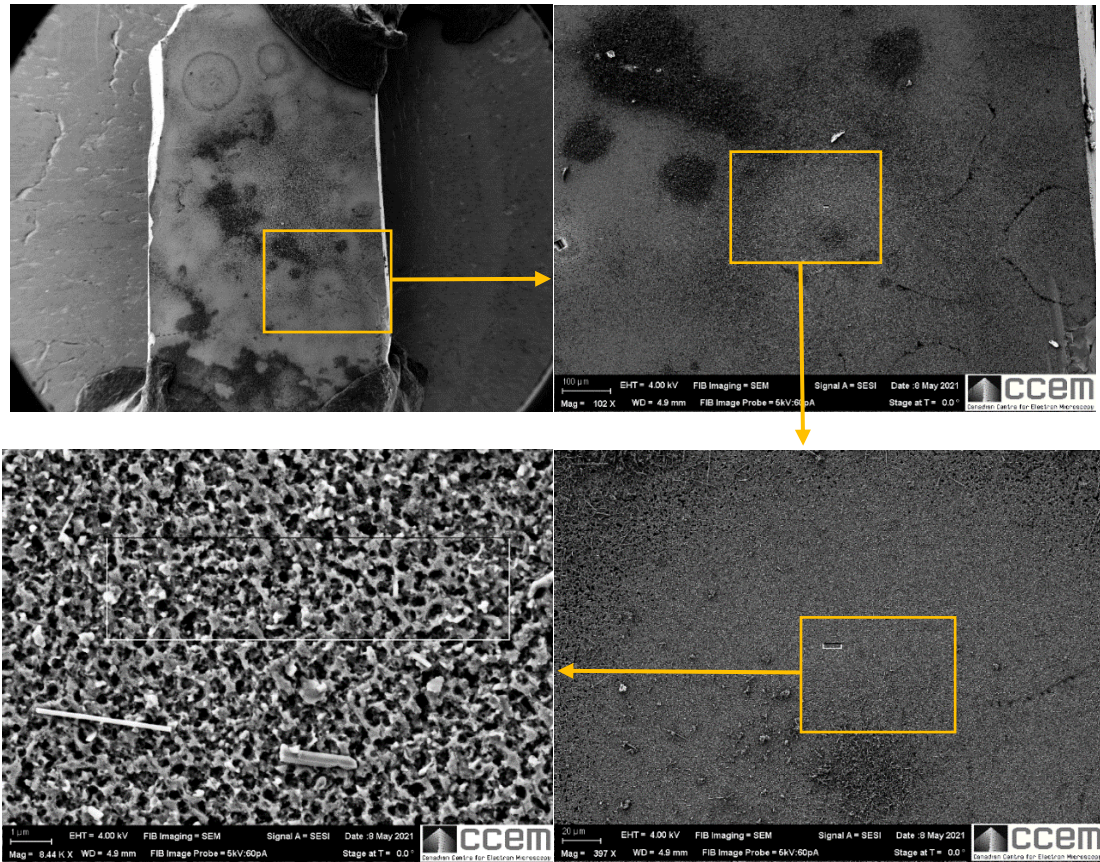


Figure 49. SEM images of the sample indicating the area where FIB preparation was performed.

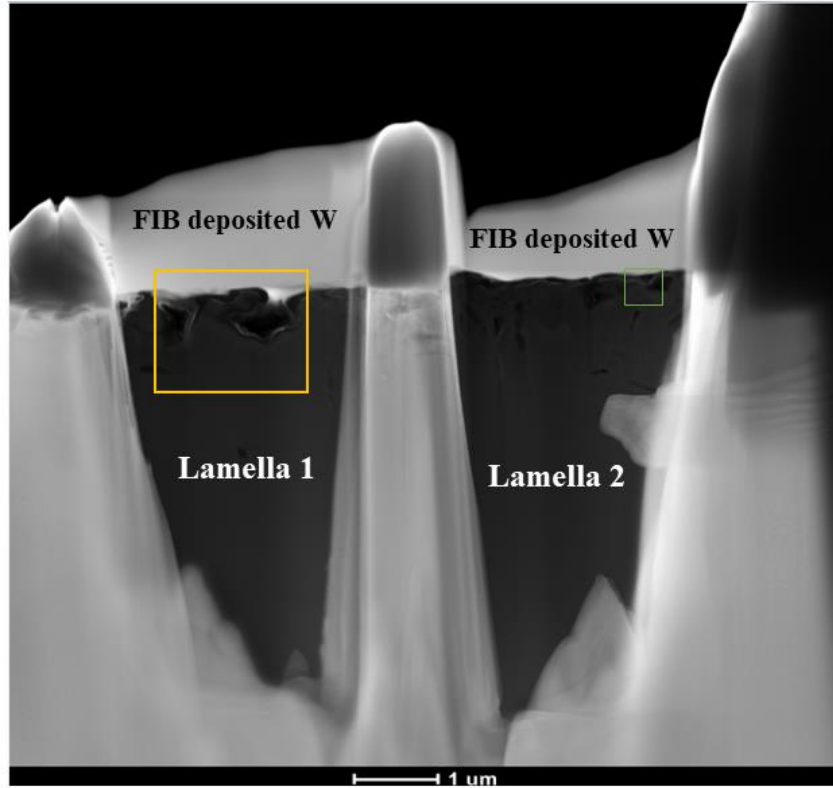


Figure 50. Cross-sectional dark-field TEM image of the two lamellas prepared using FIB technique on $60\text{-Eu}_{6.4}\text{Si}_{25.7}\text{O}_{67.9}$ annealed at 1350°C using N_2+H_2 atmosphere.

Figure 51 (a) shows the zoom up of the yellow selected area in Figure 50 and Figure 51 (b) shows the magnified image of the orange area in Figure 51 (a). Prior to the milling process the sample a layer of tungsten (W) is deposited on the sample to prevent damaging the thin film. The energy dispersive X-ray (EDX) image of Figure 51 (b) shows the distribution of each element in the thin film. Figure 52 verifies that the deposited W only diffused on the surface and did not spread deep into the thin film.

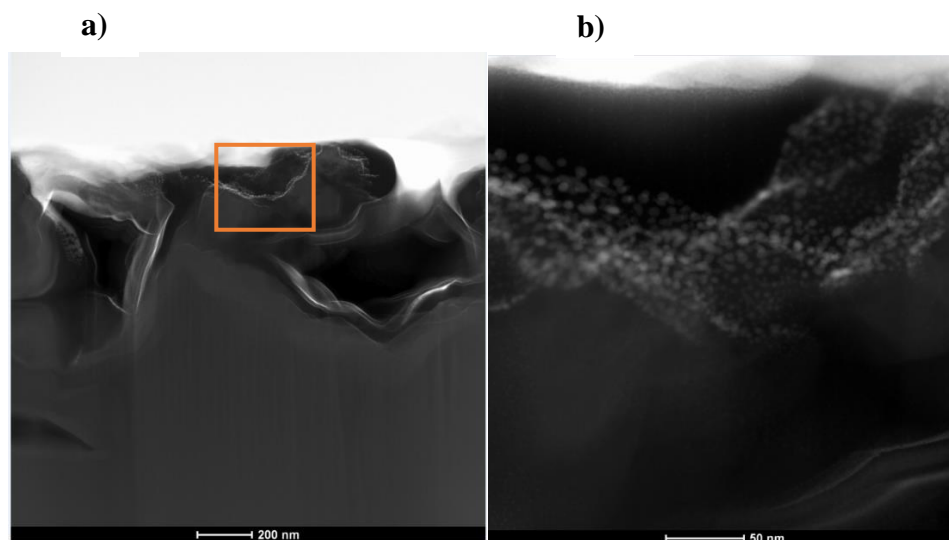


Figure 51. a) TEM imaging of the yellow marked area in Figure 50; b) Magnified view of the area marked in orange in Figure 51 (a).

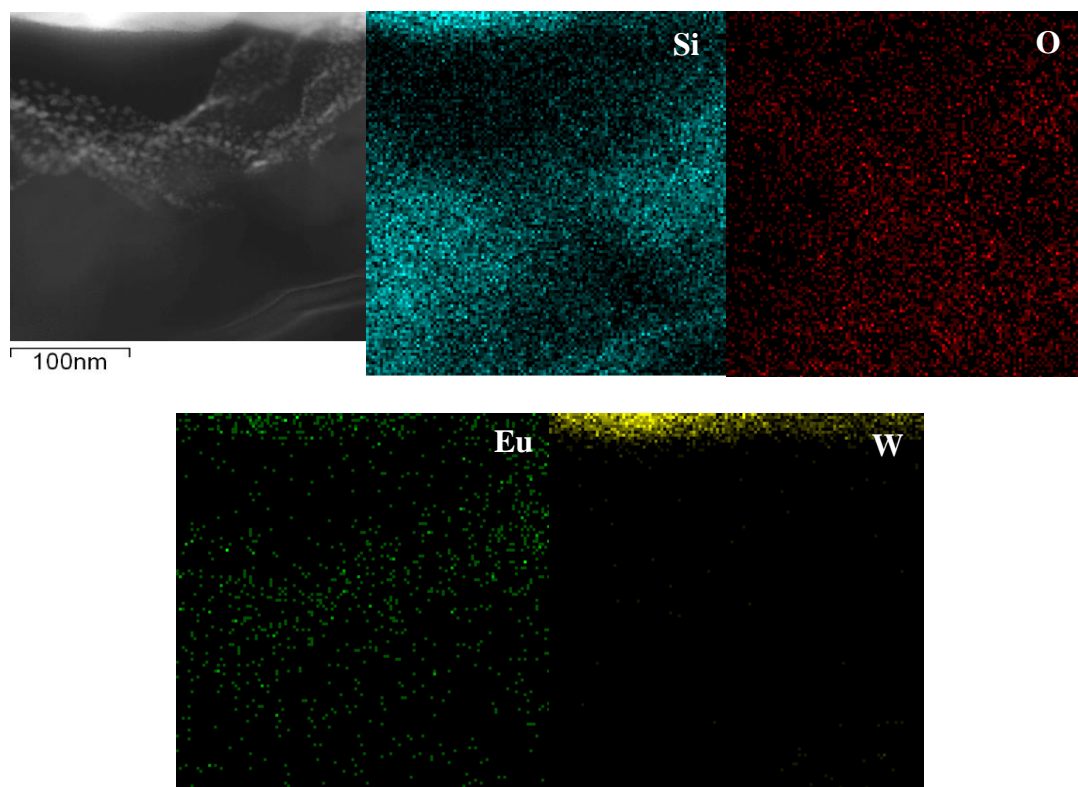


Figure 52. EDX of Figure 51 (b) shows the elemental mapping of the sample where the distribution of Si (blue), O (red), Eu (green), and W (yellow) are presented.

The formation of polycrystalline which was previously detected using XRD measurements is additionally observed in the HR-TEM image of $60\text{-Eu}_{6.4}\text{Si}_{25.7}\text{O}_{67.9}$ annealed at 1350°C

and N_2+H_2 atmosphere. The brightfield HR-TEM imaging of the sample shows the formation of $\text{Eu}_x\text{Si}_y\text{O}_z$ nanoclusters formed in the SiO_x host matrix. The heavier elements appear darker in the bright field where the lighter area is the SiO_x host. As shown in Figure 53 (b) the $\text{Eu}_x\text{Si}_y\text{O}_z$ nanoclusters (the darker areas) are surrounded by the SiO_x lattice fringes.

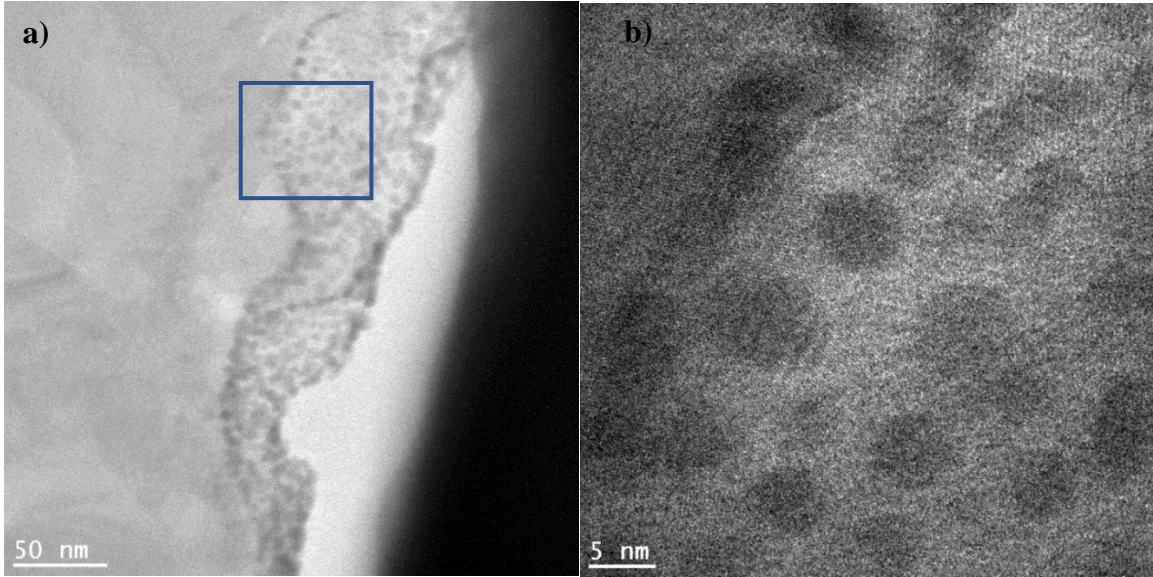


Figure 53. The bright field HR-TEM imaging of a) Zoom up of the marked green zone in Figure 50; b) Magnified view of the blue selected area in Figure 53 (a), where the formation of the $\text{Eu}_x\text{Si}_y\text{O}_z$ nanoclusters (darker spots) in the SiO_x matrix (the brighter spots) is observed.

Chapter 6: Conclusion and Future Work

In this chapter, a summary of the significant highlights remarking the optical and structural properties of the samples studied in this work is provided along with the potential future work which was not possible to be performed in the limited time of a master program.

In this thesis, a set of Eu-doped ORSO thin films with different deposition parameters were fabricated for the first time using IMS-ECR-PECVD system which is an ECR-PECVD machine upgraded with an additional sputtering gun. The samples were accordingly subjected to post-deposition annealing at temperatures ranging from 300 to 1350°C and two annealing ambientes of pure N₂ and N₂+H₂. . Using RBS measurements, it was observed that sputtering power has an intense and direct relation with the concentration of Eu while SiH₄ flow rate is inversely proportional to Eu concentration. VASE analysis confirmed that at a lower SiH₄ flow rate, a higher refractive index is achieved due to more incorporation of H. The thickness on the other hand increases with increasing the SiH₄ flow rate. PL measurements of the annealed samples showed that for the samples subjected to elevated temperatures of 1200 and 1350°C, higher PL intensity is achieved in the PAR range which is beneficial for photosynthesis applications whereas in the MOP samples there is no PL emission at the red light wavelengths. The effect of H passivation of the dangling bond on PL was studied by comparing the samples annealed at N₂ and the ones annealed using N₂+H₂ atmosphere. The PL intensity is boosted by one order of magnitude as the result of H passivation.

The structural properties of the samples were detected using XRD measurement while TEM measurement was performed as an additional complimentary analysis to XRD. It was

observed samples annealed at temperatures up to 900°C maintain the amorphous structure of SiO_x thin films, however, at higher temperatures polycrystalline structures are obtained which leads to more intense PL emission at wavelengths corresponding to Eu transitions. The TEM measurement approved the formation of polycrystalline structures and Si nanoclusters embedded in the host matrix.

Future Works

There are a few measurements that potentially can provide more comprehensive information about the composition (e.g. quantitative ERD measurements) and the structural properties (e.g. Rietveld analysis and synchrotron-based high energy XRD) of the thin films. In this thesis, only the Eu doped ORSO host matrix was studied while Si-rich SiO_x as the host matrix can be studied as well as SiN, and SiC to investigate the influence of N and C on the structure and light emission properties. Different matrices of SiO, SiN, SiC or a combination of these host materials, behave differently in the energy transferred to Eu ions based on the distance between the electron donor and acceptor levels. This brings the interest of studying these matrices and adjusting the luminescence selectivity.

One of the desired measurements is the quantitative ERD measurements to obtain the concentration of H. Due to the change of mylar foil in the RBS-ERD facility, the ERD simulation could not reach the desired fitting. The foil is installed on the detector to block the heavier element thus the lighter elements can be detected. In the SIMNRA package software, the composition of the foil has to be given to the software to proceed with the

simulation, however, since the facility was using a new foil, its composition was unknown and in the timeline of this master's program, the data could not be simulated quantitatively. In the XRD measurements, for the samples annealed at 1350°C using N_2+H_2 atmosphere, there was a Si_3N_4 crystalline phase detected, however, there was no N source during the deposition and in the RBS analysis no N was detected in the thin film composition. It was assumed that the unknown crystalline phase is some crystalline phase similar to Si_3N_4 such as Si_3O_4 . To confirm this assumption and indexing the unknown crystalline phase, the samples were measured in Brockhouse X-ray Diffraction and Scattering Beamlines - Low Energy Wiggler (BXDS-WLE) at Canadian light source (CLS). The analysis of the data takes several months and could not be achieved during the completion of this program. Measuring the weight percentage of the crystalline phases could provide valuable information to consider more details on the correlation of resulted PL intensity and the structure of the thin films. However, this also required more time for Rietveld analysis to be performed, analyzed, and discussed which can be done as a potential future work.

Bibliography

- [1] F. Priolo, T. Gregorkiewicz, M. Galli, and T. F. Krauss, “and photovoltaics,” *Nat. Publ. Gr.*, vol. 9, no. 1, pp. 19–32, 2014, doi: 10.1038/nnano.2013.271.
- [2] L. Brus, “Luminescence of silicon materials. Chains, sheets, nanocrystals, nanowires, microcrystals, and porous silicon,” *J. Phys. Chem.*, vol. 98, no. 14, pp. 3575–3581, 1994, doi: 10.1021/j100065a007.
- [3] D. Chen *et al.*, “Tuning into blue and red: Europium single-doped nano-glass-ceramics for potential application in photosynthesis,” *J. Mater. Chem. C*, vol. 3, no. 13, pp. 3141–3149, 2015, doi: 10.1039/c5tc00034c.
- [4] E. H. Murchie and K. K. Niyogi, “Manipulation of photoprotection to improve plant photosynthesis,” *Plant Physiol.*, vol. 155, no. 1, pp. 86–92, 2011, doi: 10.1104/pp.110.168831.
- [5] M. Ashraf and P. J. C. Harris, “Photosynthesis under stressful environments: An overview,” *Photosynthetica*, vol. 51, no. 2, pp. 163–190, 2013, doi: 10.1007/s11099-013-0021-6.
- [6] R. E. Blankenship *et al.*, “Comparing photosynthetic and photovoltaic efficiencies and recognizing the potential for improvement,” *Science (80-.)*, vol. 332, no. 6031, pp. 805–809, 2011, doi: 10.1126/science.1200165.
- [7] M. Tikkanen and E. M. Aro, “Integrative regulatory network of plant thylakoid energy transduction,” *Trends Plant Sci.*, vol. 19, no. 1, pp. 10–17, 2014, doi: 10.1016/j.tplants.2013.09.003.
- [8] M. Hammam, M. K. El-Mansy, S. M. El-Bashir, and M. G. El-Shaarawy,

- “Performance evaluation of thin-film solar concentrators for greenhouse applications,” *Desalination*, vol. 209, no. 1-3 SPEC. ISS., pp. 244–250, 2007, doi: 10.1016/j.desal.2007.04.034.
- [9] D. Chen, L. Lei, A. Yang, Z. Wang, and Y. Wang, “Ultra-broadband near-infrared excitable upconversion core/shell nanocrystals,” *Chem. Commun.*, vol. 48, no. 47, pp. 5898–5900, 2012, doi: 10.1039/c2cc32102e.
- [10] C. Ming, F. Song, X. Ren, and L. An, “Highly efficient reddish orange emission in Mn²⁺/Eu³⁺ co-doped phosphate glasses for greenhouse,” *Appl. Phys. Lett.*, vol. 103, no. 4, pp. 2012–2015, 2013, doi: 10.1063/1.4816597.
- [11] N. Katsoulas, A. Bari, and C. Papaioannou, “Plant responses to UV blocking greenhouse covering materials: A review,” *Agronomy*, vol. 10, no. 7, pp. 1–17, 2020, doi: 10.3390/agronomy10071021.
- [12] M. N. ain Nordin *et al.*, “Characterization on optical and mechanical properties of Low-Density Polyethylene films doped with Eu(III)complex,” *Adv. Mater. Res.*, vol. 895, pp. 162–168, 2014, doi: 10.4028/www.scientific.net/AMR.895.162.
- [13] E. Tsormpatsidis, R. G. C. Henbest, F. J. Davis, N. H. Battey, P. Hadley, and A. Wagstaffe, “UV irradiance as a major influence on growth, development and secondary products of commercial importance in Lollo Rosso lettuce ‘Revolution’ grown under polyethylene films,” *Environ. Exp. Bot.*, vol. 63, no. 1–3, pp. 232–239, 2008, doi: 10.1016/j.envexpbot.2007.12.002.
- [14] J. M. Fletcher, A. Tatsiopoulou, M. Mpezamihigo, J. G. Carew, R. G. C. Henbest, and P. Hadley, “Far-red light filtering by plastic film, greenhouse-cladding materials: Effects on growth and flowering in *Petunia* and *Impatiens*,” *J. Hortic.*

- Sci. Biotechnol.*, vol. 80, no. 3, pp. 303–306, 2005, doi: 10.1080/14620316.2005.11511934.
- [15] P. García-Macías *et al.*, “Changes in the flavonoid and phenolic acid contents and antioxidant activity of red leaf lettuce (Lollo Rosso) due to cultivation under plastic films varying in ultraviolet transparency,” *J. Agric. Food Chem.*, vol. 55, no. 25, pp. 10168–10172, 2007, doi: 10.1021/jf071570m.
- [16] X. Fu *et al.*, “Reprocessable, biodegradable polyester-based solid-solid phase change materials networks from dynamic ionic crosslinking with high latent heat capability,” *J. Clean. Prod.*, vol. 297, 2021, doi: 10.1016/j.jclepro.2021.126630.
- [17] D. Grifoni, G. Agati, F. Bussotti, M. Michelozzi, M. Pollastrini, and G. Zipoli, “Different responses of *Arbutus unedo* and *Vitis vinifera* leaves to UV filtration and subsequent exposure to solar radiation,” *Environ. Exp. Bot.*, vol. 128, pp. 1–10, 2016, doi: 10.1016/j.envexpbot.2016.03.012.
- [18] T. Tezuka, T. Hotta, and I. Watanabe, “Growth promotion of tomato and radish plants by solar UV radiation reaching the Earth’s surface,” *J. Photochem. Photobiol. B Biol.*, vol. 19, no. 1, pp. 61–66, 1993, doi: 10.1016/1011-1344(93)80094-P.
- [19] C. Maraveas, “Environmental sustainability of greenhouse covering materials,” *Sustain.*, vol. 11, no. 21, 2019, doi: 10.3390/su11216129.
- [20] W. D. Callister, “Materials science and engineering: An introduction (2nd edition),” *Mater. Des.*, vol. 12, no. 1, p. 59, 1991, doi: 10.1016/0261-3069(91)90101-9.
- [21] J. N. Hahladakis, C. A. Velis, R. Weber, E. Iacovidou, and P. Purnell, “An

- overview of chemical additives present in plastics: Migration, release, fate and environmental impact during their use, disposal and recycling,” *J. Hazard. Mater.*, vol. 344, pp. 179–199, 2018, doi: 10.1016/j.jhazmat.2017.10.014.
- [22] X. Hao and A. P. Papadopoulos, “Effects of supplemental lighting and cover materials on growth, photosynthesis, biomass partitioning, early yield and quality of greenhouse cucumber,” *Sci. Hortic. (Amsterdam)*, vol. 80, no. 1–2, pp. 1–18, 1999, doi: 10.1016/S0304-4238(98)00217-9.
- [23] S. Ghani *et al.*, “Design challenges of agricultural greenhouses in hot and arid environments – A review,” *Eng. Agric. Environ. Food*, vol. 12, no. 1, pp. 48–70, 2019, doi: 10.1016/j.eaef.2018.09.004.
- [24] P. P. Reddy, “Sustainable crop protection under protected cultivation,” *Sustain. Crop Prot. under Prot. Cultiv.*, pp. 1–434, 2016, doi: 10.1007/978-981-287-952-3.
- [25] A. Kumar *et al.*, “Bio-inspired and biomaterials-based hybrid photocatalysts for environmental detoxification: A review,” *Chem. Eng. J.*, vol. 382, no. September 2019, p. 122937, 2020, doi: 10.1016/j.cej.2019.122937.
- [26] A. J. G. Zarbin, “Liquid–liquid interfaces: a unique and advantageous environment to prepare and process thin films of complex materials,” *Mater. Horizons*, 2021, doi: 10.1039/d0mh01676d.
- [27] G. C. Sih, M. N. Abdelaziz, and T. Vu-Khanh, *Particle and Continuum Aspects of Mesomechanics*. 2010.
- [28] R. P. Dabkowski, “Installation of a New Electron Cyclotron Plasma Enhanced Chemical Vapour Deposition (ECR- PECVD) Reactor and a Preliminary Study of Thin Film Depositions,” MSc thesis, McMaster University, 2012.

- [29] R. D. Arnell and P. J. Kelly, “Recent advances in magnetron sputtering,” *Surf. Coatings Technol.*, vol. 112, no. 1–3, pp. 170–176, 1999, doi: 10.1016/S0257-8972(98)00749-X.
- [30] J. W. Miller, Z. Khatami, J. Wojcik, J. D. B. Bradley, and P. Mascher, “Integrated ECR-PECVD and magnetron sputtering system for rare-earth-doped Si-based materials,” *Surf. Coatings Technol.*, vol. 336, pp. 99–105, 2018, doi: 10.1016/j.surfcoat.2017.08.051.
- [31] A. Podhorodecki, G. Zatoryb, L. W. Golacki, J. Misiewicz, J. Wojcik, and P. Mascher, “On the origin of emission and thermal quenching of SRSO:Er³⁺ films grown by ECR-PECVD,” *Nanoscale Res. Lett.*, vol. 8, no. 1, pp. 1–12, 2013, doi: 10.1186/1556-276X-8-98.
- [32] T. R. Roschuk, “A study of luminescent Si-based materials through X-ray spectroscopies,” PhD thesis, McMaster University, 2009.
- [33] F. Priolo, T. Gregorkiewicz, M. Galli, and T. F. Krauss, “Silicon nanostructures for photonics and photovoltaics,” *Nat. Nanotechnol.*, vol. 9, no. 1, pp. 19–32, 2014, doi: 10.1038/nnano.2013.271.
- [34] A. J. Kenyon, *Recent developments in rare-earth doped materials for optoelectronics*, vol. 26, no. 4–5. 2002.
- [35] G. Franzò, V. Vinciguerra, and F. Priolo, “Excitation mechanism of rare-earth ions in silicon nanocrystals,” *Appl. Phys. A Mater. Sci. Process.*, vol. 69, no. 1, pp. 3–12, 1999, doi: 10.1007/s003390050967.
- [36] D. E. BLAKIE, “COUPLED LUMINESCENCE CENTRES IN ERBIUM-DOPED SILICON RICH SILICON OXIDE THIN FILMS DEPOSITED BY ECR-

- PECVD,” MSc Thesis, McMaster University, 2006.
- [37] Y. Gao, “Optical and Electrical Properties of Ce Doped Silicon Based Thin Films
Optical and Electrical Properties of Ce Doped Silicon Based Thin Films,”
McMaster University.
- [38] P. Mascher, “XANES and XEOL Investigation of Cerium and Terbium Co-Doped
Silicon Oxide Films,” vol. 45, no. 5, pp. 43–48, 2012.
- [39] A. Baran, S. Mahlik, M. Grinberg, and E. Zych, “High pressure and time-resolved
luminescence spectra of Ca $3\text{Y}_2(\text{SiO}_4)_3$ doped with Eu^{2+} and Eu^{3+} ,” *J. Phys.
Condens. Matter*, vol. 25, no. 2, 2013, doi: 10.1088/0953-8984/25/2/025603.
- [40] E. J. Nassar *et al.*, *Europium III: Different emission spectra in different matrices,
the same element*, no. January. Franca – SP – Braz: Nova Science Publishers, Inc.,
2010.
- [41] J. Li, “Light emission from rare earth-doped silicon oxide thin films deposited by
ECR-PECVD,” MSc Thesis, McMaster University, 2008.
- [42] A. Mariscal-Jiménez *et al.*, “Photoluminescence and Stoichiometry Correlation in
Nanocrystalline EuO_x Thin Films: Tunable Color Emission,” *J. Phys. Chem. C*,
vol. 124, no. 28, pp. 15434–15439, 2020, doi: 10.1021/acs.jpcc.0c03052.
- [43] Z. Khatami, “Luminescent Silicon Carbonitride Thin Films Grown Using Ecr
Pecvd : Fabrication and Characterization Luminescent Silicon Carbonitride Thin
Films Grown Using Ecr Pecvd : Fabrication and,” PhD Thesis, McMaster
University, 2017.
- [44] Z. Khatami, L. Wolz, J. Wojcik, and P. Mascher, “Highly Controlled Deposition of
Rare Earth Doped Si-based Thin Films : Integrated Magnetron Sputtering and

- Plasma Enhanced Chemical Vapor Deposition,” *J. Mater. Res.*, 2021.
- [45] T. Müller, K. H. Heinig, and W. Möller, “Size and location control of Si nanocrystals at ion beam synthesis in thin SiO₂ films,” *Appl. Phys. Lett.*, vol. 81, no. 16, pp. 3049–3051, 2002, doi: 10.1063/1.1512952.
- [46] J. Perrière, “Rutherford backscattering spectrometry,” *Vacuum*, vol. 37, no. 5–6, pp. 429–432, 1987, doi: 10.1016/0042-207X(87)90327-7.
- [47] F. Corni, G. Ottavinaï, M. Michelini, G. L. Michelutti, L. Santi, and A. Stefanel, “Rutherford Backscattering Spectrometry: a technique worth introducing into pedagogy,” in *Teaching the science of condensed matter and new materials. GIREP 1995 book of selected papers.*, 1996, pp. 266–272.
- [48] F. J. Ager *et al.*, “Rutherford backscattering spectrometry (RBS) characterization of oxide scale formed on (AISI-304) steel after surface deposition of lanthanum,” *Acta Mater.*, vol. 44, no. 2, pp. 675–681, 1996, doi: 10.1016/1359-6454(95)00193-X.
- [49] Z. Khatami, P. R. J. Wilson, J. Wojcik, and P. Mascher, “The influence of carbon on the structure and photoluminescence of amorphous silicon carbonitride thin films,” *Thin Solid Films*, vol. 622, pp. 1–10, 2017, doi: 10.1016/j.tsf.2016.12.014.
- [50] M. Mayer and M. Mayer, “SIMNRA User ’ s Guide,” *Book*, 1997.
- [51] G. Dollinger, M. Boulouednine, A. Bergmaier, T. Faestermann, and C. M. Frey, “Limits in elastic recoil detection analysis with heavy ions,” *Nucl. Instruments Methods Phys. Res.*, no. 95, 1996.
- [52] J. A. Woollam *et al.*, “Basic Theory and Typical Applications,” vol. 10294, pp. 3–28, 2017, doi: 10.1117/12.351660.

- [53] J. A. Woollam, “CompleteEASETM Data Analysis Manual,” 2011.
- [54] J. Miller, “A novel approach to thin film deposition and rare-earth incorporation for silicon integrated photonics,” PhD Thesis, McMaster University, 2020.
- [55] B. B. He, *Two-dimensional X-ray Diffraction Book*, Second edi. John Wiley & Sons, Inc, 2018.
- [56] J. Li, O. H. Y. Zalloum, T. Roschuk, C. L. Heng, J. Wojcik, and P. Mascher, “Light emission from rare-earth doped silicon nanostructures,” *Adv. Opt. Technol.*, vol. 2008, 2008, doi: 10.1155/2008/295601.
- [57] S. Jing, H. Jiang, Y. Hu, and C. Li, “Graphene supported mesoporous single crystal silicon on Cu foam as a stable lithium-ion battery anode,” *J. Mater. Chem. A*, vol. 2, no. 39, pp. 16360–16364, 2014, doi: 10.1039/c4ta03370a.
- [58] B. B. He, *Two-dimensional X-ray Diffraction*. 2018.
- [59] T. O. Yeates, “Detecting and overcoming crystal twinning,” *Methods Enzymol.*, vol. 276, no. 1974, pp. 344–358, 1997, doi: 10.1016/S0076-6879(97)76068-3.

Curriculum Vitae

Rashin Basiri Namin

Islamic Azad University 2009-2013 Bachelor of Chemical Engineering

University of New Brunswick 2019-2021 Master of Science in Chemical Engineering

Publications:

Hailong Yu, Jingjing Hou, Rashin Basiri Namin, Yonghao Ni, Shiwei Liu, Shitao Yu, Yuxiang Liu, Qiong Wu, Shuangxi Nie, Pre-cryocrushing of natural carbon precursors to prepare nitrogen, sulfur co-doped porous microcellular carbon as an efficient ORR catalyst, Carbon, Volume 173, 2021, Pages 800-808, ISSN 0008-6223, <https://doi.org/10.1016/j.carbon.2020.11.069>

Rashin Basiri Namin et al 2020 Meet. Abstr. MA2020-02 2749, Europium Doped Silicon Oxide Thin Films Using an Integrated PECVD and Sputtering System.

Conference Presentations:

The Electrochemical Society ECS Meeting 238th 2020, Europium Doped Silicon Oxide Thin Films Fabricated Using an Integrated PECVD and Sputtering System

Photonics North 2021, Comparison of Two Rare Earth Doping Techniques for Luminescent Europium Doped Silicon Oxide